A STUDY OF INCLUSIVE PRODUCTION OF OPEN CHARM PARTICLES AT HERA-B ENERGIES USING $\phi(1020)$ AS A TAG

A Dissertation
Presented to the Faculty of the Department of Physics
University of Houston

In Partial Fulfillment
of the Requirements for the Degree
Doctor of Philosophy

By
Halasya Siva Subramania
May 2005

A STUDY OF INCLUSIVE PRODUCTION OF OPEN CHARM PARTICLES AT HERA-B ENERGIES USING $\phi(1020)$ AS A TAG

Halasya Siva Subramania

APPROVED:

Dr. Kwong Lau, Chairman

Dr. Bill W. Mayes

Dr. David Bao

Dr. Ed Hungerford

Dr. Lawrence Pinsky

Dean, College of Natural Sciences and Mathematics

ACKNOWLEDGEMENTS

It is almost five years since I joined graduate school. The physics analysis in this dissertation has been an interesting experience in exploring various aspects of data analyses and signal hunting from a huge sample with significant background. Many people have helped me along to complete this dissertation successfully.

First of all, I heartfully thank God for everything I have and get to enjoy. Then I thank my parents for their care, support, and everything. They have been of great support. Next, I have to thank Mr. Balkishanji Mohta (1940-2000) who was instrumental in helping me to join Physics.

I do not have words to express my gratitude towards my advisor Dr. Kwong Lau, starting from selecting me and giving me a chance to join the High Energy Physics community. I am extremely grateful to him. He is nothing less than a godfather to me. I want to thank him for dealing with me patiently and teaching about everything from survival in science to life. I am surely going to miss those friendly discussions about science, politics, business, international affairs and many others. I want to thank him for being there for me, for helping me join the HERA-B experiment, for giving me an opportunity to work on the preliminary phase of the BTeV experiment and also a chance to work at Fermilab for an entire summer.

As a colleague, a best friend and almost a second guide, I want to thank Dr. Mikayel Ispiryan, who also has patiently listened, discussed, and taught me so many things for this dissertation to come out successful. Thanks for his encouragement and motivation to make me keep trying with a never-die attitude.

Further, I want to thank my dissertation committee members for their support and critical comments during the yearly meetings to make this a better dissertation. I want to thank all my teachers and staff in the Department of Physics at the University of Houston for bearing with me for five years. I also want to convey a special thanks to Ms. Naomi Haynes for all her help and kindness through these five years at UH.

Well, I should not forget about all the friends that I have made during my PhD here at UH. Especially, I would like to thank my friend Chamith Rajapakse for helping me on several occasions like, for instance, by sharing his LATEX tools specific to UH thesis requirements and also sharing his knowledge and expertise in computer and programming. I also would like to thank Logan Lebanowski for helping me with the language corrections in my dissertation. I also want to thank all my friends from back home, Nandu, Ravi, Sinoj, to name a few, who have been of great support and encouragement during hard times and I know they will be there to share all the fun in my life forever.

I want to thank the HERA-B Collaboration and my DESY colleagues especially, Dr. Michael Medinnis and Dr. Joachim Spengler for their kind help in making me feel at home during my visit to DESY. I also want to thank Dr. Michael Symalla, Dr. Chris Van Eldik, Dr. Yuriy Pylypchenko, Dr. Törsten Zeuner and many others for sharing their knowledge with me about the HERA-B experiment. All of them had helped me with many unscheduled discussions and sharing their knowledge about the HERA-B experiment. I also want to thank this great person Frau. Sielaff, who gave me a place to stay in Germany whom I call my German grandma. She took care of me so well that I want to thank God for giving me a chance to meet such a kind person.

Finally, I want to say that so many people have helped me along the way. I do not intend to forget anyone. Please do not mistake me if I did.

THANK YOU ALL.

A STUDY OF INCLUSIVE PRODUCTION OF OPEN CHARM PARTICLES AT HERA-B ENERGIES USING $\phi(1020)$ AS A TAG

An Abstract of a Dissertation
Presented to the Faculty of the Department of Physics
University of Houston

In Partial Fulfillment
of the Requirements for the Degree
Doctor of Philosophy

By
Halasya Siva Subramania
May 2005

ABSTRACT

A study of inclusive charm production using the channel $c\bar{c} \rightarrow D_i(\bar{D}_j) + X \rightarrow \phi + X' \rightarrow K^+K^-$ has been done. Interaction triggered data from the HERA-B experiment with ϕ's produced from pA interactions at $\sqrt{s} = 41.6$ GeV are used for analysis. A detailed analysis of ϕ production at HERA-B energies has been done. The ϕ production cross-section has been measured to be $\sigma_{0\phi} = (1.08^{+0.14}_{-0.12}) \cdot A^{\alpha_\phi}$ mb, where α_ϕ is measured to be $\alpha_\phi = 0.92 \pm 0.03$. The displacement of the decay vertex of the ϕ's produced from charm decay compared to those produced directly in the primary interaction is used to obtain the fraction of ϕ's from charm decay which in turn is used to determine the inclusive charm cross-section, namely, the sum of all charm cross-section, each weighted by its branching ratio to ϕ. The inclusive cross-section for open charm production has been measured in terms of the ϕ cross-section to be $\sum_i BR(D \rightarrow \phi)\sigma_{0D_i} = (11.12 \pm 5.90 \pm 4.80) \cdot A^{1.02}$ μb.

DEDICATION

To My Parents,

Bal Kishenji Mohta & Family

&

My Sweet Little Nephews

TABLE OF CONTENTS

ABSTRACT . . . . . **vi**

LIST OF FIGURES . . . . . **xi**

LIST OF TABLES . . . . . **xiii**

CHAPTER 1 INTRODUCTION AND PHYSICS MOTIVATION . **1**

1.1 History 3

1.2 The Standard Model 4

1.2.1 Quantum Chromodynamics 7

1.3 Cross-sections 8

1.3.1 Inclusive cross-sections in hadron collisions 10

1.4 Open-Charm Production 11

1.4.1 Properties of the Open-Charm particles and ϕ mesons 11

1.4.2 Open-charm production 12

1.4.3 ϕ production 14

CHAPTER 2 THE HERA-B EXPERIMENT **17**

2.1 Overview 17

2.2 The HERA Storage Ring 18

2.3 The HERA-B Spectrometer 20

2.3.1 The Target System 22

2.3.2 Silicon Vertex Detector 24

2.3.3 The Magnet 26

2.3.4 The Inner Tracker 27

2.3.5 The Outer Tracker 29

2.3.6 The Ring Imaging Čerenkov Detector 32

2.3.7 Electromagnetic Calorimeter 35

2.3.8 The Muon Detector 38

2.4 HERA-B Data Acquisition 40
2.4.1 Front End Electronics 41
2.5 The HERA-B Trigger System 42
2.5.1 Pretriggers 43
2.5.2 The First Level Trigger 44
2.5.3 The Second Level Trigger 44
2.5.4 The Third Level Trigger 46
2.5.5 The Fourth Level Trigger 46
CHAPTER 3 DATA RECONSTRUCTION 48
3.1 Data Storage 48
3.2 Event Reconstruction 50
3.2.1 Analysis and Reconstruction Tool for Events 50
3.2.2 Event Reconstruction Packages 51
3.2.3 File generation sequence in event reconstruction 54
3.3 HERA-B Event Simulation 55
3.3.1 Model for open-charmed mesons generation 56
3.3.2 Model used for generation of ϕ mesons 57
3.4 Experimental determination of cross-section 58
3.4.1 Luminosity determination 59
3.5 Error Analysis Methods 62
3.5.1 Statistical Errors 62
3.5.2 Systematic Errors 64
CHAPTER 4 DATA ANALYSIS AND RESULTS 65
4.1 The Δz Method 66
4.1.1 What is Δz? 66
4.1.2 Method description 68
4.1.3 Method to measure the *open-charm* cross-section 70
4.1.4 $A-$Dependence correction 70

4.2 ϕ Analysis 72
4.2.1 Data sample 72
4.2.2 Selection criteria 72
4.2.3 ϕ Counting and Mass measurement 79
4.2.4 ϕ Cross-Section 81
4.2.5 $A-$dependence of ϕ production 85
4.3 Open Charm Analysis 86
4.3.1 Selection Criteria 86
4.3.2 Determination of the fraction of ϕ mesons from charm decay by the Δz method 90
4.3.3 Charm Cross-section 94
CHAPTER 5 SUMMARY 96
APPENDIX A Method to reconstruct a vertex from two given tracks 100
REFERENCES 102

LIST OF FIGURES

1.1 A schematic representation of a hadron-hadron interaction depicting the role of cross-section . . . 9

1.2 Feynman diagrams for $c\bar{c}$ production . . . 13

1.3 Feynman diagram for $c\bar{c}$ fragmentation into D mesons . . . 14

1.4 The Feynman diagrams for ϕ production . . . 15

2.1 Schematic of the HERA storage ring . . . 19

2.2 Diagram of a bunch structure . . . 19

2.3 Schematic of the HERA-B spectrometer . . . 21

2.4 Schematic view of the target system . . . 22

2.5 Schematic view of SVD . . . 25

2.6 Schematic view of an ITR . . . 27

2.7 Schematic view of a single layer of ITR . . . 28

2.8 Schematic View of OTR . . . 30

2.9 Schematic View of the RICH detector . . . 31

2.10 Čerenkov angle distribution . . . 34

2.11 Čerenkov angle versus momentum distribution . . . 36

2.12 Example showing the effect of particle identification by the RICH in K_S^0 detection . . . 37

2.13 Schematic View of ECAL . . . 38

2.14 Schematic View of the MUON . . . 39

2.15 Schematic View of the muon chamber module . . . 39

2.16 Flow chart representing the output rates for the four trigger levels . . . 43

2.17 Schematic representation of the FLT concept . . . 45

3.1 A simple box diagram showing basic hierarchy of the data storage . . . 49

3.2 A diagram showing the ring reconstruction method . . . 53

4.1 A typical interaction diagram showing the various Δz contributions . . . 67
4.2 Venn diagram representation of fractional ϕ distribution 68
4.3 Distribution of number of interactions per event 73
4.4 Hit distributions of (a) SVD (b) OTR 74
4.5 Hit distributions of the RICH detector 75
4.6 Particle likelihood efficiency plots 76
4.7 Effect of kaon likelihood on ϕ selection 77
4.8 Opening angle distribution of K^+K^- vs ϕ 79
4.9 Invariant mass spectrum of K^+K^- 80
4.10 A Plot showing disagreement between data and Monte Carlo events . . . 83
4.11 The γ correction factor as a function of p_T^2 83
4.12 The x_F distribution after the p_T^2 correction 84
4.13 The rapidity "y" distribution after the p_T^2 correction 84
4.14 Plot to measure α and σ_0 85
4.15 Δz resolution plot for ϕ's from data, primary interactions, and charm decays 88
4.16 Δz resolution plot for K^+K^- and ϕ 89
4.17 The Δz as a function of $m_{K^+K^-}$ with primary vertices from ARTE tables 91
4.18 The Δz as a function of $m_{K^+K^-}$ with primary vertices reconstructed by the averaging method 91
4.19 The $z-$coordinate distribution of the primary vertices obtained from ARTE table, those obtained by "the averaging of all vertices of track pairs in an event" method and the target position 92
5.1 The ϕ cross-section measured at HERA-B is compared to other experiments and there seems to be excellent agreement with both theory and experiment 97

LIST OF TABLES

1.1 The different forces of nature and their relative strengths with reference to the strong forces 5

1.2 Quarks of the Standard Model 6

1.3 Leptons of the Standard Model 6

1.4 Gauge Bosons of the Standard Model 6

1.5 Properties of D mesons 11

1.6 Decay modes of ϕ mesons and branching ratios 12

2.1 Target material and dimensions 23

2.2 Table for Channel and Data per channel 40

3.1 Inelastic cross-sections for different target materials for 920 GeV/c pN interactions 60

3.2 Hodoscopes rate correction factor for different target materials 61

4.1 Table for step-by-step reconstruction efficiency measurement $w.r.t$ events 78

4.2 Table for step-by-step reconstruction efficiency measurement $w.r.t$ tracks 78

4.3 Table for ϕ counting 81

4.4 Table for ϕ production cross-sections 82

4.5 Table for Δz displacement of ϕ's 93

4.6 Table of fraction of ϕ's 94

4.7 Table of efficiencies for ϕ and charm detection 94

4.8 Table for charm cross-section 95

5.1 Properties of D mesons 98

CHAPTER 1

INTRODUCTION AND PHYSICS MOTIVATION

The aim of this dissertation is to study the production of ϕ mesons and open charm hadrons in 920 GeV/c pA collisions, using the data from the HERA-B experiment. HERA-B was a fixed target experiment, performed using high energy protons from the "Hadron Elektron Ring Anlage" (HERA) storage ring colliding with wire targets at the "Deutsches Elektronen-Synchrotron" (DESY) Lab in Hamburg, Germany. The experiment was designed to study CP violation in B mesons. HERA-B experiment was an international collaboration of some 250 physicists from 13 countries. This dissertation focuses on physics analysis of ϕ mesons using the data from HERA-B.

The open charm hadrons, produced from proton-nucleus interactions, are detected through the $\phi(1020)$ meson decay channel. The ϕ meson, in turn, is detected through the $\phi \to K^+K^-$ decay channel. In a typical interaction, ϕ mesons may be produced either from primary interactions, or as decay products of a heavier particle. An example of a heavy particle is an open charm hadron. The pseudoscalar mesons D^0, D^+, D_s^+, and their anti-particles are open charm hadrons. These charm particles do not decay into a ϕ meson alone in general. The four-momentum must be conserved, which means the decay will produce two or more products. In this study, we require to have a ϕ meson present in the final state of the D decay. This means that all decay channels of the D mesons which have a ϕ in the final state are included, irrespective of the accompanying particles. Therefore, the $c\bar{c} \to D_i + \bar{D}_j \to \phi + X$ production cross-section is called an *inclusive* measurement.

ϕ mesons are extremely short lived particles. Open charm hadrons have lifetimes which are several orders of magnitude larger. Open charm particles live long enough to have a measurable flight distance (well above the detector's resolution

along the forward z direction) before their decay in the HERA-B detector. We call the decays of the open charm hadrons "charm decays." The long lifetime is used as a signature to separate the ϕ mesons produced through charm decays from the ϕ mesons produced in primary interactions. A new technique, called the Δz method, is used to extract statistically the fraction of ϕ mesons which are produced from charm decays with respect to the total number of ϕ mesons produced. The quantity Δz is a measure of the average flight distance travelled by the particles before their decay in the forward z direction with reference to the z coordinate of the primary interaction vertex. Using this information, the inclusive production cross-section of open charm hadrons with each species weighted by its respective branching ratio to ϕ, $\sum_i \mathcal{BR}(D_i \to \phi X)\sigma_{D_i}$, is measured in terms of the ϕ production cross-section. This relative measurement is expected to have minimum systematic error. To summarize, the following three quantities are measured:

- σ_ϕ - ϕ production cross-section.
- $f_{c\phi}$ - Fraction of ϕ mesons from charm decay.
- $\sum_i \mathcal{BR}(D_i \to \phi X)\sigma_{D_i}$ - Inclusive charm cross-section.

In this chapter, a brief introduction to particle physics is given. In section 1.1, a brief history about quarks is presented. Particle physics has evolved to a coherent model called the "Standard Model" which characterizes forces and particles at the most elementary level. A brief description of the Standard Model is presented in section 1.2, together with an introduction to Quantum Chromodynamics (QCD). Heavy quark production in hadron collisions is still an open subject. Various models have been proposed. Each model fits certain experimental results. None of them can completely explain all the experimental results. The results of inclusive charm production can be used to test heavy quark production models. Production of particles are quantified by cross-sections. In section 1.3, a brief description of cross-sections is presented. Finally, production processes and models describing heavy quark production, heavy quark fragmentation, and ϕ production are discussed.

1.1 History

The first elementary particle called the "corpuscle" and later renamed as the "electron", was discovered towards the end of nineteenth century. This discovery marked the beginning of a field of physics which seems to have a never ending history of ideas put forward by some of the most brilliant minds the world has ever seen. Ever since, elementary particle physics has been a subject which is constantly searching for new particles and theories to explain the origin of the particles and the origin and evolution of our universe. After the electrons, the nuclei, protons, neutrons, pions, positrons, neutrinos and muons were some of the other path breaking discoveries. It was discovered that an atom is made of a core of positively charged massive nucleus and a distribution of electrons surrounding the nucleus. The nucleus is made of protons and neutrons. Nonetheless, elementary particle physics was at its infancy until the discovery of quarks. In the meantime, numerous particle detectors were invented, most of which are used in present-day experiments.

In 1964 Gell-Mann [1] and Zweig [2] introduced the idea of quark structure of hadrons. Since then, many new particles have been discovered. The quark model classifies the hadrons into baryons and mesons. Baryons are made of three quarks. Mesons are made of quark-antiquark pairs. Quarks carry fractional charges of $\frac{2}{3}|e|$ or $-\frac{1}{3}|e|$, where $|e| = 1.6 \times 10^{-19}\ C$ is the electron charge. The quark type or 'flavor' is denoted by a symbol: u for 'up', d for 'down', s for 'strange', c for 'charm', b for 'bottom', and t for 'top'. The names for the u and d quarks were derived from their isospin orientations: u for up-spin and d for down-spin. The names of b and t quarks were derived in a similar manner. The 's for strange' terminology came about because these quarks were found to be constituents of the so-called 'strange particles' first discovered in cosmic rays. Strange particles are found to be produced prolifically in strong interactions. Since they are produced strongly, they are expected to decay strongly too, in the strong interaction time scale (10^{-23} s). But strangely, the strange particles decay weakly in the time scale of $\approx 10^{-10}$ s, hence their 'strange' name. The solution to the puzzle came in the form of a new quantum number 'strangeness'. Strangeness is conserved in strong interactions. The

'c for charm' quark was discovered after the observation of heavy meson states of the type $J/\psi = c\bar{c}$. The charm quark's introduction also explained the experimental observation of the suppression of strangeness-changing neutral current decays [3]. After the discovery of charm, the observation of the upsilon (Υ) gave rise to the introduction of the bottom quark 'b'. To complete the group, the introduction of the Cabibbo-Kobayashi-Masakawa (CKM) matrix formulation led to the prediction of the top quark 't'. After a long wait, the top quark was finally observed at the Tevatron in 1995. It was found that the top quark has a mass which is orders of magnitude higher ($\approx 175\ GeV/c^2$) than those of the other quarks. Its high mass explains its extremely short lifetime.

1.2 The Standard Model

In his science fiction novel, *The Rolling Stones*, Robert A. Heinlein comments:

> Every technology goes through three stages: first a crudely simple and quite unsatisfactory gadget; second, an enormously complicated group of gadgets designed to overcome the shortcomings of the original and achieving thereby somewhat satisfactory performance through extremely complex compromise; third, a final proper design therefrom.

After about six decades of extensive research and numerous discoveries, particle physics has matured to its final stage in developing an explanatory model. The "Standard Model" [4] is a theoretical framework built on observations which predict and correlate new data. The Mendeleev table of elements was an early example of such a framework in chemistry; from the periodic table one can predict the properties of many hitherto unstudied elements and compounds. Nonrelativistic quantum theory is another paradigm which has correlated the results of countless experiments. The Standard Model of particle physics has been enormously successful in predicting a wide range of phenomena. And, just as ordinary quantum mechanics fails in

the relativistic limit, we do not expect the Standard Model to be valid at arbitrarily short distances. Nevertheless, the Standard Model has remained an excellent approximation to nature at distance scales as small as 10^{-18} m.

The Standard Model describes nature in terms of four distinct forces. The forces are characterized by widely different ranges and strengths as measured at an energy scale of 1 GeV. Table 1.1 describes the four forces and their relative strengths. The main achievement of the Standard Model was its unified description of the electromagnetic and weak interactions. Also included is the accurate description of strong interactions by the theory of QCD. Gravity is much too weak to play any significant role in ordinary particle processes, so it has not yet been included in the Standard Model. But, attempts are still being made to include gravitation in the Standard Model. The strong and weak interactions have a very short range ($\approx 10^{-15}$ m), about

Table 1.1 *The different forces of nature as per the Standard Model and their relative strengths with reference to the strong forces.*

Force type	**Relative strength**
strong	1
electromagnetic	10^{-2}
weak	10^{-7}
gravity	10^{-39}

the size of the nucleus. The range of an interaction indicates the distance of its influence beyond which it falls off rapidly to zero. Relatively speaking, electromagnetic interactions and gravitation have infinite range.

The Standard Model is based on the SU(3)×SU(2)×U(1) symmetry group corresponding to the theories of QCD, weak interactions and electromagnetism, respectively. The Standard Model is characterized by its classification of matter fields consisting of fermions and bosons. These matter fields are classified as *quarks*, *leptons*, and *gauge bosons*. The leptons and the gauge bosons carry integral charges. Quarks, on the other hand, carry fractional charges as confirmed by experiment. Quarks and leptons are fermions with half integral spin. Gauge bosons have integral

spin. It is interesting to note that there are six "flavors" of quarks and leptons. The six particles, in both cases, are divided into three generations with two flavors in each generation. Each interaction has its own mediating gauge bosons: the strong interactions are mediated by the gluons, the photons mediate the electromagnetic interactions, the W's and the Z mediate the weak interactions and, presumably, the gravitons mediate gravitional interactions. Tables 1.2, 1.3, and 1.4 show the spectra of elementary fields with some of their physical properties. Q represents the electric charge and m represents the mass. The subscripts 1, 2 and 3 in the quark columns of Table 1.2 stand for the color quantum numbers. All quantum numbers are conserved

Table 1.2 *Quarks of the Standard Model.*

Q=$\frac{2}{3}\|e\|$	m, **GeV**/c^2	**Q**=$-\frac{1}{3}\|e\|$	m, **GeV**/c^2
u_1, u_2, u_3	(2-8) $\times 10^{-3}$	d_1, d_2, d_3	(5-15) $\times 10^{-3}$
c_1, c_2, c_3	(1-1.6)	s_1, s_2, s_3	(0.1-0.3)
t_1, t_2, t_3	173.8 ± 5.0	b_1, b_2, b_3	$(4.1 - 4.5)$

Table 1.3 *Leptons of the Standard Model.*

Q= $-\|e\|$	m, **GeV**/c^2	**Q**= 0	m, **GeV**/c^2
e	5.11×10^{-4}	ν_e	$< 1.5 \times 10^{-8}$
μ	10.566×10^{-2}	ν_μ	$< 1.7 \times 10^{-4}$
τ	1.7770	ν_τ	$< 1.8 \times 10^{-2}$

Table 1.4 *Gauge Bosons of the Standard Model.*

Quantum	m, **GeV**/c^2
$g_1 ... g_8$	<a few $\times 10^{-3}$
γ	$< 6 \times 10^{-25}$
$W^{\pm}$, Z^0	80.39 ± 0.06, 91.187 ± 0.002

in strong interactions while some quantum numbers, such as strangeness, need not be conserved in weak interactions.

1.2.1 Quantum Chromodynamics

Quantum Chromodynamics (QCD) is the formal theory of the strong color interactions. According to Fermi-Dirac statistics, the existence of the Ω^- particle which is composed of three strange quarks, or the Δ^{++} which is composed of three up-quarks, both of which have a total spin of $\frac{3}{2}$, has to be precluded. This is because three identical fermions with their spins aligned cannot exist in a symmetric s-wave ground state. This led to the idea that quarks carry an additional quantum number called *color*, a conjecture supported by experimental observations. A combination of further experimental observations and theoretical analyses probes the nucleon structure by verifying various aspects of the constituents inside the nucleon, called partons. The word 'chromo' means 'color' in Greek. The color charge of a quark has three possible values. Antiquarks carry anticolors. Leptons do not carry color, and hence they do not participate in strong interactions. Quark-quark interactions conserve color. The gluons mediating quark-quark interactions carry a unit of color and another unit of anti-color, a combination which belongs to a $SU(3)$ octet. The color charge of the strong interactions is analogous to the electric charge of electromagnetic interactions. But, unlike the weak interaction's two types of charged and uncharged mediating bosons, QCD has eight colored mediating bosons. The QCD Lagrangian density is very similar to its QED counterpart, and has the form:

$$L_{QCD} = -\frac{1}{4}F^a_{\mu\nu}F^{\mu\nu}_a + i\sum q\bar{\psi}^i_q\gamma^\mu(D_\mu)_{ij}\psi^j_q - \sum_q m_q\bar{\psi}^i_q\psi^i_q \tag{1.1}$$

where,

$$F_{\mu\nu} = \partial_\mu A^a_\nu - \partial_\nu A^a_\mu + g_s f_{abc}A^b_\mu A^c_\nu$$
$$(D_\mu)_{ij} = \delta_{ij}\partial_\mu - ig_s\sum_a \lambda^a_{ij}A^a_\mu/2$$

where g_s represents the strength of the strong interaction, f_{abc} stands for the structure constants of the SU(3) symmetry group. The subscripts $a,\ b,\ c$ take values from 1 to 8. λ^a_{ij} are the generators of the SU(3) group and ψ^i_q are the 4-component Dirac spinors describing quarks of color i and flavor q. A^a_μ are the eight gauge bosonic fields. The evidence that gluons mediate the QCD color-force was first observed in experiments at the e^+e^- collider 'PETRA' at DESY in Hamburg, Germany.

The strong interaction coupling constant is two orders of magnitude larger than the electromagnetic interaction coupling constant. One of the great triumphs of QCD is the discovery of the strong interaction coupling constant's dependence on the separation distance between the interacting particles [5]. This dependence makes the strong interaction constant a *running coupling constant*. At relatively large distances which are characteristic of nuclear physics, the coupling constant is large. This explains quark confinement, *i.e.*, there are no observable free quarks. At short distances, the coupling constant is small, a behavior which is opposite to what was observed in QED. This behavior in QCD is known as *asymptotic freedom*.

Even though the Standard Model is in agreement with many experimental observations, many questions remain unanswered. There are still speculations whether elementary particles known today are made of more elementary subparticles. To answer these questions, we need new physics beyond the Standard Model. It is now believed that the Standard Model explains most of the observations in hadron physics including this experiment.

1.3 Cross-sections

Interactions can be studied in many different ways. Three experimental probes of elementary particle interactions include bound states, decays and scattering. The internal structure of the interacting particles may be studied using scattering. Cross-sections quantify scattering. A schematic of a hadron-hadron interaction is shown in Figure 1.1, depicting the dependence of the interaction cross-section on various parameters such as the parton distribution functions, properties of the final state, and parton-parton interaction cross-sections. In Figure 1.1, P_a and P_b stand for the four-momenta of the two interacting hadrons, $F_{a(q)}$ and $F_{b(q)}$ represent the parton distribution functions of the particles a and b, and q stands for a parton inside the hadrons. σ stands for the hadron-hadron cross-section, and c represents the final state of the parton-parton interaction.

Electrons scatter off a target more readily than neutrinos and less so than

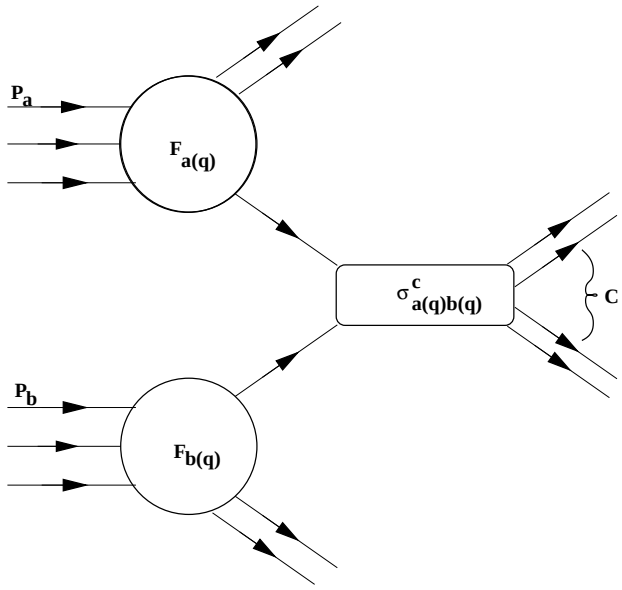

Figure 1.1 *A schematic representation of a hadron-hadron interaction depicting the role of cross-section.*

protons because different types of interactions are involved. If the energy is high enough, in addition to *elastic* scattering, *inelastic* processes will take place. The inelastic processes are further divided into diffractive processes and non diffractive processes. The elastic and diffractive processes give rise to low multiplicity events with particles emitted in the very forward and backward regions in the center of mass system. Each interaction process with a specific final state has an "exclusive" scattering cross-section, σ_i (for process i). In some cases, however, the final products are not examined, and we are interested only in the *total* cross-section.

$$\sigma_{tot} = \sum_{i=1}^{n} \sigma_i \tag{1.2}$$

The cross-section typically depends on the momentum of the incident particle. Loosely speaking, cross-sections are expected to be proportional to the time the incident particle spends in the vicinity of the target. This implies that cross-section is inversely proportional to the momentum. A "resonance" is a special case where the particles interact and form a short-lived semibound state [5] before breaking apart. Short lived particles, according to Heisenberg Principle, appear as resonances with

measurable widths. Most high energy hadron-hadron interactions are strong inelastic interactions. Since strong interactions have a finite range, which is of the order of the nuclear radius ($\approx 1\ fm$), the cross-sections are very close to the geometrical cross-section of the nucleus. Therefore, cross-sections are measured in units of *barn*. $1\ barn = 10^{-24}$ cm^2.

1.3.1 Inclusive cross-sections in hadron collisions

In a high energy hadron collision, the final state is complex because many particles are produced from the collision. Particles in the final state can be produced either in the primary interaction or as decay products. An inclusive cross-section measures the production of a certain particle in the final state, irrespective of how it is produced. Inclusive hadronic cross-sections exhibit the property of scaling and factorization [6]. At very high center of mass energies, the inclusive cross-section depends on the transverse momentum ($p_\perp = \sqrt{p_x^2 + p_y^2}$) and the longitudinal momentum fraction x_F ($= 2p_z/\sqrt{s}$, where p_z is in the center-of-mass frame). All experimental hadronic cross-sections show a strong exponential decrease with respect to transverse momentum ($p_\perp$). And, since a large number of slow particles are produced, the differential cross-section falls rapidly as $x_F \to 1$. The combined dependence is given by the relation:

$$\frac{d^2\sigma}{dx_{\mathrm{F}}\, dp_\perp} \propto (1 - x_F)^n \cdot e^{-bp_\perp^2}. \tag{1.3}$$

The parameters b and n depends on the process.

In this dissertation, the cross-section of open-charm production from hadron collisions is studied using the ϕ meson as a tag. The ϕ cross-section is measured using a "direct method" which is described in chapter 3. ϕ is a bound state of a strange and an anti-strange ($s\bar{s}$) quark pair. In a fixed target experiment, the production rate of hadrons made of quarks heavier than s is orders of magnitude smaller than the rate of hadrons made of lighter quarks. At HERA-B, the $D^\pm$ and $D^0(\bar{D}^0)$ production cross-sections have been measured using their prominent hadronic decay modes [7, 8, 9]. The total number of reconstructed D's is $\approx$ 150 each. The $D_s^\pm$ is known to be produced with an even lower cross-section [3]. This makes it extremely difficult to

reconstruct the $D_s^{\pm}$ mesons directly using the prominent hadronic $\phi\pi$ decay mode on an event-by-event basis. However, one can measure statistically the D_s cross-section using the fact that the ϕ's coming from $D_s \to \phi + X$ ($\approx 20\%$ of the time) decay have large flight distances. The Δz method, described in Chapter 4, is used to separate the ϕ mesons statistically. Since we cannot distinguish between the charm parent of the ϕ in this case, we measure the inclusive open-charm cross-section with each species weighted by its branching ratio to ϕ.

1.4 Open-Charm Production

1.4.1 Properties of the Open-Charm particles and ϕ mesons

The main decay modes of the charm mesons (D) are hadronic and semileptonic. For this dissertation, we look only at the decays that contain a $\phi(1020)$ meson in the final state. The branching ratios ($\mathcal{BR}s$) for these decay modes are listed in the last column of Table 1.5.

Table 1.5 *Properties of* D *mesons.*

Particle	**Quark content**	**Mass, MeV/c^2**	**Lifetime, *ps***	$\mathcal{BR}(D_i \to \phi)$**, %**
$D^0(D^0)$	$c\bar{u}(\bar{c}u)$	1864.5 ± 0.5	0.412 ± 0.003	1.7 ± 0.8
$D^+(D^-)$	$c\bar{d}(\bar{c}d)$	1869.3 ± 0.5	1.051 ± 0.013	< 1.8
$D_s^+(D_s^-)$	$c\bar{s}(\bar{c}s)$	1968.5 ± 0.6	0.490 ± 0.009	18^{+15}_{-10}

The ϕ meson is an ideally mixed $s\bar{s}$ bound state of the ground-state vector meson nonet. The mass of the ϕ meson is 1019.456 ± 0.020 MeV/c^2 [10]. As a short lived particle, it is observed as a resonance with a full width half maximum (FWHM) equal to 4.26 ± 0.05 MeV/c^2. In general, the ϕ is referred to as $\phi(1020)$, but it is used either way in this dissertation. The main decay modes of the ϕ mesons and their corresponding branching ratios are given in Table 1.6. There are many more radiative and semileptonic decay modes with very small branching ratios. They are not relevant to the present analysis.

Table 1.6 *Dominant decay modes of ϕ mesons and branching ratios.*

Decay mode	$\mathcal{BR}, \%$
$\phi \to K^+K^-$	$49.2^{+0.6}_{-0.7}$
$\phi \to K^0_L K^0_S$	33.7 ± 0.5
$\phi \to \rho\pi + \pi^+\pi^-\pi^0$	15.5 ± 0.5

1.4.2 Open-charm production

Open charm production takes place in two steps. According to theory, there is no charm quantum number for the interacting particles before collision. Charm quarks are generated during interactions. In strong interactions, all quantum numbers must be conserved. Therefore, they are produced as a charm-anticharm quark pair. This pair needs not be a bound state like the J/ψ, η_c or the χ. The $c\bar{c}$ pair, if not bound, is unstable and cannot exist freely because of quark confinement. Therefore, they combine with other lighter quarks to form relatively stable open charm particles.

Heavy Quark production

The production of charm-anticharm pairs ($c\bar{c}$) is categorized as heavy quark production. The processes involved are expected to be similar for bottom and top quarks as well. Heavy quark production in hadronic collisions has been a topic of interest for many years. The dependence of the strong interaction coupling constant on the mass of the interacting quarks, leads to the explanation of production of new particles only in the realm of perturbation theory. Heavy quark production processes happen to be a very good test for the theory of perturbative Quantum Chromodynamics (pQCD) where the production of heavy quark flavors are calculable until their masses are sufficiently large [11]. The current ideas in pQCD agree very well with measurements concerning the top quark. While their agreement for bottom and charm quarks is not as good, but is valid within the quoted errors. Various models have been proposed to layout the theoretical framework of heavy quark production from hadronic collisions. Recent studies based on pQCD have been predicting heavy

quark production to next-to-leading-order (NLO) and next-to-next-to-leading order (NNLO) and have proven very promising [12]. Heavy quark production in hadronic collisions, especially those containing charm quarks, have proven to be a useful test of the QCD parton-fusion model [13].

According to the parton model and pQCD, there are two types of leading order processes ($\mathcal{O}(\alpha_s)$) responsible for heavy quark production: one is quark-antiquark annihilation and the other is gluon-gluon fusion [12]. The various leading order pro-

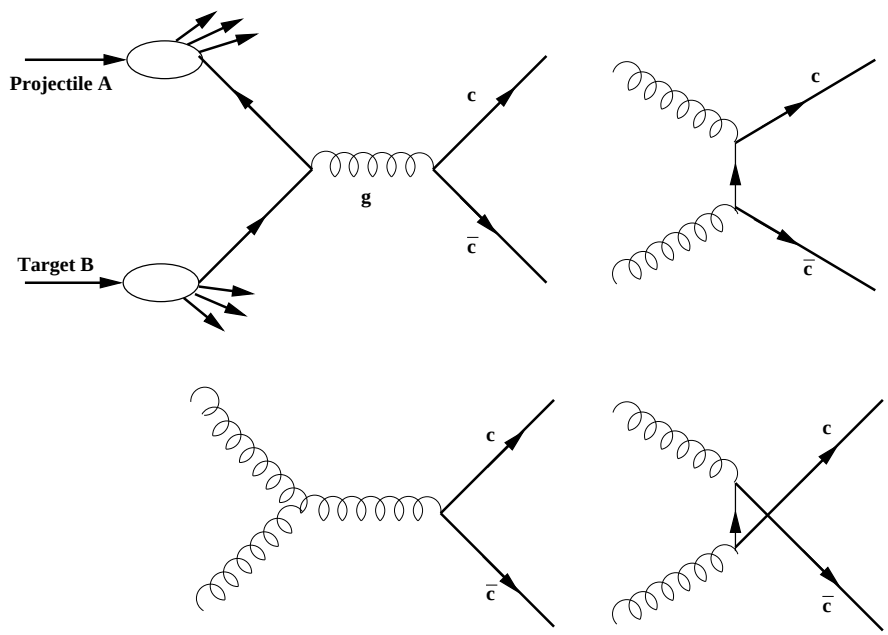

Figure 1.2 *Feynman diagrams for $c\bar{c}$ production.*

cesses for $c\bar{c}$ production are shown in Figure 1.2. In fixed target experiments, very few quark-antiquark interactions are possible, except with antiquarks from the sea. Virtual quark-antiquark pairs continually created out of the vacuum, make a sea of quarks, antiquarks, and gluons. Therefore, heavy quark production is mostly due to the gluon fusion process. In the next-to-leading-order (NLO) processes ($\mathcal{O}(\alpha_s^2)$), the quark-gluon interaction is the main contribution.

Heavy Quark fragmentation

The process of unstable $c\bar{c}$ pairs hadronizing into D mesons is called fragmentation. A well known model called the string fragmentation model [14] is commonly used to describe fragmentation. The origin of the confinement of quarks into hadrons is in the strong potential that increases with the separation between the quarks. According to the string fragmentation model, the interaction field of the heavy quark pair is channeled into a tube. This tube, which is a bond between the quark-antiquark pair, stretches due to the separation of the quark-antiquark pair. The energy density along this tube is constant. When the stretching is sufficient, the unstable heavy quark pair fragments and binds with other lighter quarks to form new bound states in order to lower the potential energy. This stretching continues until the momenta of the quarks become too low to create new tubes and the quarks become glued to other lighter quarks and form hadrons. The process of formation of new particles through fragmentation is called hadronization [15, 16]. The fragmentation of a $c\bar{c}$ pair and their hadronization into open charm hadrons is shown in Figure 1.3. The $c(\bar{c})$ can

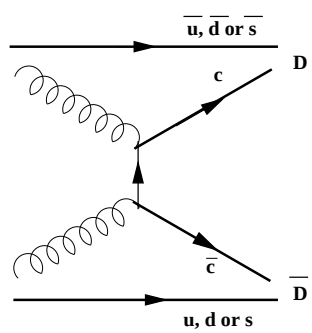

Figure 1.3 *Feynman diagram for $c\bar{c}$ fragmentation into D mesons.*

combine with $\bar{u}, \bar{d}, \bar{s}(u, d, s)$ to form open charm hadrons such as the D mesons.

1.4.3 ϕ production

The production of ϕ mesons has been an important subject of study. The ϕ meson is the lightest bound state of strange quarks. The production of the ϕ meson is

suppressed in ordinary hadronic interactions, like pN interactions, because of the Okubo-Zweig-Iizuka (OZI) rule [17]. In the naïve quark model, nucleons have no $s\bar{s}$ content. So, as in the case of charm production, strange quarks are expected to be produced only during interactions. The OZI rule implies the suppression of ϕ production from nucleons which have no valence strange quarks. In heavy ion collisions, ϕ mesons are considered to be a useful tool to probe various phenomena, such as the quark-gluon plasma state formation. There is a speculation that the nucleon has an intrinsic strangeness component, which can be probed using ϕ mesons from heavy ion collisions.

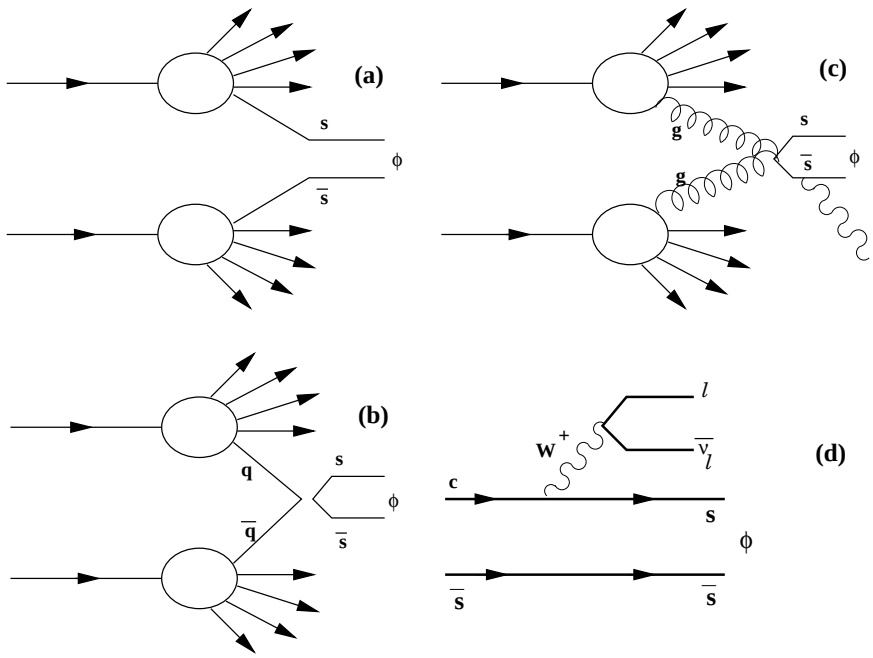

Figure 1.4 *The Feynman diagrams for ϕ production.*

In hadron-hadron interactions, the parton fusion model that was used to describe heavy quark production in the case of $c\bar{c}$, also effectively describes the production of $s\bar{s}$ bound states and ϕ mesons [18]. In an experiment with proton-nucleon interactions, the ϕ mesons are produced mainly through the gluon fusion process as in the case of heavy quark production. Figures 1.4*a, b* and *c* show the various Feynman diagrams describing direct ϕ production. Figure 1.4*d* shows the Feynman diagram of

ϕ production through the decay of a D_s meson. Similar processes as the one in Figure 1.4d describe ϕ production through D^0 and $D^{\pm}$ decays. The production cross-section predicted from the parton fusion model is found to agree with experiment.

To summarize the physics motivation of this dissertation, production cross-section measurements help in furthering the knowledge of production mechanisms at a higher center of mass energy and verify the validity of QCD. The results can be used as input to determine parton distribution functions, a topic outside the scope of this dissertation. The ϕ production cross-section will be measured using a direct method. The charm production cross-section will be measured using the Δz (z displacement from the primary vertex to the decay vertex) method described in Chapter 4 using the ϕ sample.

CHAPTER 2

THE HERA-B EXPERIMENT

2.1 Overview

The HERA-B experiment was a fixed target experiment, where the 920 GeV/c proton beam of the "Hadron Elektron Ring Anlage" (HERA) storage ring at "Deutsches Elektronen-Synchrotron" (DESY) collides with fixed target wires with a center of mass energy ($\sqrt{s}$) of 41.6 GeV. The detector was mainly designed to study CP violation in B decays. The $b\bar{b}$ production cross section is expected to be ≈ 25 nb per nucleon and hence, practically speaking, the interaction rate must be high [19] to get an ample amount of B's produced. The amount of data recorded must also be high to capture enough B events.

The main challenges of the HERA-B spectrometer as one can imagine were to cope with the high interaction rate. This required the spectrometer to possess the following qualities:

- a good solid angle coverage
- a good tracking system
- a good particle identification device
- a very efficient DAQ and trigger system.

As shall be seen in this chapter, HERA-B had all the qualities above. The main goal of HERA-B to study CP violation in B decays could not be achieved because of technical reasons and uncertain theoretical estimates for the b cross-section. In spite

of such a difficulty, the large amount of data recorded during the operation of the experiment gave scope to do various other useful physics studies.

2.2 The HERA Storage Ring

The HERA storage ring is located at the DESY research laboratory in Hamburg, Germany. The storage ring, shown in Figure 2.1, has a series of pre-accelerators in "Positron Elektron Tandem Ring Anlage" (PETRA) where the protons and electrons/positrons get accelerated to 40 GeV/c before filling two separate storage rings. The storage rings are located in the 6.3 km long HERA tunnel. The storage rings accelerate the protons to 920 GeV/c and the electrons to 27.5 GeV/c. At the time this data was taken, there were four experiments that were using the beams - H1, ZEUS, HERMES and HERA-B. The experiments H1 and ZEUS allow the electron and proton beams to collide and study the parton structure functions using deep inelastic ep scattering. The HERMES experiment uses a longitudinally polarized electron beam to interact with a polarized gas target to study spin structure of the nucleons. HERA-B used the proton beam *halo* which contain protons drifting away from the beam center. The HERA-B interaction point and the detector were located at "Hall West" as shown in Figure 2.1.

The HERA proton beam is organized into bunches. Each bunch contains approximately 10^{11} protons. There are potentially 220 buckets or bunches, out of which only 180 of them are filled. This discrepancy is attributed to the filling procedure. Each bunch takes 21.2 μs to travel around the HERA tunnel. In HERA-B, each crossing was identified by a bunch crossing number with each bunch separated in time by about 96 ns. This amounts to a bunch crossing rate of 10 MHz. A typical bunch structure is shown in Figure 2.2. The filled bunches were separated into three trains, and each train was a collection of six groups. A group contains ten bunches, and the groups are separated by a single empty bunch.

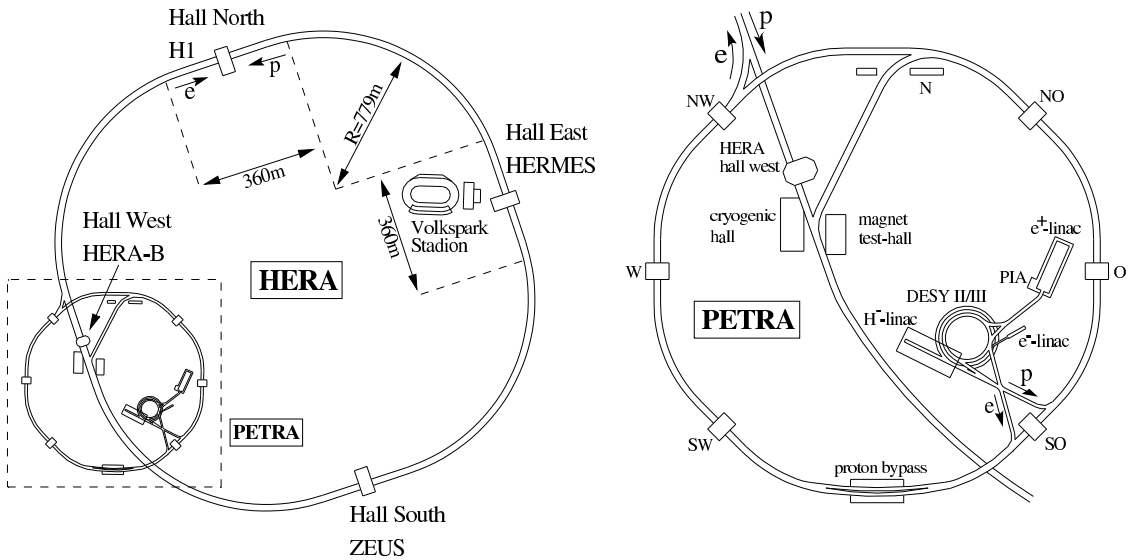

Figure 2.1 Left: *The HERA storage ring.* Right: *The pre-accelerator PETRA.*

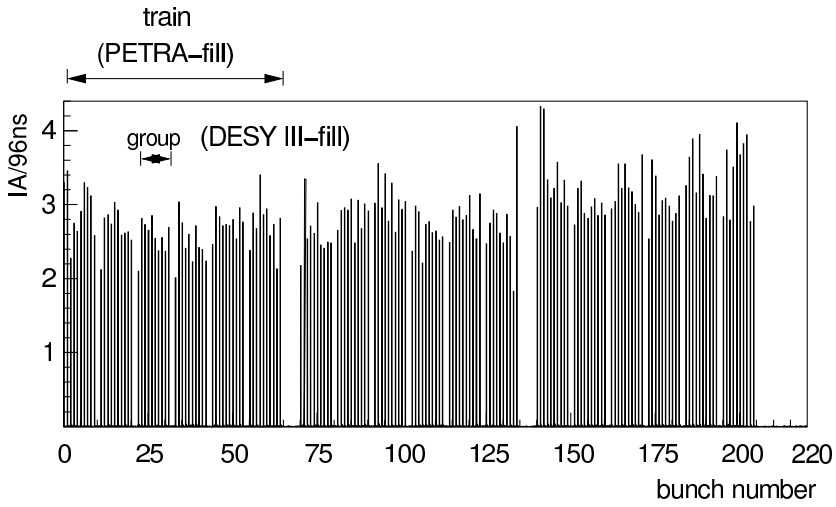

Figure 2.2 *Typical bunch structure or spectrum at HERA.*

2.3 The HERA-B Spectrometer

The HERA-B detector was a state-of-the-art forward spectrometer. It had a large angular acceptance. The complexity of the detector was attributable to the high granularity that was required to cope with the high particle densities. The HERA-B experiment used a total of eight target wires made of different materials. The targets were introduced into the halo of the proton beam without disturbing the main beam [20]. The main spectrometer was built for tracking and particle identification. Each part had its share of detector components as listed below:

- The tracking system
  - The Silicon Vertex Detector
  - The Magnet
  - The Inner Tracker
  - The Outer Tracker
- The particle identification system
  - The Ring Imaging Čerenkov counter
  - The Transition Radiation Detector
  - The Electromagnetic Calorimeter
  - The Muon identification system

Figure 2.3 shows schematics of the top and side views of the HERA-B spectrometer. In this section, each of the detector components and their properties are described.

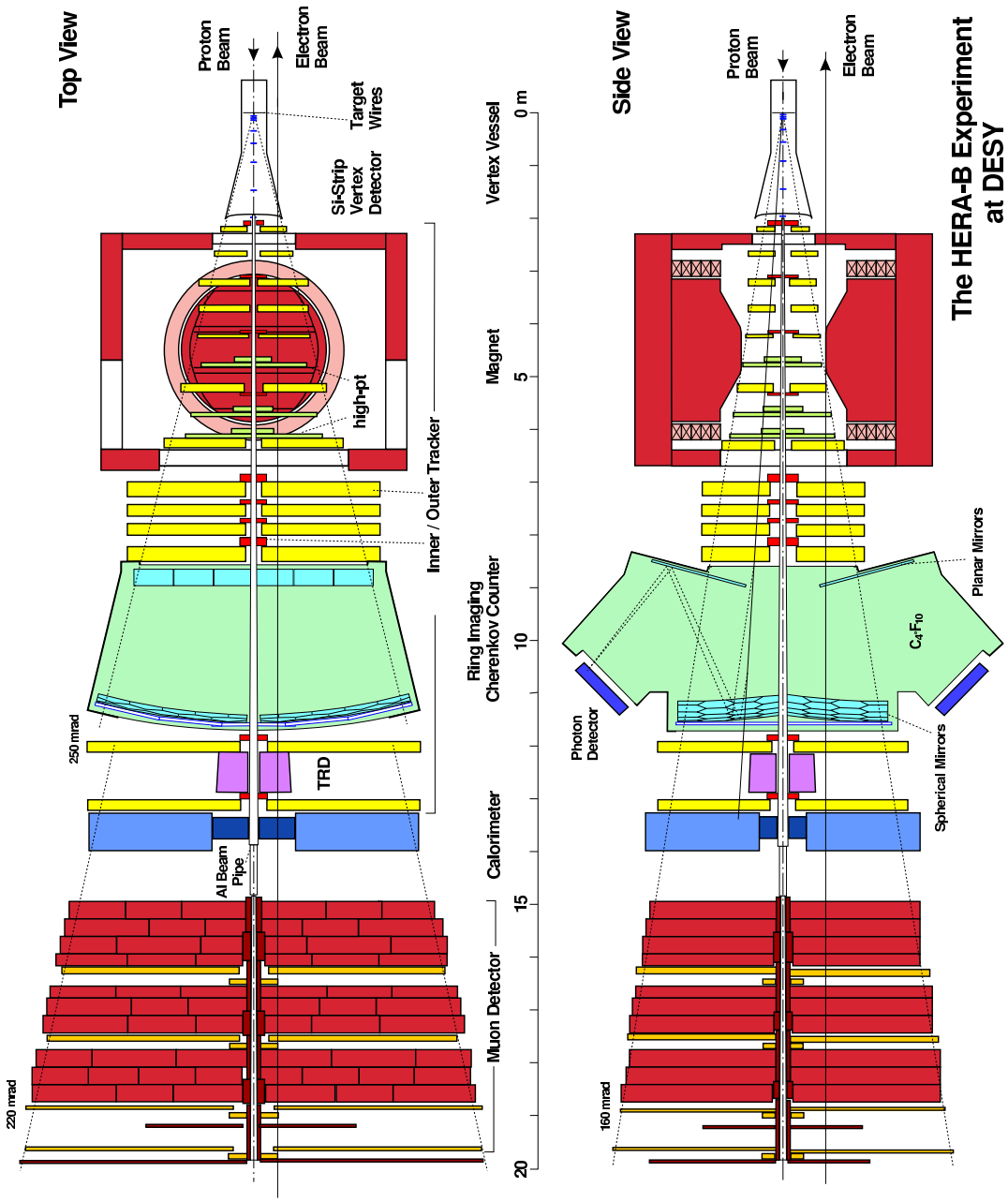

Figure 2.3 *Schematic diagram of the HERA-B Spectrometer from the top view and the side view.*

2.3.1 The Target System

HERA-B was a fixed target experiment. The target system in HERA-B consisted of wires and ribbons made of different materials. The interactions in HERA-B were produced by inserting the target wires into the halo of the HERA proton beam. The beam halo consists of protons that are slowly drifting away from the beam. This drifting beam is normally removed by collimators. HERA-B was able to achieve a high interaction rate by colliding the halo protons on the target before the halo protons were removed.

The interaction rate at HERA-B was designed to be 40 MHz. The filled proton bunches pass the target wires at only 8.5 MHz ($= 180/220 \times 10.4$ MHz). Therefore, an average of 4.7 interactions per bunch crossing had to be achieved. It was achieved by introducing eight target wires simultaneously as in the schematic view of the target system in Figure 2.4. The eight wires were mounted in two stations

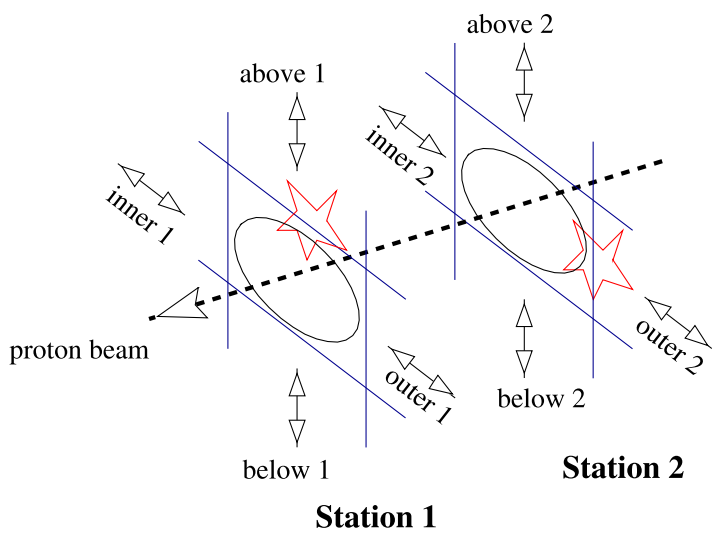

Figure 2.4 *Schematic view of the HERA-B target system with naming conventions.*

separated by approximately 4 cm. Each wire was attached to its own target fork to allow independent movement. This property helped in adjusting the interaction rate on each target. Four scintillating hodoscope counters were placed behind the RICH

to monitor the interaction rate [21]. If the rate was too high, then target wires were retracted slightly and vice versa. The wire position adjustments were done ten times per second and the stepping motors were able to move a wire by as little as 50 nm. To ensure equal number of interactions on each target, a charge integrator was connected to each target which measures the charge produced by δ electron generation and accordingly the interactions were adjusted on each target wire within 10%. Typically the wires were operated at a distance of 3−5 times the beam width (≈ 400 μm) from the center of the beam.

Table 2.1 *Target material and dimensions used during the December 2002 runs.*

Target Number	**Wire Material**	**Wire Dimensions**
above I	Aluminium	ribbon 50 μm $\times$ 500 μm
below I	Carbon	ribbon 100 μm $\times$ 500 μm
inner I	Tungsten	round wire 50 μm diameter
outer I	Titanium	round wire 50 μm diameter
above II	Palladium	round wire 50 μm diameter
below II	Titanium	round wire 50 μm diameter
inner II	Carbon	ribbon 100 μm $\times$ 500 μm
outer II	Carbon	ribbon 100 μm $\times$ 500 μm

The target materials used for this analysis include Carbon (Below I), Titanium (Below II) and Tungsten (Inner I). The main reason behind using various target materials was to find the best compromise between B^0 production and detector occupancy [22]. Also it was believed that production of B^0 increases with increasing mass number 'A' of the nucleus. (The results on B-studies are not yet clear). The various target materials definitely helped in studying the A-dependence of particle production for several other particles. Table 2.1 lists the target materials and their dimensions used during the December 2002 run period.

2.3.2 Silicon Vertex Detector

The Silicon Vertex Detector (SVD) was at that time, a state-of-the-art component of the HERA-B detector. The SVD was a strong component of the detector because it provided the co-ordinates for track reconstruction before the magnet. This property allows precise vertex reconstruction, which plays an important role in the present analysis and also for studying B decays. The design requirement on the resolution of the SVD was well below 10% of the $B-$decay length(9 mm) along the forward z direction. The corresponding transverse resolution on both x and y directions were required to be within 20-30 μm. Figure 2.5 shows a schematic view of the SVD.

The SVD was built from 64 double-sided silicon micro-strip detectors(MSD) arranged in eight superlayers each divided into four quadrants with their planes perpendicular to the beam direction. These detectors were calibrated to provide spatial resolution better than 10 μm in the direction orthogonal to the length of the strip [21]. Three dimensional capabilities are obtained by implementing at least three differently projected views. To reconstruct the primary and secondary vertices with high precision and to have the largest angular coverage possible the detectors had to be as close to the target as possible. A minimum amount of material had to be used in order to minimize effects from multiple scatterings.

The first seven superlayers of the SVD were placed inside a large steel vessel which is a part of the HERA storage ring [22]. The vessel also contained the target system. The detector module of each quadrant of a superlayer consisted of two double-sided silicon layers housed in a"Roman pot". The Roman pot arrangement allowed the SVDs to be retracted during injection. The detectors were moved after each fill to within 10 mm of the beam which provided an angular coverage of 10 to 250 mrad. The steering system attached to each quadrant plane of the SVD allowed the SVD to be aligned to the same position to within 1 μm. Each super layer had different angular coverage. The eighth and the last super layer was not movable and was located two meters from the target system just before the magnet so that all charged tracks have a position measurement just before entering the magnet.

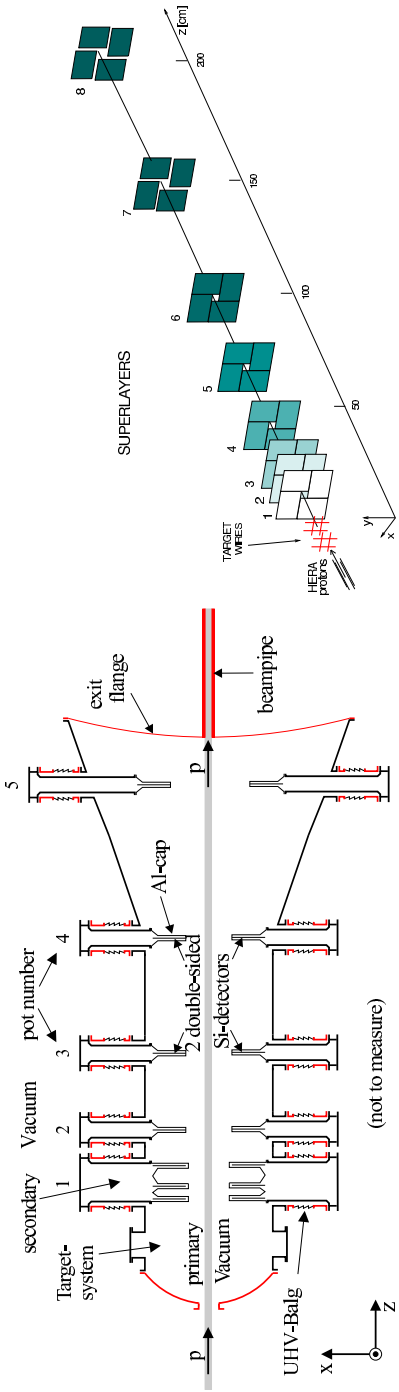

Figure 2.5 Left: *Schematic view of the silicon vertex detector and the super layers, with the last super layer after the exit flange,* Right: *The quadrant structure and super layer numbering.*

The silicon layers were made from 280 μm thick n-type material and had an active area of 50×70 mm^2. The readout pitch was 50 μm. The two sides of a double layer were orthogonal and had 1024 and 1280 readout strips, respectively. The strips were rotated by $\pm 2.5^\circ$ about the vertical/horizontal layer in order to get very good pattern recognition. A resolution of 12 μm was achieved along the x and y directions for reconstruction of every hit with an efficiency of 98%. Primary and secondary vertices were reconstructed along the z axis with a resolution of 500-700 μm [22, 7].

2.3.3 The Magnet

The design of the spectrometer magnet influences and determines the structure of the whole spectrometer. It was a large single magnet. The magnet aperture was designed to achieve a large geometrical acceptance, ≈ 200 mrad, as seen from the target. The magnet provided a field integral of 2.2 Tm at an estimated power consumption of 1.1 MW and was built using the ARGUS magnet coils [21]. The magnet was built to get the flux return concentrated in the forward region and its shape allowed easy access to the chambers from the sides. An iron skirt at the entrance of the magnet protected the vertex detector from the stray magnetic fields simplifying, triggering and pattern recognition. The mass resolution of the spectrometer depends on the value of the field integral that factors in the momentum measurement from the tracking system. The mass resolution was ≈ 8 MeV/c^2 for $B \to J/\psi K^0_S$.

The main challenge faced during the installation of the magnet was the shielding of the electron beam. It was handled by using two metal pipes of high permeability surrounding the electron beam to provide the shielding. A set of solenoidal coils were required to avoid saturation of the inner pipe. A groove in the lower pole face of the magnet funneled the magnetic flux sideways, which helped in reducing the shielding requirements.

2.3.4 The Inner Tracker

The Inner TRacker (ITR) provided tracking between 10 mrad to 100 mrad angular coverage. The ITR was made of several layers of Micro Strip Gas Chambers (MSGC). A MSGC detector is shown in Figure 2.6. The ITR consisted of a 400 μm thick glass wafer with thin anode and cathode strips of gold placed in a gas filled volume (70% Ar and 30% CO_2). A large drift voltage was applied between the anode, the top of the chamber and the cathode strips. The passage of a charged particle would ionize the gas and the ionization electrons would drift to the anode strips [21, 22]. The large electric field around the 10 μm wide anode strips provided a strong gas amplification of the primary electrons so that a large signal could be read out from the anode strip. The gold electrodes on ordinary glass substrates used in conjunction with clean gas conditions drastically reduced the aging in MSGC's. This allowed the ITR to provide enough rate capability.

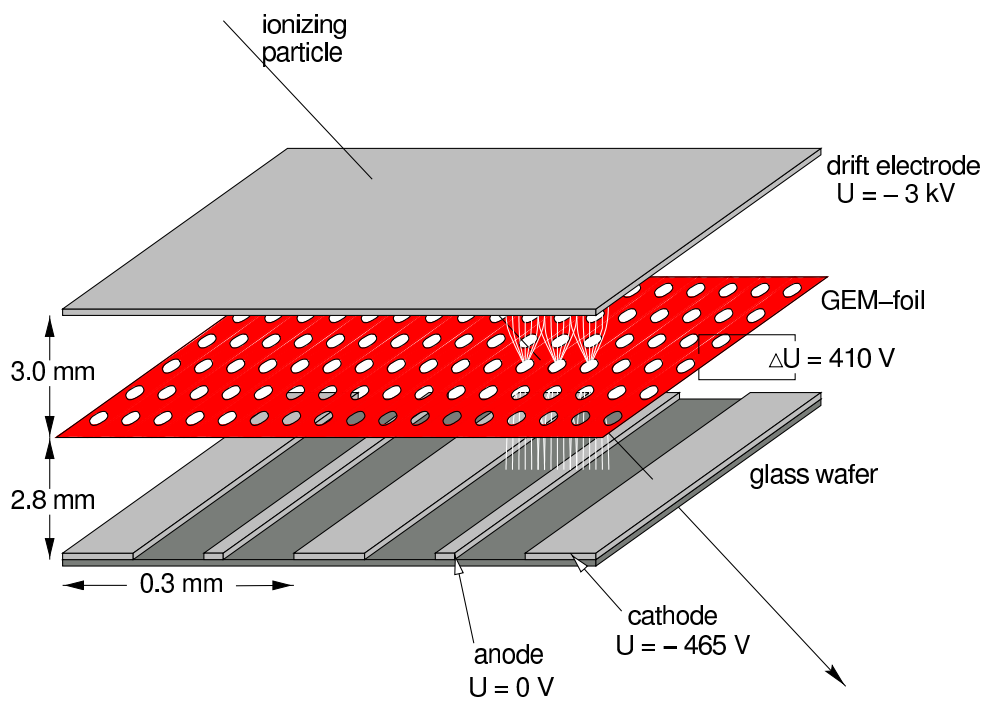

Figure 2.6 *Schematic view of the inner tracker(ITR) with the GEM layer.*

A typical layout of a MSGC inner tracking station is illustrated in Figure 2.7. The entire system consisted of 48 (single) layers of MSGCs, arranged in 11 superlayers with three views (0° and ±5° stereo), with a total of 192 individual detectors. The tilt in the layers left the horizontal coordinate intact which satisfied the requirement of a very good precision in the horizontal plane for the momentum measurement. The first tracking station was in addition equipped with Silicon microstrip detectors to cover the low angle (10 mrad aperture) region. The ITR had four superlayers inside the magnetic field and six superlayers behind the magnet, four of which were used as part of the First Level Trigger(FLT).

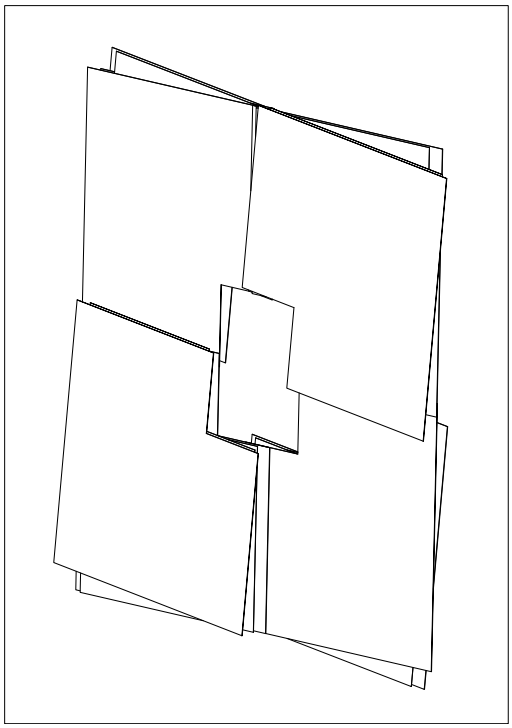

Figure 2.7 *Schematic view of one layer of the ITR with 12 detector modules arranged to provide 3 layers of views.*

The ITR had an intermediate Gas Electron Multiplier (GEM) layer. The layer allowed reduction of voltage in the cathodes to minimize the sparks created by some heavily ionizing particles, avoiding destruction of the chambers. The GEM layer was a 50 μm thick 'Kapton' foil with thin copper layers on each side. The layer was

filled with holes. By applying a voltage potential over the layer, a gas amplification of a factor 15-100 takes place in the holes while the amplification in the MSGC layers was about 200-1000. The readout pitch of the ITR layers was 300 μm which gave an overall resolution of about 90 μm. The hit efficiency was measured to be 91-97% depending on the quality of the GEM layer.

2.3.5 The Outer Tracker

The angular acceptance of the Outer TRacker (OTR) overlaps that of the ITR extending up to 250 mrad in the horizontal plane and 160 mrad along the vertical plane. The OTR was made of Honeycomb drift cells.

The schematic view of an OTR module is shown in Figure 2.8. The Honeycomb drift cell consisted of a 25 μm gold-plated tungsten anode wire and a 50 μm polycarbonate (Pokalon-C) coated on the inside of a cathode drift cell by thin gold layers. The gas mixture used was $Ar/CF_4/CO_2$ which kept the drift time below a single bunch crossing and helped minimize aging. The cell size was 5 mm in the modules closest to the beam pipe, and the cell size was 10 mm for those that were farther away. This difference in cell size maintained the occupancy at 40 MHz interaction rate below 20%. The readout of the OTR was equipped with Time-to-Digital converters (TDC). This drift time information helped measure up to a left-right ambiguity [8], how far from the anode the charged particle passed.

The OTR had three more superlayers than that of the ITR inside the magnet. Behind the magnet the OTR had six superlayers exactly at the same z positions as the ITRs. Similar to the ITR, the OTR also had several layers put together with slight tilts within 5°. Due to the large size of the OTR, it was built using several modules. The OTR was also used as part of the First Level Trigger (FLT). For the FLT, only OTR modules with double layers were used to achieve higher efficiency.

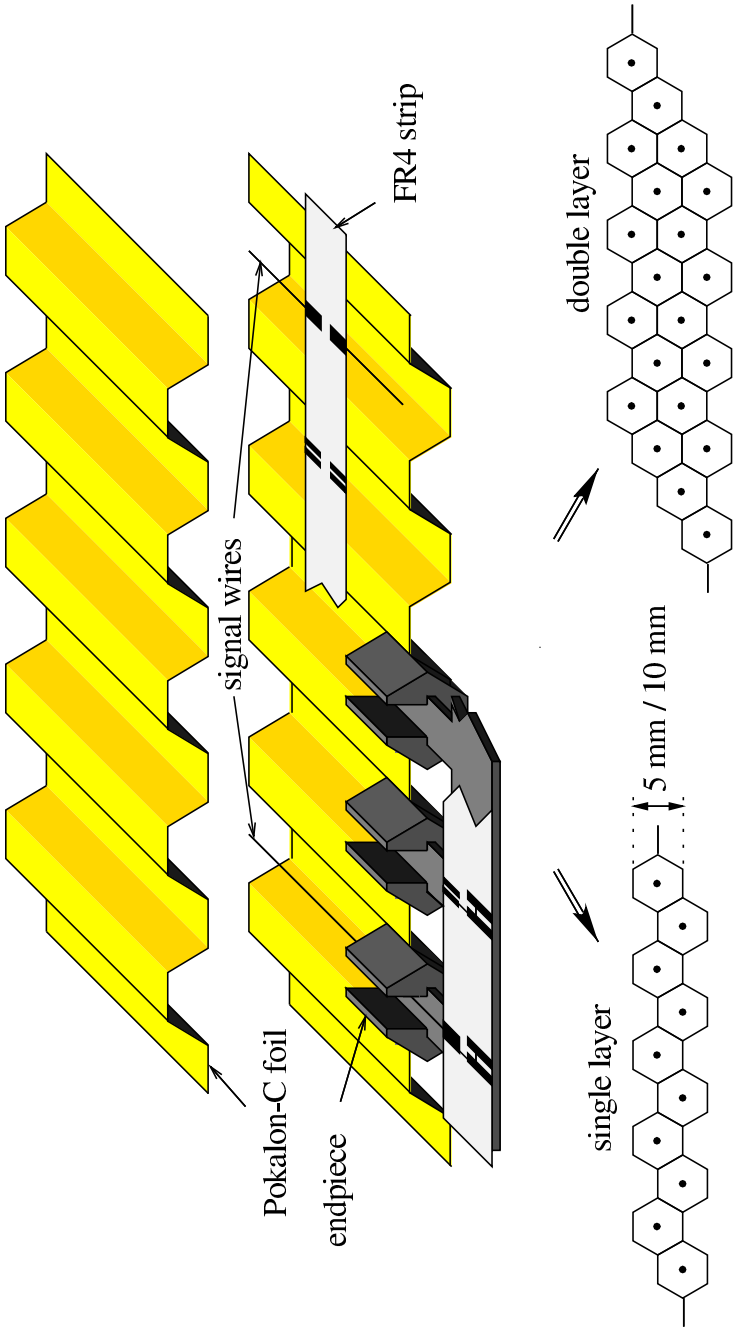

Figure 2.8 *Schematic view of the OTR's honey comb drift chambers.*

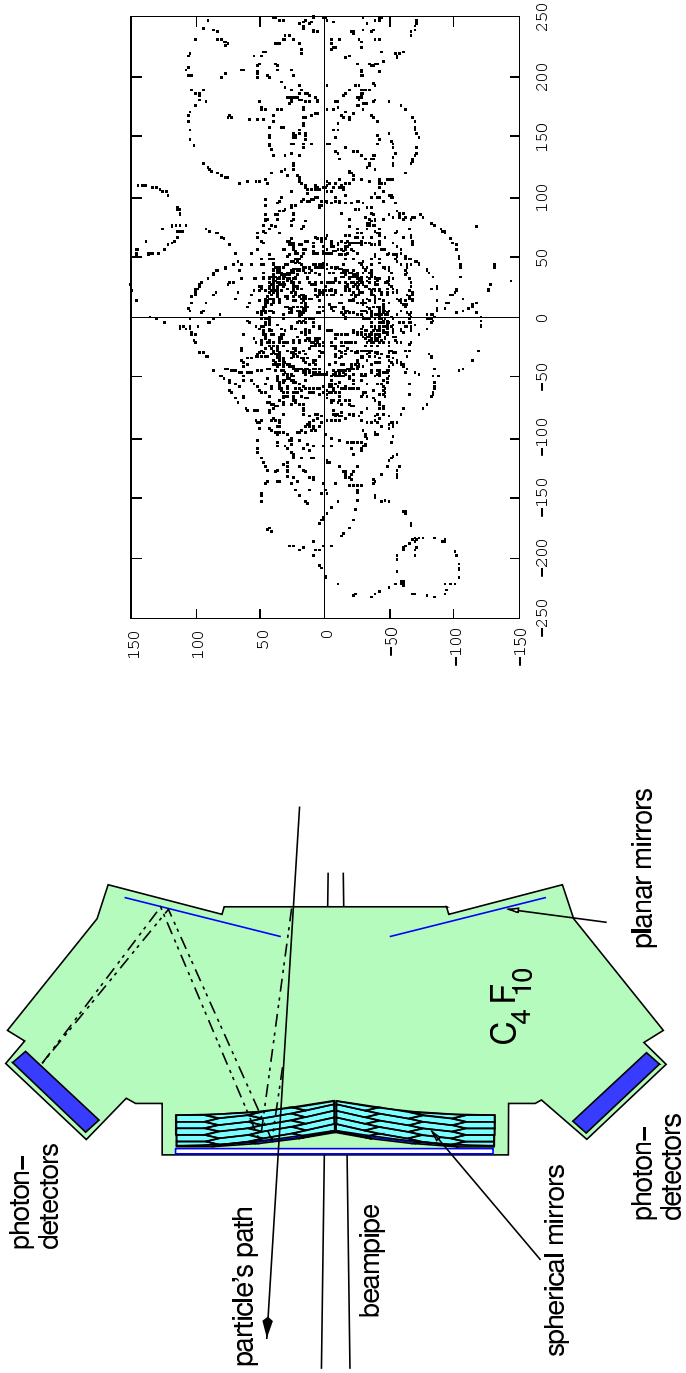

Figure 2.9 *Schematic view of the RICH detector*.

2.3.6 The Ring Imaging Čerenkov Detector

The HERA-B Ring Imaging Čerenkov Detector (RICH) was a very important part of the spectrometer because it provided charged-hadron particle-identification. A schematic of the RICH is shown in Figure 2.9.

Principle of RICH

When high energy charged particles traverse dielectric media with $v > c/n$ [3], where n is the refractive index of the medium, light is emitted by excitation of atoms in the form of coherent radiation at a fixed angle with respect to the trajectory - a phenomenon known as the Čerenkov effect. The angle of emission of photons, called the Čerenkov angle, is given by

$$\cos\theta = \frac{c\ t/n}{\beta c\ t} = \frac{1}{\beta n}. \tag{2.1}$$

This emitted radiation is detected by a two-dimensional array of photo-multiplier tubes. Each photomultiplier detection was considered as a hit. Several of these hits from a track were reconstructed to form rings. The center of the ring fixes the line of the track and direction. This is the working principle of the RICH. Threshold Čerenkov counters can be used to discriminate between two relativistic particles of the same momentum p and different masses m_1 and m_2, if the heavier particle (m_2, say) is just below threshold. The production rate of photons gives rise to an inverse relation between the square of the Čerenkov angle and the square of the momentum [3, 5]. It is given by the equation:

$$\theta^2 \approx \theta_0^2 + \frac{m^2}{p^2} \tag{2.2}$$

where θ_0 is the Čerenkov angle for $\beta = 1$.

Construction

The HERA-B RICH was made of a large vessel filled with 108 m^3 C_4F_{10} as a radiator gas with a radiation path length of 2.8 m and refractive index, $n = 1.00137$.

The radiator vessel, made from stainless steel plates with 1 mm aluminum particle entrance and exit windows to minimize multiple scattering, is placed about 8.5 m downstream of the target. The radiator gas is kept at 2.5 mbar overpressure relative to ambient pressure [21, 7].

The main imaging device of the RICH was a spherical mirror placed inside the radiator vessel with the center of the sphere near to the target and a radius of curvature of 11.4 m. The mirror consisted of 80 full or partial hexagons made from 7 mm thick Pyrex glass coated with 200 nm of aluminum and 30 mm of MgF_2. The mirror was split horizontally, and both halves were tilted by 9° away from the beamline. Apart from the spherical mirror, the RICH had a set of two planar mirrors, composed of 18 rectangular elements that translated the focal surface to the photon detector area above and below the radiator vessel. All 80 spherical and 36 planar mirrors were mounted on a rigid, low mass support structure inside of the radiator volume [8]. Each mirror had the ability to be adjusted by individual stepper motors from the outside. The planar mirrors helped reduce the width of the RICH and prevented overlap with the OTR.

The photons were detected by two-dimensional array of photomultiplier tubes (PMT) contained in 14 supermodules that used a set of lenses to increase the acceptance of the photomultipliers. The photomultiplier tubes had a cell size of 9×9 mm^2 and their angular accuracy is ≈ 0.46 mrad calculated using the equation,

$$\sigma_{cell} = \frac{D}{\sqrt{12} \cdot R/2} \tag{2.3}$$

and 18×18 mm^2 in the outer regions with angular accuracy $\approx$0.9 mrad. The average number of detected photons depends on the Čerenkov angle, and can be expressed as

$$N \approx N_0 \cdot T \cdot < \theta >^2 \tag{2.4}$$

where N_0 is the parameter defined by various other parameters such as the transmittance T of the gas, vessel walls, and lenses ε_T, the reflectivity of the mirrors ε_R, and the quantum efficiency of the photomultipliers ε_{PMT}. The cell size and dispersion in the radiator gas are main contributors to the total single photon resolution which is

$\approx$ 0.7 mrad for the inner cells and $\approx$ 1.0 mrad for the outer ones. Other optical aberrations also affect the resolution but altogether make < 0.5 mrad error.

Performance of the RICH detector

The purpose of the RICH detector was to identify high velocity particles. The RICH acceptance was adjusted for particles that originate from short decays, near the target and have a momentum above the radiation threshold. The Čerenkov radiation threshold of the pions and kaons for the RICH's radiator gas are 2.7 GeV/c and 9.6 GeV/c, respectively. For $\beta = 1$ particles, the Čerenkov angle is 52.4 mrad as shown in Figure 2.10. The difference in Čerenkov angle between π - K is 0.9 mrad at 50 GeV/c. The Čerenkov angle distribution for particles detected by the RICH

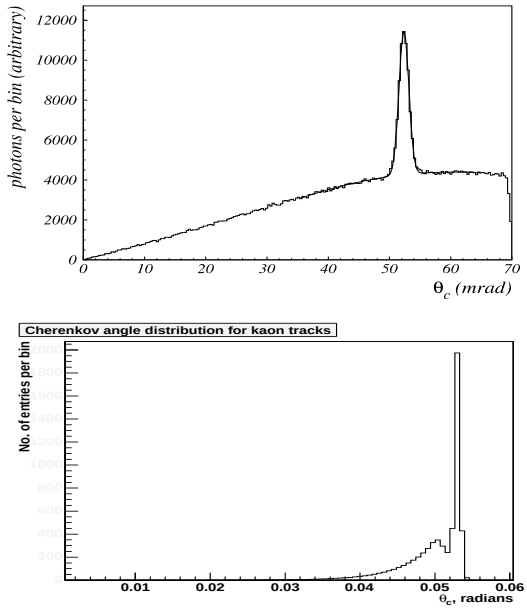

Figure 2.10 *Čerenkov angle distribution.*

[23, 24] looks as shown in the Figure 2.10a. The Čerenkov angle depends on various gas parameters such as temperature, pressure, and other thermodynamic factors [7]. Using the Clausius-Mossotti relation that describes the dielectric behavior of a gas,

a suitable dependence between the Čerenkov angle and the gas parameters were derived. This further helped in deriving a pressure/temperature correction factor for the Čerenkov angle measurements.

Particle Identification

Two different methods were used for particle identification (PID) purposes. A ring-search-based and a track-based algorithm. In the ring-search method, rings are reconstructed and matched to tracks, while in the track-based algorithm tracks from SVD and OTR hits are used to find rings. The two methods were used in a complimentary way. The track based algorithm for particle identification of every track is called the extended likelihood method. The plot of Čerenkov angle versus the momentum for data shows a clear separation of protons, kaons, pions, and electrons as can be seen in Figure 2.11. Each particle species is distributed over a band and has different radiation thresholds because of their masses [24]. By using the χ^2 fit for the tracks the probability of a particular track being a pion or a kaon or some other charged particle is calculated. This probability is called the particle likelihood. As an example to show the performance of the RICH in particle identification, Figure 2.12 shows a clear reduction in background for $K_S^0 \rightarrow \pi^+\pi^-$ invariant mass spectra drawn with and without using harder cuts on particle ID.

2.3.7 Electromagnetic Calorimeter

The Electromagnetic CALorimeter (ECAL) works on the principle of the total-absorption of the energy of an interacting charged particle. In the ECAL, an incident particle of high energy interacts with a large detector mass, generating secondary particles which in turn generate tertiary particles and so on, until all of the incident energy appears as excitations in the medium of the detector [3]. For electrons and photons of high energies, a combination of bremsstrahlung and pair production occurs as cascade showers. The longitudinal development of such a shower traverses several radiation lengths and ceases as soon as it has not enough energy

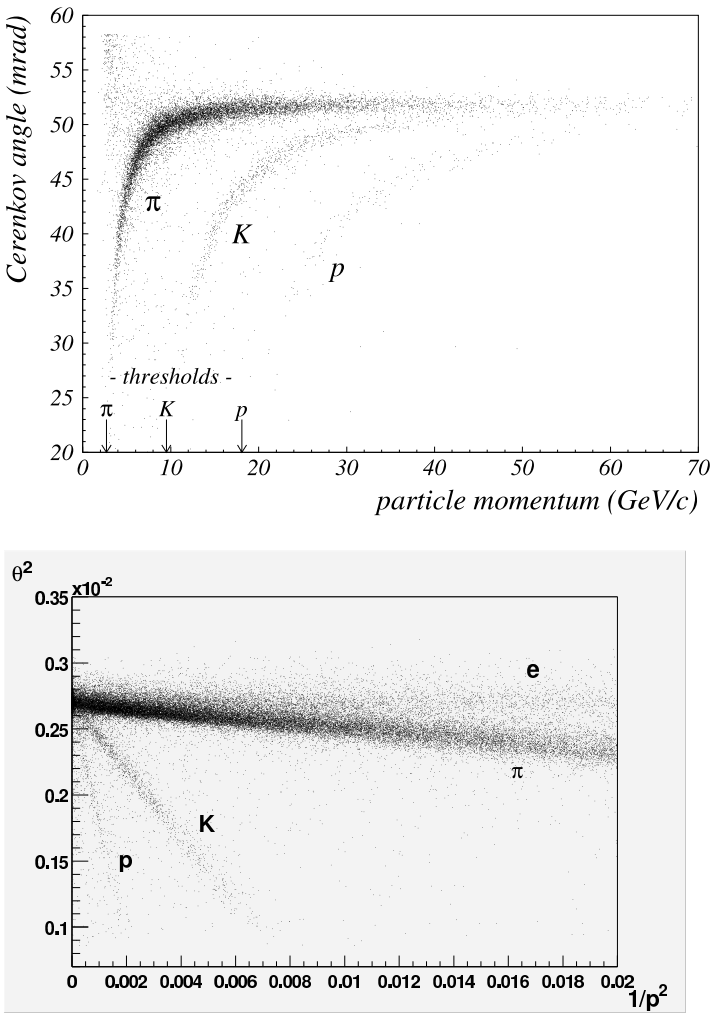

Figure 2.11 *Čerenkov angle versus momentum distribution.*

for the bremsstrahlung or pair production process to take place. The maximum of the shower occurs at a depth increasing logarithmically with the primary incident energy, E_0. The number of shower particles and the total track-length integral is proportional to E_0. So the ECAL allows one to measure energy and position coordinates of the electrons and photons. Photons do not leave a track in the tracker while the electrons do. The measured momentum p should match the measured energy E within measurement uncertainities. For hadrons, the ECAL measures only a small part of the energy and therefore $E/p \ll 1$.

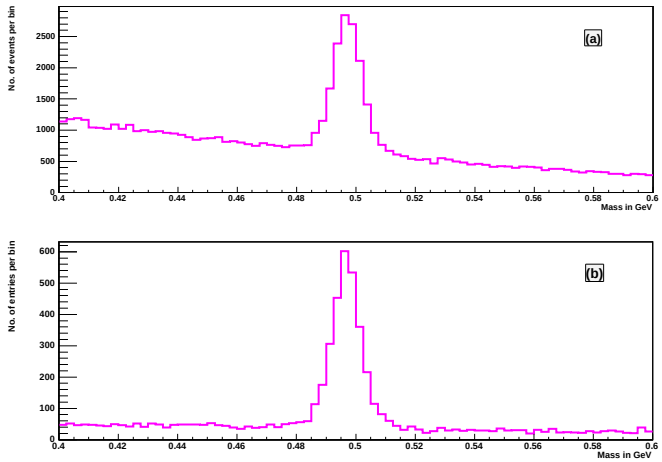

Figure 2.12 *Example showing the effect of particle identification by the RICH in* K_S^0 *detection.*

The ECAL at HERA-B, shown in Figure 2.13, was built as a sampling calorimeter with a sandwich structure where the absorber plates were interleaved with plastic scintillator layers. The calorimeter was divided into modules with a front face of 11.2×11.2 cm^2. In total it had 56 modules in the horizontal direction and 42 modules in the vertical direction providing full angular acceptance. To keep the shower of an electron or a photon confined laterally to a few cells, the inner ECAL used a tungsten alloy as absorber material while the middle and the outer ones used lead. To keep occupancies below 10%, the modules were further divided into cells of varying sizes. In the innermost part, a module consisted of 25 cells. In the middle part, a module had 4 cells and in the outer part, the module was a single cell.

A shower was expected to deposit energy in several neighbouring cells, and the reconstruction therefore combined cells with energy depositions into clusters and used them as candidates for electrons and photons. For the inner ECAL the energy resolution, $\sigma(E)$ was

$$\frac{\sigma(E)}{E} = \frac{17\%}{\sqrt{E/\mathrm{GeV}}} \oplus 1.6\% \tag{2.5}$$

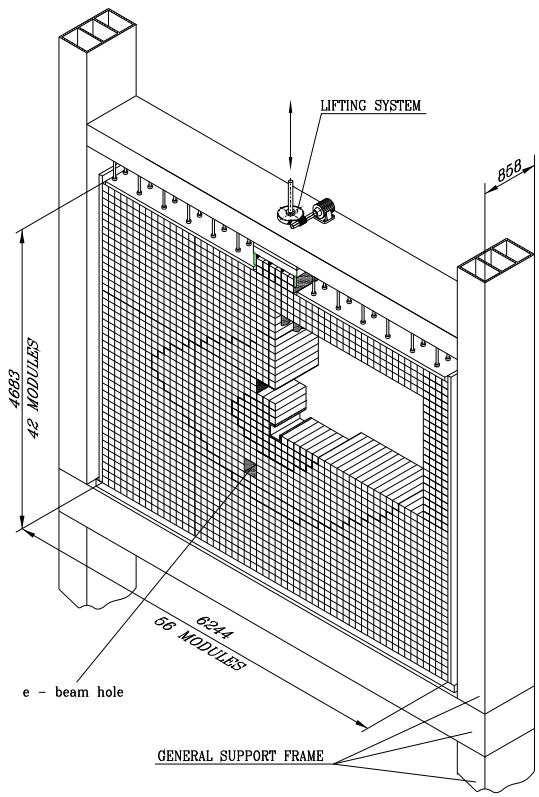

Figure 2.13 *Schematic view of the ECAL.*

and for the middle and the outer ECAL sections, the energy resolution was

$$\frac{\sigma(E)}{E} = \frac{9.5\%}{\sqrt{E/\mathrm{GeV}}} \oplus 1.0\% \tag{2.6}$$

The interaction triggered events used in this dissertation required at least 1 GeV energy deposition on the ECAL for event selection.

2.3.8 The Muon Detector

The muon detector (MUON) system was also an important part of the HERA-B experiment. The MUON requires the least amount of extrapolation beyond well-known and field proven experimental techniques. The MUON had an angular coverage of 220 mrad. The stereo angle for the detector was 20°.

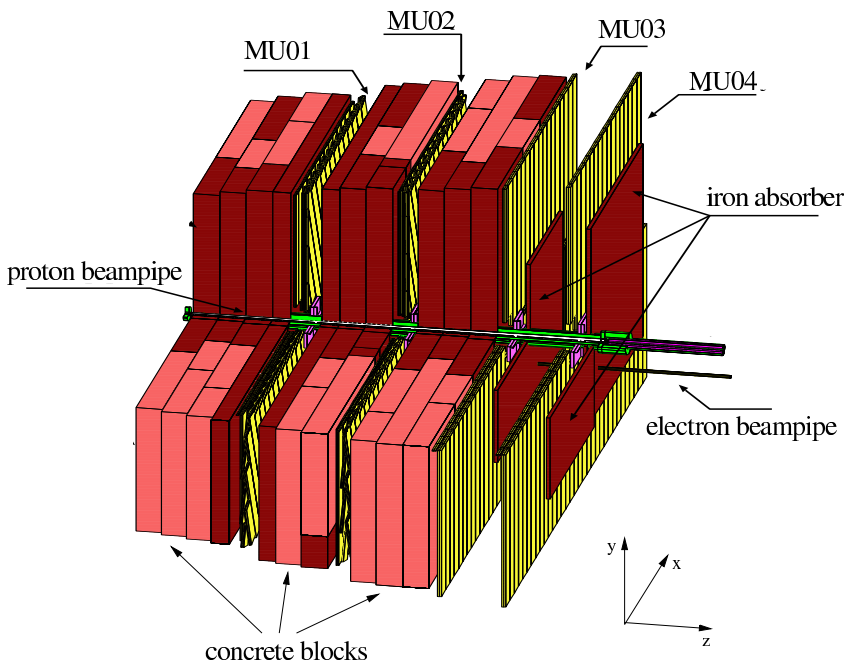

Figure 2.14 *Schematic view of a muon detector.*

The MUON used identical types of rectangular chamber modules for all parts of the detector as shown in Figure 2.14. The MUON consisted of four tracking stations behind the calorimeter that were separated from each other by one meter thick walls of concrete and iron. The absorber walls were introduced to stop the hadrons and allow only muons with momentum larger than 5 GeV/c to penetrate all the walls. The muons leave signals in the four tracking stations through penetration and are identified quite reliably in this manner.

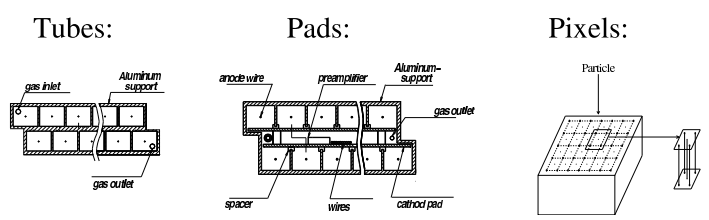

Figure 2.15 *Schematic view of the muon chamber module.*

The chamber modules near the 0° region consisted of gas pixel chambers with short (3 cm) wires along the beam direction, with cells defined by four thick potential wires. The gas pixel chambers were used to meet the requirement of higher granularity. The pixel chambers had the advantage of using the wire signal instead of weaker and slower cathode signals. The gas mixture consisted of 80% Ar and 20% CF_4. The passage of a particle ionizes the gas and the resulting avalanche electrons drift towards the anode and induce a signal on the wire.

In the outer region, the MUON consisted of proportional tube chambers. The tubes were 16 mm wide and in order to have high hit efficiency all layers are implemented as double layers with the second layer shifted half a cell size as shown in Figure 2.15. The drift time of the cells are not read out, only the presence of a signal is recorded.

2.4 HERA-B Data Acquisition

HERA-B was a finely segmented spectrometer with more than 500,000 channels to be read out for every event. The number of channels and the amount of data per channel are described in Table 2.2. In total, 470 kByte of data were produced per

Table 2.2 *The number of channels and the detector component-wise data per channel in HERA-B.*

Detector	**# of Channels**	**Bits per channel**
VDS	176,000	8
ITR	135,000	8
OTR	120,000	8
RICH	27,520	1
ECAL	5,800	16
MUON	30,814	1

bunch crossing, which at the 10.4 MHz bunch crossing rate gives almost 5 TByte per second. This data cannot be stored by any means, even after the suppression of empty channel readouts. Hence, the data had to be filtered. The actual rate of

interesting events, for example b-quarks, are produced once in a million events. Such a low rate of interesting events as compared to the high input rate, required the event filtering to maintain a high efficiency. This reduced the event rate from 10.4 MHz to 20-50 Hz of events that were stored on tape. The event filtering was done using a multi-level "trigger and buffer" system that used an increasing amount of data and processing power on a decreasing amount of events as events pass through the system. The description of the HERA-B trigger and data acquisition system in this chapter corresponds to the initial design. In reality, most of the trigger was operated as per design, except for minor changes such as combining two or more levels into one.

2.4.1 Front End Electronics

The above-mentioned rates required a very good readout hardware to achieve high efficiency for recording all the interesting events. The readout hardware was expected to amplify, shape, digitize, compare, and trigger to get a reasonable output from the detector. To achieve this the following electronics were used for the respective detector components:

- **VDS** - Used the HELIX chip to read out the micro-strips. Each HELIX chip handles 128 input channels and each channel consists of a charge integrating preamplifier followed by a pulse shaper, which stores the measured charge in a pipeline of 141 capacitors.
- **ITR** - Also used the HELIX chip.
- **OTR** - Used the ASD8 chip to read out. Each chip provides preamplification, fast signal shaping with tail cancellation and a discriminator for eight channels. The signal threshold for each of the eight discriminators is set by external voltage sources. The output is then fed through a Time-to-Digital-Converter (TDC) to have a distinction between track hits to make coincidences later in the trigger.
- **RICH** - Used the photomultiplier tubes readout.

- **ECAL** - Also used the photomultiplier readout.
- **MUON** - Also used the ASD8 chips.

The front-end electronics are an intricate part of the trigger system which is explained in the next section.

2.5 The HERA-B Trigger System

As a brief overview for the HERA-B trigger, one should mention that the main physics channel for the HERA-B trigger design was based on the so-called golden decay, $B_d^0 \rightarrow J/\psi K_S^0$. K_S^0 mesons are very common in hadronic inelastic interactions and therefore they are not well suited for triggering purposes. The golden decay was triggered using J/ψ. J/ψ mesons decay weakly to muon or electron pairs and these lepton pairs having an invariant mass corresponding to the J/ψ mass (3.097 GeV/c^2) were considered to be a good trigger. A signature for the trigger system was either the high transverse momentum (0.5-3 GeV/c) of the muons, and electrons, or the high invariant mass ($>$ 2.0 GeV/c) of these pairs. Apart from the J/ψ trigger, HERA-B also used an interaction trigger during its run period to study various other particles and to study the functionality of the detector. To filter the data using the trigger conditions above, a multi-level trigger and buffer system was designed [25]. A pretrigger got rid of the empty readouts, and generated seeds for detected tracks of non-emtpy events which were fed into the First Level Trigger.

The *First Level Trigger* (FLT) looked at the data from every event seeded by the pretrigger. It was designed to find and track leptons and hadrons with high transverse momentum through the tracking chambers behind of the magnet. The *Second Level Trigger* (SLT), which looked at a lesser amount of data, refines the FLT tracks in the tracking chambers behind the magnet by tracking them through the magnet and vertex detectors, and reconstructs the primary and secondary vertices for the event. After the SLT, a *Third Level Trigger* (TLT) verifies the reconstructed primary and secondary vertices. The *Fourth Level Trigger* (4LT) does a complete

event reconstruction and classifies each event into different physics classes, making it easy for the final-user analysis. At this stage, the output rates becomes 50 Hz. Data storage becomes possible at this rate. A flow chart of the output rate for the

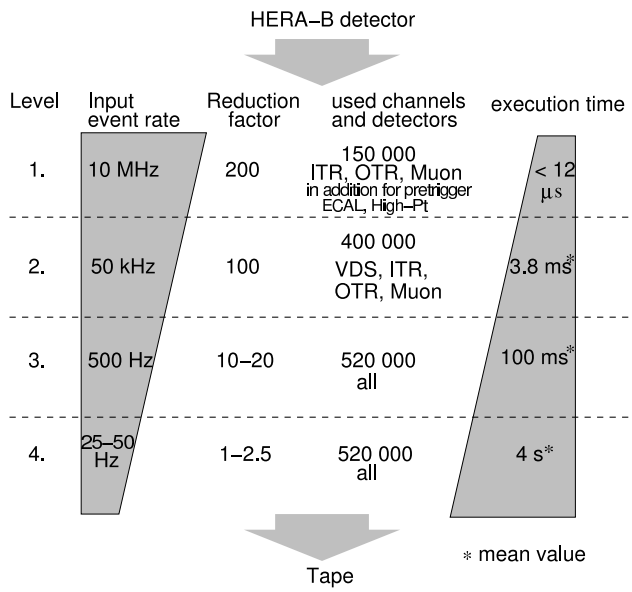

Figure 2.16 *Flow chart representing the output rates for the four trigger levels.*

four trigger levels [22] is described in Figure 2.16. A functional description of the four trigger levels including a description of the pretriggers, is given in detail in the following subsections.

2.5.1 Pretriggers

The pretriggers do not reject or accept events, though they cut off empty events. The pretriggers are designed to serve as an input to the First Level Trigger where the initial good-track search, rejection and acceptance of events takes place. The FLT looked for input from various detector components, such as the ECAL, MUON, High-p_T chambers and each had their own pretrigger.

The ECAL pretrigger based its seeds for the FLT on highly energetic clusters in the calorimeter. For each cell in the calorimeter an individual energy threshold E_c

was set. If the energy in a cell was higher than E_c, a cluster search was done. Again, when the energy of the neighbouring eight cells added to the energy of the central cell exceeded a second threshold, a pretrigger seed was generated and fed to the FLT. Similarly, the MUON pretrigger based its seed on muons with momentum larger than 5 GeV/c since only those muons were able to penetrate the thick absorber and reach the MUON layers. The pretrigger generates a seed whenever there is a coincidence between two adjacent MUON layers.

2.5.2 The First Level Trigger

The First Level Trigger (FLT) looked for lepton candidates from $J/\psi \rightarrow l^+l^-$ decays. The FLT does so by getting its seed from the ECAL and the MUON pretriggers and then a fast FLT algorithm searched for additional hits in the tracking detectors. When the FLT was processing an event, the detector data was stored in the pipeline placed in the readout electronics of the DAQ. The pipeline is 128 events deep, when associated with 96 ns between bunch crossings, it means that the FLT has 12.3 μs to decide whether an event should be accepted or not. If the FLT decision was too late, the event data would have already been overwritten by a new event. To avoid such a situation, a highly parallel and pipelined architecture was designed and used.

The FLT uses a Kalman filter, as illustrated in Figure 2.17, to search for additional hits in the tracking chambers for tracks that belong to the ECAL, MUON or High-p_T pretrigger seeds. The FLT is purely a hardware trigger. Since the FLT requires coincidences from double layers, the efficiency is reduced significantly as can be seen from the ratio of the amount of selected events to the amount of input events from Figure 2.16.

2.5.3 The Second Level Trigger

The subsequent triggers after the FLT were all software triggers. The Second Level Trigger (SLT) was a farm of minimal Linux systems, and all processing of events was done on a parallel-node basis. The SLT gets its input from the FLT, and the SLT

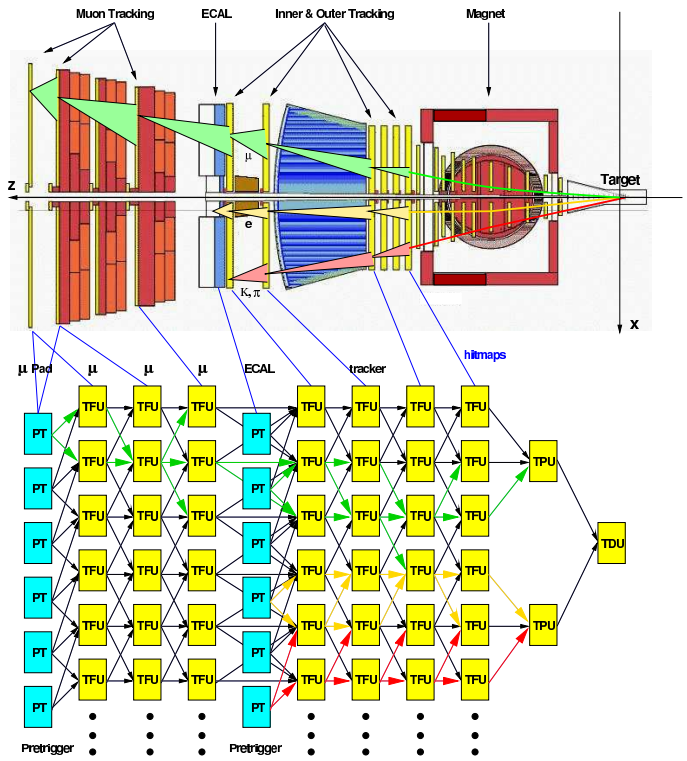

Figure 2.17 *Schematic representation of the Kalman filter used in FLT.*

algorithm searches for hits in the VDS. The SLT was more of an algorithm whose application was oriented towards a specific interest, like accepting only leptonic track pairs that have a common vertex which is outside of the target wires to look for J/ψ from B hadrons. The SLT algorithm consisted of the following:

- Slicer - The slicer removes ghost tracks by requiring a minimum number of hits in the tracking chambers behind the magnet to be lined up on an approximate straight line.

- RefitX - Applies a Kalman filter to the hits with track parameters in the xz plane and rejects those with poor χ^2.

- RefitY - Same as RefitX, except for the track parameters now chosen are in the yz plane.

- L2Magnet - Propagates the tracks from behind the magnet to the front of the MAGNET by using track parameters based on momentum and track slopes. It also searches for hits in the tracking chambers infront of the MAGNET.
- L2Sili - Follows the tracks through the VDS using the Kalman filter and does the same thing as RefitX and RefitY.
- L2Vertex - The track pairs detected by the previous algorithms are required to be detached from the target wires and should also have a common vertex within errors.

2.5.4 The Third Level Trigger

The Third Level Trigger (TLT) was also a software trigger which runs in the same process as the SLT. The difference between the SLT and the TLT was that the TLT played a more general role. Unlike the SLT which looks for events of specific interest, the TLT worked with the whole data from all the subdetectors, no matter if the vertex was outside the target wire or inside. The TLT read out the data from the Second Level Buffer (SLB) which contained output from the FLT, events which were rejected as ghost tracks and those from bad track fits, excluding those from the specific interest part of SLT.

In reality, neither the specific interest part of SLT nor the TLT were used separately. All of the output of FLT processed into SLB were directly fed as input to the fourth level trigger along with the vertex reconstruction information from the SLT.

2.5.5 The Fourth Level Trigger

The main purpose of the Fourth Level Trigger (4LT) was to provide complete event reconstruction. The events that are classified depending on the previous triggers were made available for users to do individual analysis. The explanation about the complete event reconstruction is all described elaborately in the next chapter.

Even though HERA-B's trigger system was built based on the di-lepton requirement, the interaction trigger efficiency was maintained high $\approx 99\%$. Seeding forms the basis of trigger algorithms, which in turn is a process of setting up region of interests(RoI) in the tracking system. As per the definition of the interaction (IA) trigger, 20 hits in the RICH along with > 1 GeV energy deposition in the ECAL as a requirement acted as the pretrigger seed for FLT for these events. The requirement for the hits was achieved by making coincidences from the phototubes of the RICH.

At the pretrigger stage, almost all the events satisfy this criterion. At the FLT stage, where the requirement is that there must exist valid tracks for all hits, cuts off a portion of the events. All the data after the FLT are dumped into tape drives. The data that get past the FLT were fed into the SLT and a vertex requirement for the event forms the pretrigger for the SLT. Track fitting and rejecting ghost tracks forms the main function of the SLT. Subsequently, event rate can be further reduced by the use of TLT and 4LT for the full event reconstruction that includes: event classification, data-quality monitoring, and final physics analysis.

CHAPTER 3

DATA RECONSTRUCTION

In this chapter, the data storage procedures used at HERA-B are described. The various procedures followed for reconstruction and analysis are described. A description of the "Analysis and Reconstruction Tool for Events" (ARTE) and ARTE tables are given. Monte Carlo event simulations help in determining and understanding the intricacies of the experiment. In modern high energy physics experiments, the very nature of the experiments, owing to their size and cost, require careful planning. Monte Carlo event simulations have to be done to get realistic estimates on the output of an experiment, so that, time and money can be spent in an efficient way to move forward in scientific research. A few methods and models used for Monte Carlo event simulation purposes are described. Performance checks and efficiency measurement are done using event simulation techniques. This dissertation is about measurement of cross-sections, which is closely related to the number of interactions per event per unit area quantified as luminosity. The method used to determine experimental cross-sections is described. A description of the procedure used to measure luminosity is also given. Error analysis methods to determine statistical and systematic errors form a vital part of every experiment. These methods are described in the final section.

3.1 Data Storage

Data storage forms an important part of an experiment. Data storage provides the opportunity for online and offline analysis, which need not be done realtime. The trigger system described in Chapter 2, sums up the various steps the data passes

through before storage. HERA-B had several running periods since year 2000. This dissertation uses data taken during the run period between October 2002 and March 2003. During this period, data collection was done with two different types of triggers. Most of the run period used the $J/\psi \rightarrow \mu^+\mu^-$ or $J/\psi \rightarrow e^+e^-$ *di-lepton* trigger. During December 2002, data collection was done completely using the *interaction* (IA) trigger [15] also known as the "minimum bias" trigger. The conditions that defined the two triggers used at HERA-B were:

- **Di-Lepton trigger** also called the J/ψ trigger, filters events with at least two muons or two electron candidates which were written on tape at 100 Hz.
- **Interaction trigger** selects an event if at least 20 hits appear in the RICH along with an energy deposition in the ECAL > 1 GeV. The events were written on tape at a rate of ≈ 1 kHz.

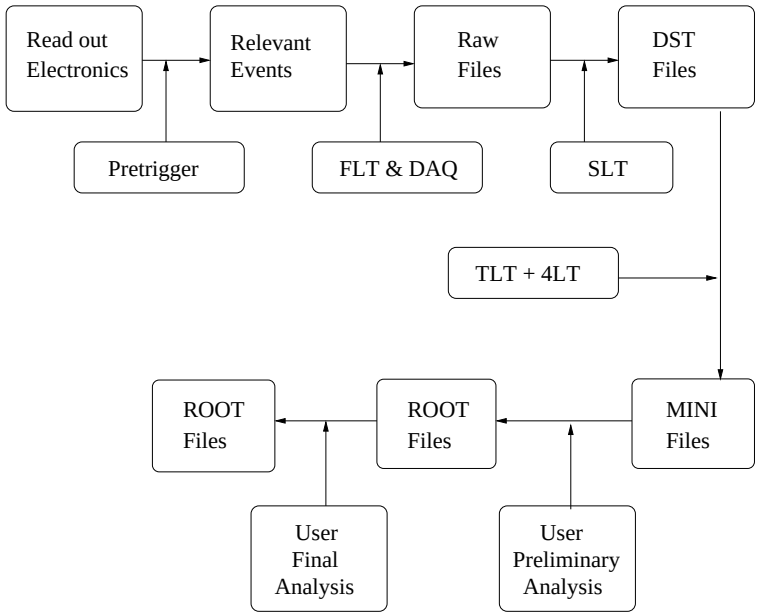

Figure 3.1 *Basic Hierarchy of Data Storage.*

The present analysis is done using only IA triggered data collected during December 2002. The total amount of data collected using J/ψ trigger equals 164×10^6 events out of which 20,000 J/ψ's were reconstructed. The total amount of minimum

bias events recorded equals 200×10^6 events. Figure 3.1 shows a simple flow chart representing the hierarchy followed for data storage and analysis.

3.2 Event Reconstruction

Event reconstruction and event classification forms the final step of the trigger system. The idea of event classification was to store the reconstructed data in table format, with each table representing a particular aspect of the events. For example, one table contains all information about geometry of the detector during an event, another contains all information about the vertex of a track, then another about the track itself. There are tables that contain data from Monte Carlo production so that it could be reconstructed the same way as the data to make a higher level of comparison between data and Monte Carlo results.

3.2.1 Analysis and Reconstruction Tool for Events

ARTE is a common roof under which offline programming and part of the online programming for HERA-B is housed [26]. In general, ARTE provides a program steering tool that facilitates input/output, dynamic memory management and interactive program control. ARTE is the central house for all the general data structures stored as header files (filename.h) for the HERA-B software.

ARTE was developed and tested under the UNIX environment. It was developed mainly using FORTRAN 77, while it had been proven to be easily and efficiently accessible in C and C++ programs as well. For this analysis, all programming for reconstruction and analysis by the user was done using C++. To initialize ARTE, the header files "arte.h" and "arte.hh" were added. Several PAW based ".kumac" files were also used to provide the links to various devices and software.

The naming convention of data structures in the ARTE tables were done to allow easy recognition. Each name contains four letters. The first letter represents the type of data. For example, 'D' stands for *digitization*, 'R' stands for *reconstructed*

(both data from experiment and Monte Carlo), 'M' stands for *Monte Carlo generated*. The next three letters represents the detector component or the nature of the structure. For example, data structure for *target* properties have 'TAR' as the three letters, for *track* properties 'TRA' were the three letters. Together, if we have 'MTRA', it stands for *Monte Carlo generated tracks* [27, 28, 29, 30].

3.2.2 Event Reconstruction Packages

The reconstruction package in ARTE is a common interface connecting all the reconstruction routines and offers several reconstruction chains. For example,it provides access to Monte Carlo and data separately. ARTE classifies the data obtained from various detectors and stores them in the table format. In ARTE, we have tables that represent one specific component of the detector, and there are also tables that have variables representing output from detector combinations such as VDS-ECAL combination or VDS-OTR combination. The combination tables help in easier reconstruction. For example, one table contains information mainly about charged particle tracks, in which case the user need not worry about the neutral particle tracks. The version of the ARTE reconstruction package used for this analysis is "ARTE-04-01-r5". This version completely ignores the ITR because the ITR's presence or absence does not show significant changes on tracking efficiency. The reconstruction routines that makes this ARTE reconstruction package are standard routines widely used in experimental high energy physics and they are as mentioned below.

- Geometry is the main thing that has to be maintained for event reconstruction, so that a track can be identified accurately. Hence alignment corrections, hits recognition, and track reconstruction should be done effectively. The geometry version used for this analysis is "GEOM/VERS 2.1205", where the first 2 stands for the year, the 12 stands for the month, and 05 represents the 5th iteration or sub-version.

- PRISM is just an event display and Tc1/Tk interface.

- CATS - Cellular Automaton of Tracking in Silicon (CATS) is the track reconstruction package for the Silicon tracker that uses a principle most widely used in neural networks. The package collects experimental hit points and sorts them into track groups. Incorrect tracks may be constructed accidentally but eventually will be rejected during further analysis without losing real tracks. Specific features of the SVD favor the segment model of a cellular automaton, where an elementary unit (a cell) is a segment connecting two hits in neighbouring layers. To cope with the high interaction rate and the poor-speed of the competing kalman filter, CATS was chosen and works efficiently.

- WAX is the software interface between the outer tracker and ARTE. It feeds information into HITB, RSEG, RHIT and to other ARTE tables.

- RISE/RITER - The ring searching routines for the RICH plays a very important role in particle identification and have proven to work efficiently. It has been a robust part of the reconstruction package. The idea behind the ring searching routines was based on drawing a ring around each photon hit and the points where many circles intersect is a ring center. Once the ring center is determined, we join all the points to reconstruct the ring and determine the radius of the ring. From the radius of the ring, we can determine the Čerenkov angle. Then using the Čerenkov angle and momentum of a track, we can separate different hadrons based on their momentum thresholds to emit Čerenkov radiation. Figure 3.2 shows a rough diagram showing the idea of ring reconstruction.

- CARE is the ECAL's reconstruction package. The main goal of the ECAL reconstruction is to detect either electromagnetic or hadronic showers in a standalone mode. The secondary goal of the ECAL reconstruction is to search for all signals coming from external charged particles impinging on ECAL using informations from other detectors. During this phase it is possible to classify signals on ECAL as − neutral particle showers (most probably gammas), charged particle showers (electrons and strongly interacting pions), and charged particle low signals (MIPS). The main job that CARE does in order to achieve these

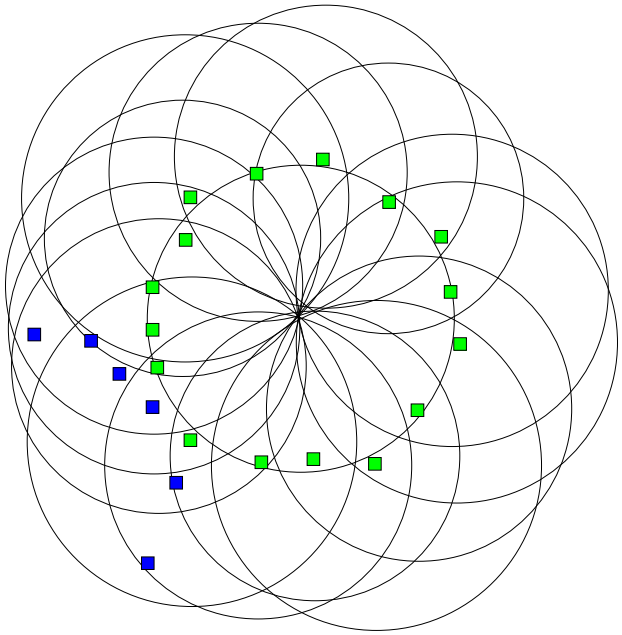

Figure 3.2 *A diagram showing the ring reconstruction method.*

goals is that it clusterizes the information on the hit cells of the calorimeter according to their measured energy. It further classifies the clusters of hit cells found. Various pattern recognition techniques are being used for this purpose.

- **MUREC** is the MUON reconstruction package. It uses two methods for reconstruction. One method uses the track information from the rest of the detector and generates a seed to muon detection. The other method finds independent track hits in the muon detector.

In general, RANGER/MARPLE was being used for the track fitting purpose, where the track hits from various detectors are linked together to reconstruct a track. The RANGER package does the track fitting in four steps − first by fitting the x coordinates, followed by the y coordinates, then project the track through the magnet, and finally behind the RICH. For vertexing, the package GROVER is being used. Most or all of these packages are written in C++. The main and notable features of the geometry version reflect the kind of systematic errors one may expect. The important features of GEOM/VERS 2.1205(also are the changes from the geometry's

previous version) are:

- The TARGET wires have the positions as given from magnet-off alignment for MAGNET OFF. With MAGNET ON all wires are shifted by 0.333 cm to positive x and by 0.036 cm to negative y for compensation of primary beam deflection due to our magnetic field;
- a new VDS in agreement with alignment data (shifts in x and y by 1-3 mm, also shifts in z). This results also in different superlayer positions. Attention: Superlayer SI01 and SI02 overlap.
- In MS14 and MS15 the stereolayers had the wrong sign, i.e. for all ± 5 degree layers the sign is reversed.
- A new muon geometry in agreement with alignment data.

The implementation of all the packages above is done by PAW's ".kumac" file. A .kumac file is a special type of shell file that acts as a macro to perform specific operations. We input the links to access raw data files and the corresponding geometry packages and alignment constants into the .kumac file. This assists reconstruction.

3.2.3 File generation sequence in event reconstruction

As shown in Figure 3.1, all the data after the trigger are stored on magnetic tapes and similar storage devices. After event reconstruction, the resultant data is stored in the form of mini-files and stored on tape. The files are accessible to the users through a cluster farm that allows users to access the data in parallel mode. Each user selects specific events of interest and dumps them into a ntuple. For this analysis, the PAW inspired "ntuple" type of storage is done using PAW's successor, the "ROOT" graphics package distributed by CERN. Later, data are accessed from the ntuples to study and determine cut parameters required to obtain the final result.

3.3 HERA-B Event Simulation

Event simulations have become the way to study the performance of particle detectors and HERA-B is no exception. Event simulations allow one to determine detector acceptance, trigger efficiencies and particle reconstruction efficiencies for particles produced in interactions and decays reconstructed from real data. Event simulations also help in estimating systematic errors and other aspects of the experiment.

The event simulations are generally based on Monte Carlo techniques. For HERA-B event simulation the software packages such as PYTHIA, GEANT4 and ARTE were used together to create HBGEAN. The HERA-B event simulations were done in 3 steps.

- The first step generates particles and physical processes for the 920 GeV/c proton beam striking on a target wire made of materials used in this experiment.
- In the second step, all the generated particles from the simulated interactions are classified into particles produced from primary and secondary interactions or decays. Everything is then stored in the ARTE tables as MIMP, MTAR, MTRA etc.
- As the last step, the generated particles are run through HBGEAN's detector simulation [31]. To get a good comparison for the reconstruction efficiency of real data, the MC simulated events are made to undergo the same offline reconstruction as the real data.

Particle generation in the event simulations is done using the combination of the PYTHIA/JETSET subroutine and the FRITIOF subroutine of the Lund Monte Carlo package. The physics behind the generation of different particles is different and for the present analysis, particles of interest are open charm mesons and ϕ mesons. PYTHIA generates the hard interaction between the beam proton and target nucleon. Only the events associated with the heavy quarks and their decay products are kept. These particles generated by PYTHIA are then used as input to FRITIOF [32].

FRITIOF simulates the proton-nucleus interactions in the fixed target mode. This event generator does so by conserving momentum and energy in every event. For this analysis, the Monte Carlo data were generated, reconstructed and stored in ARTE tables by a group at DESY [33]. This dissertation uses the available Monte Carlo data as an end-user.

3.3.1 Model for open-charmed mesons generation

The confinement of quarks in hadrons is attributed to the strong potential that increases as the separation between the quarks. When the separation becomes sufficiently large, the string between the quarks break and a new quark pair is created through the hadronization process, to lower the potential energy. The approach used in the Lund scheme reiterates that the remaining jets create additional strings if the momentum is large enough. The flavor of a new pair that may be created is determined using probabilities based on the mass ratio among the quarks ($m_u : m_d : m_s : m_c \approx 1 : 1 : 0.3 : 10^{-11}$). This strongly favors the lighter quarks over the heavier quarks. And as described in Chapter 1, heavy quark production could only be explained through perturbative QCD. Once the heavy quarks are produced, they fragment and hadronize with the help of lighter quarks and form stable particles.

In the PYTHIA generator, quark pairs are generally produced according to the "String Model". Based on the mass ratios of flavor production, it is almost certain that charmed particles cannot be produced in non-perturbative processes. Hence, perturbative processes produce $c\bar{c}$ pairs. This followed by fragmentation of the strings and non-perturbative hadronization processes are responsible for the generation of open-charmed mesons. In most cases, if not always, charm and anticharm quarks are produced in pairs and the unstable pairs start to decay. Only low momentum quark combinations remain forming color singlet pairs by tunneling through the potential barriers, thus breaking the strings. Again the meson production depends on the properties of these particle strings and their probability [34].

3.3.2 Model used for generation of ϕ mesons

According to the Lund model, the interaction between an incident hadron and the target is pictured as a connection between a valence quark of the incident hadron and a valence quark of the target. The remaining valence quarks will continue to move apart and a color flux tube is stretched between the valence quarks. Consequently one of the valence quarks of the incident hadron will be the leading quark at the end point of the string. The valence quarks of the interacting hadrons have an equal probability to be the interacting quark. Mesons are produced by the creation of pairs of quark and anti-quark, which are pulled apart by the string. For incident non-strange beams, s and $\bar{s}$-pairs must be created to produce a ϕ meson which is the case in pN interactions that we are interested in. Figure 1.4 shows the various relevant processes used in this model [34, 35]. An important point to be noted here is that the Lund cross-section for inclusive ϕ production is rather sensitive to the parameter which determines the relative creation probability of $s\bar{s}$-pairs compared to $u\bar{u}$ or $d\bar{d}$ pairs. Even though it is sensitive, the problem is solved if we set the parameter to some optimum value so that the Monte Carlo agrees with the data. This is tested by data-Monte Carlo comparison of the co-variance matrices in the ARTE tables and is well taken care of. The Lund model described above is true for low-p_T interactions, but they do not necessarily agree for high-p_T interactions. The production processes involve similar processes except, in addition, gluon-gluon interactions (LO processes) and quark-gluon interactions (NLO processes) must be included as well.

The two models described above (regarding the generation of open-charm mesons and ϕ mesons) are theoretically valid. From a practical point of view, the implementation of the above models into a program to generate these particles are done mainly by using the differential cross-sections as a function of x_F and p_T in the center-of-mass frame. This relation is described in section 1.3.1. Therefore, by fixing the values of N, b and the proportionality constant in the differential equation, particles are generated with certain boundary conditions. These particles are then run through the detector by requiring that a particle generated with certain momentum, when it passes a particular position, should obey another set of boundary conditions.

After all of these are achieved, then event reconstruction procedures are followed and finally they get stored in the ARTE tables.

3.4 Experimental determination of cross-section

When one talks about nuclear decay, one always characterizes it with the number of radioactive particles that are still present as given by the exponential decay formula. Similarly, when one talks about hadronic interactions or hadronic decay, we still want to know how many particles of a particular kind are being produced. At high energies, interactions are going to be inelastic most of the time. New final state particles will be produced. Using a detector we detect these particles. Then we reconstruct a particular final state particle and find out how many could be observed. However, the observed number is not the total number produced because of poor detection and reconstruction efficiencies. The detection and reconstruction efficiencies are measured through Monte Carlo events. The important point to be noted here is that the number observed is directly proportional to the initial intensity of particles involved in the interactions. It is also proportional to the cross-section of the particle of interest being produced within a certain cross-sectional range. The most obvious of all is, it is proportional to the detection and reconstruction efficiency. For example, consider the reaction $P \rightarrow AB$, where P itself is produced in the primary interaction of two hadrons. But P is short-lived and hence decays to AB final state. A and B are relatively longer-living and therefore they can be detected by the detector. We reconstruct P by plotting the invariant mass spectrum of AB, and determine the number of P's observed. This number of P's observed is given by,

$$N_{P\rightarrow AB} \propto \mathcal{L} \cdot \sigma_P \cdot \varepsilon_{P\rightarrow AB} \tag{3.1}$$

where $N_{P\rightarrow AB}$ represents the number of P final state particles observed, $\mathcal{L}$ stands for integrated luminosity which quantifies the total number of interactions per event per unit cross-section, the description of which is given in the next subsection. σ_P stands for the cross-section of particle P and $\varepsilon_{P\rightarrow AB}$ stands for the detection and reconstruction efficiency. Now the important thing to remember is that P's were

reconstructed using one particular decay channel. However, the particle P need not decay into that particular final state all the time. So out of 100 decays, how many times P decays into AB final state is quantified by the branching ratio for the channel. The branching ratio gives the probability of the occurence of this decay. So if we rewrite the equation above incorporating for the branching ratio, we obtain

$$N_{P\rightarrow AB} = \mathcal{L} \cdot \sigma_P \cdot \mathcal{BR}\,(P \rightarrow AB) \cdot \varepsilon_{P\rightarrow AB} \tag{3.2}$$

Experimental cross-sections are determined using the formula:

$$\sigma_P = \frac{N_{\mathrm{P\rightarrow AB}}}{\mathcal{L} \cdot \mathcal{BR}\,(P \rightarrow AB) \cdot \varepsilon_{P\rightarrow AB}} \tag{3.3}$$

This method is also called the direct method to measure cross-section.

In this dissertation, we are measuring the ϕ cross-section. We will use the direct method to measure ϕ cross-section. When we write equation 3.2 both for the number of ϕ mesons from charm decay and the number of ϕ mesons from primary interactions and divide them, we obtain the fraction of ϕ mesons from charm decay. This fraction is measured using the Δz method as described in Chapter 4. The fraction is proportional to the ratio of open-charm cross-section to the ϕ cross-section. So if we know the ϕ cross-section, we can make a relative measurement of the charm cross-section. A detailed description of this is given in Chapter 4.

3.4.1 Luminosity determination

If a beam of N particles bombards a target consisting of n_0 atomic nuclei which are concentrated in the area S, then the number of inelastic events is given by:

$$n_{inel} = \sigma_{inel} \cdot (\frac{n_0 N}{S}) \tag{3.4}$$

where σ_{inel} is the cross-section of inelastic processes and the expression in the parentheses is the luminosity $\mathcal{L}$ and hence the definition for luminosity is

$$\mathcal{L} = \frac{n_0 N}{S} \tag{3.5}$$

In the HERA-B experiment, where the stored proton beam is only partly interacting with the target, we know neither the number of protons that interact nor the number of interacting target nuclei, since we do not know about the target area inserted in the beam. From the equation above, we may write

$$n_{inel} = \sigma_{inel} \cdot \mathcal{L} \tag{3.6}$$

which means we can determine the luminosity by knowing the inelastic cross-section and the number of inelastic interactions.

Table 3.1 *Inelastic cross-sections for different target materials for 920 GeV/c pN interactions.*

Target	σ_{inel}**, mb**
Carbon	237.2 ± 3.4
Titanium	644.8 ± 7.5
Tungsten	1710.0 ± 16.6

Determining inelastic cross-sections directly for every experiment is not possible. The inelastic cross-sections for different targets used in this analysis are given in Table 3.1. These inelastic cross-sections are the result of extrapolation of results obtained from theory and experiment. There were experiments that studied inelastic cross-sections of proton-nuclei collisions as a function of center-of-mass energy, for several target materials. This leaves us with the task of determining the number of inelastic events and we do this for the"*IA*" triggered events taped for each run. We take all the *IA* triggered events and try to extract out the inelastic events. For the ideal case, all *IA* triggered events are inelastic events. But the presence of empty events causes some complication [36].

Suppose the probability of k interactions per one bunch crossing follows a Poisson distribution:

$$P(k) = \frac{\lambda^k}{k!} e^{-\lambda}, \tag{3.7}$$

where λ is the average number of inelastic interactions per bunch crossing. To exclude the empty events, we assume that $k > 0$ always. When k=0, then $P(k) = e^{-\lambda}$. The

sum of all probabilities equals 1 and hence the probability for $k \neq 0$ is just $1 - e^{-\lambda}$. From this, we obtain the number of inelastic events to be

$$n_{inel} = \lambda \frac{n_{\mathrm{IA_{trig}}}}{1 - e^{-\lambda}}. \tag{3.8}$$

So the task now reduces to determining λ. There were hodoscopes placed behind the RICH to determine the interaction rate and we can determine the value of λ from,

$$\lambda = K \frac{R_{\mathrm{hod}}[\mathrm{MHz}]}{8.523[\mathrm{MHz}]}, \tag{3.9}$$

where the 8.523 MHz is the frequency with which the beam particles are passing through the target per bunch crossing and K is the factor which when multiplied with the hodoscope rate gives the actual interaction rate. The K factors are determined by adjusting the hodoscope rates to give approximately equal probability distributions for the number of vertices per event, considering the acceptance, versus the different runs of a particular target. The K factors for different targets are as shown in the Table 3.2. For this analysis, we have used only the *IA* triggered events. But considering the possibility of wrongly triggered events, that might allow a small

Table 3.2 *Hodoscopes rate correction factor for different target materials.*

Target	**K**
Carbon	1.748 ± 0.030
Titanium	1.412 ± 0.034
Tungsten	1.172 ± 0.044

fraction (ν) of empty events to leak into the of number of *IA* events and also considering the trigger efficiency (ϵ), the correct formula for the number of inelastic events would be

$$n_{inel} = n_{IA_{trig}} \cdot \lambda \frac{1}{1 - e^{-\lambda}\nu - \lambda e^{-\lambda}(1 - \epsilon)}, \tag{3.10}$$

where ν and ϵ are determined from Monte Carlo studies.

The luminosity determination method above is just an overview. This method was used by the target group at DESY to determine the luminosities of all the interaction triggered runs with different target materials used in the HERA-B

experiment. The integrated luminosities for this analysis are determined by summing the luminosities of all the runs with respect to each target material.

3.5 Error Analysis Methods

Experimental errors in general are classified into statistical and systematic errors. Statistical errors represent how well a result can be reproduced given the condition that the experiment is repeated N number of times. On the other hand, systematic errors represent human errors, resolution of the detector, errors from Monte Carlo simulations, systematic errors of quantities determined from a different experiment but used as input to calculate the result. Not all systematic errors are accountable since there is no systematic control on those errors, they are inevitable. To deal with these inevitable errors, systematic errors are only estimated to an upper limit at best. Errors may be calculated using many different techniques. The method followed in this analysis is described below.

3.5.1 Statistical Errors

Statistical error originate from the distribution of a data sample. It varies with the amount of data that fills the distribution. It has been a general practice to quote the statistical errors from event simulations as systematic errors because of their theoretical nature of reproduction of events. How correct is this practice is a question of debate. Practically speaking, why beat ourselves because we lack in statistics in our simulation studies and end up quoting a large systematic error. However, the argument that the statistics from Monte Carlo events have nothing to do with the actual statistical part of the data and hence must be under the systematic error presents a strong case. Also interesting to note is that these statistical errors from Monte Carlo simulations inherently contain information about how the result deviates from normal. However, these deviations are systematic in nature. Therefore, in the present analysis, errors from data statistics shall be classified as statistical errors and the errors from event simulations plus systematic errors from data reconstruction will

together be classified as systematic errors.

Methods to determine statistical errors are well developed. A few of these important algorithms used for this analysis are described below. The uncertainity in the statistical measurement of a physical quantity is usually estimated by evaluating the standard deviation of the measurements. The expression used to determine the standard deviation is given in equation 3.11.

$$\sigma = \sqrt{\frac{\sum_{\mathrm{i}} (x_{\mathrm{i}} - \bar{x})^2}{N-1}} \tag{3.11}$$

where $\bar{x}$ stands for the mean value of x and N represents the number of data points. When it comes to estimating errors in a *calculation* of another physical quantity using the results from the measurement of certain physical quantities, we have to follow the procedure of error propagation. Error propagation is the method of combining the errors of each of the variables used in calculating a particular quantity.

Error propagation is explained in terms of partial differentials. For instance, if we have a quantity $Z = F(A, B)$ for any function F, a slight deviation in A will result in a deviation in Z by an amount, $\left(\frac{\partial \mathrm{F}}{\partial \mathrm{A}}\right) \Delta A$, with no effect from B. Hence if we have deviations in both A and B, then deviations are combined using the Pythogorean theorem which results in the deviation in Z equal to,

$$\Delta Z = \sqrt{\left(\frac{\partial F}{\partial A}\right)^2 (\Delta A)^2 + \left(\frac{\partial F}{\partial B}\right)^2 (\Delta B)^2}. \tag{3.12}$$

In the case of $Z = A + B$,

$$\Delta Z = \sqrt{(\Delta A)^2 + (\Delta B)^2} \tag{3.13}$$

but when $Z = AB$,

$$\frac{\Delta \mathrm{Z}}{\mathrm{Z}} = \sqrt{\left(\frac{\Delta A}{A}\right)^2 + \left(\frac{\Delta B}{B}\right)^2} \tag{3.14}$$

as though one has taken logarithms on both sides of the equation and then performed the partial differentiation. The cases above are true when A and B are independent of each other.

3.5.2 Systematic Errors

In the initial stages of particle physics using bubble chambers and other small detectors, very few events would be produced, so that the statistical error at the 10% level was considered big enough to overwhelm any error quoted for the systematic error. But, at the present stage, experiments deal with thousands and millions of events, HERA-B is no exception; therefore, the statistical errors are at a few percent level which makes the systematic errors very important. Estimation of systematic error is difficult in most experiments. But, with the use of event simulation techniques and comparison with real data, the evaluation seems possible and the estimates are as good as one can do.

Evaluation of systematic error is done by consistency checks. Calibration constants and parameters contributing to the final result are weighted appropriately and the resultant variation folds in as the systematic error. Variation observed by variation in application of cut requirements should be taken into account as a systematic error. For the cross-section measurement, cut variations do affect efficiency and background significantly, but these big changes in efficiency and background seem to cause a very tiny change in the cross-section measurement. This behavior is expected because the production of ϕ's do not depend on what cuts we apply.

One important note worth mentioning is that the systematic errors are also obtained through error propagation using partial differentials, because the quantities for which we are estimating the errors are not measured directly. But unlike the statistical case where errors always add, the deviations are carefully accounted for according to direction in estimating the systematic errors. Therefore, systematic errors may be quoted with different positive and negative errors.

CHAPTER 4

DATA ANALYSIS AND RESULTS

Data analysis in modern high energy physics experiments involves computational work to process a large amount of data to extract user-specific events for further study. As far as the computation is concerned, the analysis procedures are common to all studies. The interpretation of the results is where the physics stands out. Physical quantities like cross-sections, polarization, and magnetic moments are measured from experiments to explain certain properties of a particle's behavior. In an experiment like HERA-B, which used a di-lepton trigger to record J/ψ events in parallel with a minimum bias trigger to record inelastic interactions for detector performance monitoring, the effective reconstruction efficiency of open charm hadrons is low. The total numbers of $D^{\pm}$, D^0 and $\bar{D}^0$ mesons reconstructed were ≈ 150 each. The $D_s^{\pm}$ meson yield is even smaller. Therefore, it is difficult to reconstruct a large sample of D_s mesons separately and measure its production cross-section using the exclusive decay $D_s \rightarrow \phi\pi$. In this chapter, we describe the measurement of the ϕ production cross-section using the direct method. The inclusive open-charm cross-section is then measured with the same ϕ sample using an indirect method. The indirect method has two parts to it. The first part involves the Δz method which is used to determine the fraction of ϕ's produced from open-charm decay. The second part uses this fraction and the ϕ cross-section to determine the inclusive open charm cross-section. The direct method to determine the ϕ cross-section is described in section 3.4. In section 4.1, the Δz method is described. The steps to measure the inclusive charm production using the fraction from the Δz method and the ϕ cross-section are described in section 4.1.3. The analysis and the results are described in the following sections.

4.1 The Δz Method

The MAC and the MARK II experiments had both used a statistical method to measure the b lifetime using muons from B meson decay [37, 38]. In this method, they used the impact parameter distribution of the muons to observe a shift in the peak of the distribution from zero. The positive shift is interpreted as a finite lifetime for the B meson, whereas muons from short lifetime particles do not contribute a shift in the impact parameter distribution. The shift observed in the data sample includes all long lived particles. With respect to the detector acceptance and other kinematic considerations, the main contributions were determined to be from bottom decays, charm decays, and background. In order to find the fraction of bottom decays, they simulated using Monte Carlo the fraction of charm and background that would contribute to the shift which were subtracted from the shift of the data sample. Though there were no vertex detectors and hence no precisely reconstructed primary vertex to compare with, the method proved successful in separating statistically muons produced from b decays. The lifetime of the bottom mesons are three times larger than their charm counterparts and hence they were able to separate them effectively. In our case the separation is done through ϕ mesons for charm decays from those produced in the primary interactions. Unlike the previous experiments, HERA-B had the advantage of a state-of-the-art vertex detector. Hence, primary interaction vertices are reconstructed with high accuracy. By reconstructing the secondary vertices of the ϕ mesons, flight distances can be measured. This is a more precise measurement when the separation of primary vertex and the secondary vertices are done on an event-by-event basis compared to measuring flight distances from a fixed target position which only gives a crude estimate for the position of the primary vertex.

4.1.1 What is Δz?

Many particles do not exist naturally but are produced in interactions. Most of these particles decay immediately after they are produced while some live relatively longer but decay eventually. For example, the $\phi(1020)$ decays almost immediately because

their lifetime is short. These particles are identified as resonances and their masses have well-defined widths. From the width, the lifetime of a particle can be calculated by h/Γ, where h is Planck's constant and Γ is the width. From the observed width, the ϕ has a lifetime of about 10^{-22} s. This allows the ϕ to travel a distance of $c\tau\gamma$, also known as the flight distance, before it decays, where τ represents the lifetime and γ is the Lorentz boost. The interaction takes place at one point, but the ϕ's decay at another point. The former is called the primary vertex or the primary interaction point. The point of decay of the ϕ is called the secondary vertex or the secondary interaction point. The distance between these two points along the z direction is

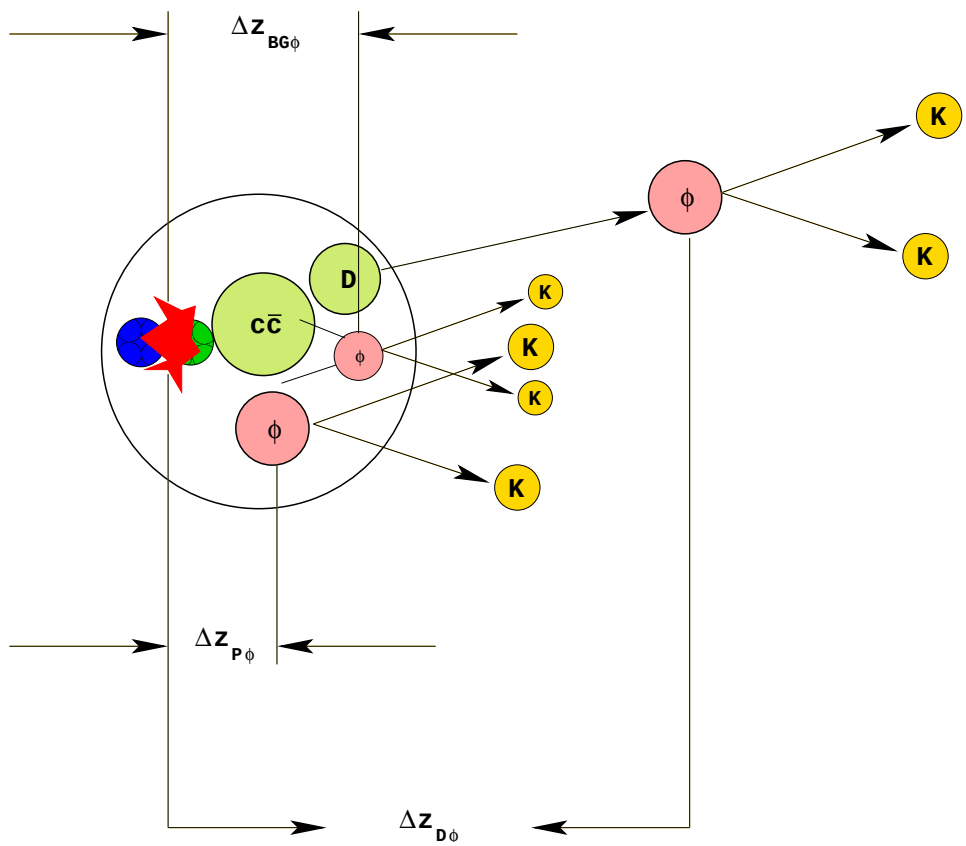

Figure 4.1 *A typical interaction diagram showing the various Δz contributions.*

referred to as the Δz. This is shown in Figure 4.1. From the short lifetime of the ϕ's, the Δz for ϕ's produced in primary interactions amounts to about 10^{-12} m. This suggests that the ϕ's will decay outside the nucleus, but not necessarily outside the

target wire. But, ϕ's from open charm decay will have a Δz of ≈ 4 mm, and hence they will be clearly separated from the primary interaction point.

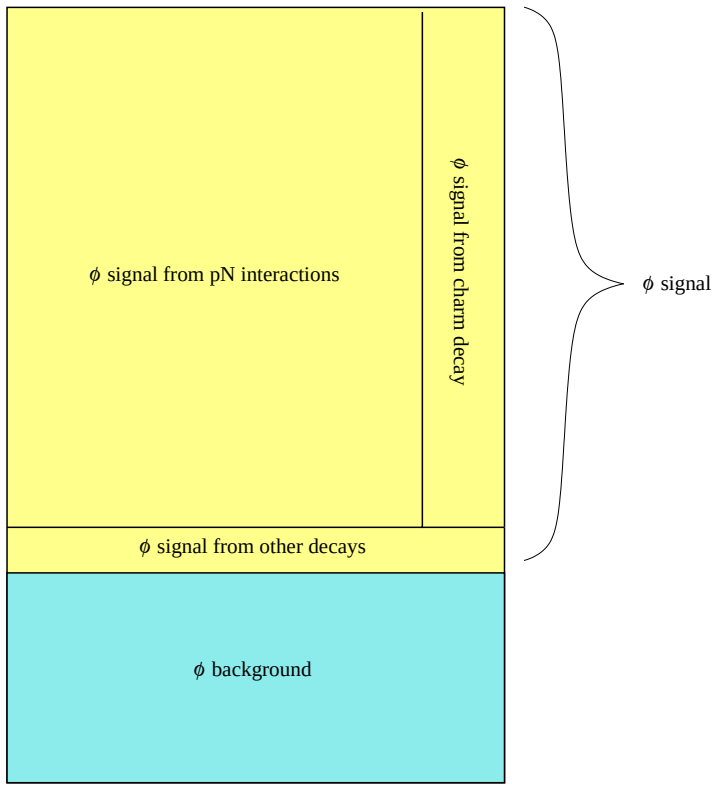

Figure 4.2 *Venn diagram representation of fractional ϕ distribution.*

4.1.2 Method description

The main sources for ϕ production are listed below.

- **pN interactions** are the interactions that take place between the projectile protons and the target nucleons. Owing to the small $c\tau_\phi\gamma$ for the $\phi(1020)$, the ϕ's decay outside the nucleus, but not necessarily outside of the target material. The resolution of the vertex reconstruction along the z direction for the HERA-B detector is ≈ 700 μm which is slightly greater than the thickness of the target. With such a vertex resolution along the z direction, the average

Δz for the ϕ's from pN interactions is expected to be approximately zero.

- ***D* decays** provide a minimum $c\tau\gamma > 2$ mm, and hence most of their decay vertices are far from the target wire. This separation is expected to be clearly visible and not be affected by the vertex resolution of the detector along the z direction.

- **Other decays** like the decays from particles containing b quarks, baryonic decays and decays from light flavor mesons with masses heavier than the ϕ's might also contribute. But the sum of their decay fractions to a ϕ is very small. Hence, their contribution can be neglected in the measurement.

- **Background** contribution can be measured from the sidebands in the $\phi \rightarrow K^+K^-$ sample. We can also look at the same-sign kaon-pair spectra in the region of the ϕ mass. In our case the sidebands near the ϕ signal provide a better estimate of the background than by using the same-sign kaons. Therefore, the average Δz from the immediate sidebands of the ϕ peak is used as the background estimate in this analysis.

Figure 4.1 shows the various Δz's which contribute. Each interaction or decay contribution is taken into account for the observed Δz of the entire data sample. Figure 4.2 is a Venn diagram showing estimated fractional contributions of each source with respect to the total sample. Taking all the sources into consideration, the total displacement of the ϕ mesons $\Delta z_{T\phi}$ can be written as

$$\Delta z_{T\phi} = f_{D\phi}\Delta z_{D\phi} + f_{P\phi}\Delta z_{P\phi} + f_{BG\phi}\Delta z_{BG\phi} \tag{4.1}$$

where $f_{i\phi}$ represent the fraction of each source. The contribution from other decays has been ignored. From equation 4.1, we can find the fraction of the charm ϕ's, which will be used to measure the charm cross-section.

4.1.3 Method to measure the *open-charm* cross-section

We can write the number of reconstructed ϕ mesons in terms of the integrated luminosity $\mathcal{L}$ and the cross-section as follows:

$$N_\phi = \mathcal{L}\sigma_\phi \mathcal{BR}(\phi \to K^+K^-)\varepsilon_\phi \tag{4.2}$$

$$N_{D\phi} = \mathcal{L}\sigma_D \mathcal{BR}(D \to \phi)\mathcal{BR}(\phi \to K^+K^-)\varepsilon_{D\phi} \tag{4.3}$$

where the equation with only a ϕ subscript is for the ϕ's detected via $\phi \to K^+K^-$, while the equation with a $D\phi$ subscript is for charmed ϕ's detected via $D(\bar{D}) \to \phi \to K^+K^-$. ε is the detection efficiency. Dividing Equation 4.3 by Equation 4.2, we obtain

$$\frac{N_{D\phi}}{N_\phi} = \frac{\mathcal{L}\sigma_D \mathcal{BR}(D \to \phi)\mathcal{BR}(\phi \to K^+K^-)\varepsilon_{D\phi}}{\mathcal{L}\sigma_\phi \mathcal{BR}(\phi \to K^+K^-)\varepsilon_\phi} = \frac{\sigma_D \mathcal{BR}(D \to \phi)\varepsilon_{D\phi}}{\sigma_\phi \varepsilon_\phi} \tag{4.4}$$

because the integrated luminosities are the same. The ratio $\frac{N_{D\phi}}{N_\phi}$ is the fraction of ϕ mesons from charm decay compared to the total number of ϕ's excluding background, measured by the Δz method. When we rewrite the equation above to include all the D mesons, we obtain

$$\sum_i \mathcal{BR}(D_i \to \phi)\sigma_{D_i} = \frac{f \cdot \sigma_\phi}{\eta} \tag{4.5}$$

where i is an integer representing the three different D mesons, and

$$f = \frac{N_{D\phi}}{N_\phi} = \frac{f_{D\phi}}{f_{P\phi} + f_{D\phi}} \qquad and \qquad \eta = \frac{\varepsilon_{D\phi}}{\varepsilon_\phi}$$

Equation 4.5 is used to calculate the inclusive charm cross-section.

4.1.4 $A-$Dependence correction

The HERA-B experiment was a fixed target experiment with protons interacting with different target nuclei. Assuming a simple model that the nucleus is spherical and all the nucleons are also spherical, the radius of the nucleus is equal to $A^{1/3}$ times the radius of a single nucleon. This means that the geometrical cross-section of the nucleus is given by,

$$\sigma = \pi R_N^2 \approx (30\ mb) \cdot A^{2/3} \tag{4.6}$$

where R_N is the radius of the nucleus and the nucleon radius is around 1 fm. The simple argument that the inelastic interaction cross-section is equal to the geometrical cross-section of the nucleus agrees with the observed $A-$dependence of inelastic cross-sections in the energy range 60-375 GeV/c:

$$\sigma \approx (40\ mb) \cdot A^{0.71} \tag{4.7}$$

In other words, the projectile proton interacts more likely with the nucleons on the surface of the nucleus than those near the center or the farther end of the nucleus. This is called shadowing. The same model suggests that for new particles produced with smaller cross-section, there is less shadowing. This dependence is written in the following form:

$$\sigma = \sigma_0 A^{\alpha} \tag{4.8}$$

where σ_0 is called the cross-section coefficient. The cross-section coefficient is the cross-section of a particle if there were only one projectile proton and one target nucleon involved in the interaction. The cross-section of heavy particle production is expected to scale as A^{α}, with $\alpha \approx 1$, rather than $A^{0.71}$. The ϕ cross-section is smaller than the inelastic cross-section but not as small as the charm cross-section. Therefore, the α value for the ϕ production is expected to lie in between the inelastic and the open charm α values. The α for the ϕ production has been measured to be $\alpha_{\phi} = 0.86 \pm 0.02$ [39, 40]. The α value for charm production has been measured to be $\alpha_c = 1.02 \pm 0.03 \pm 0.02$ [41]. The α for ϕ will be measured in the present analysis from the total cross-sections of ϕ production for different target materials.

Incorporating the $A-$dependence into the cross-section formula 3.3, we obtain

$$\sigma_{0\phi} = \frac{N_{\phi}}{\mathcal{BR}(\phi \to K^+K^-)A^{\alpha}\mathcal{L}\varepsilon_{\phi}} \tag{4.9}$$

When all the target data are included together to determine an overall value for the cross-section coefficient, the target material dependent quantities like the integrated luminosity ($\mathcal{L}$) and the efficiency (ε) are entered into a summation. Equation 4.9 becomes

$$\sigma_{0\phi} = \frac{N_{\phi}}{\mathcal{BR}(\phi \to K^+K^-)\sum_{\mathrm{i}} A_{\mathrm{i}}^{\alpha}\mathcal{L}_{\mathrm{i}}\varepsilon_{\mathrm{i}\phi}} \tag{4.10}$$

4.2 ϕ Analysis

The inclusive ϕ cross-section is measured using the direct method described in the previous chapter in section 3.4. The first step is to determine the selection criteria. Once the selection criteria are determined, reconstruction and counting the number of ϕ's form the next step. Cross-section will be calculated by using equation 3.3.

4.2.1 Data sample

The data for the present analysis were collected during the December 2002 runs. Three different target materials were used for this period of runs. They were: Carbon(C), Titanium(Ti), and Tungsten(W). After initial data reconstruction, all the files were stored as "mini" files on tape. These *mini* files can be read out by using standard HERA-B software. The HERA-B software modules include, usinit.C, usevnt.C, usstop.C, and a number of user header files, all built on the ARTE architecture. The file usinit.C is used to initialize all the variables and routines to be used in the readout. The usevnt.C uses the routines to select tracks of interest (ToI) and also reads out the desired information about the selected tracks. These tracks are then written out to a ROOT histogram file. The usevnt.C is the main program where all the operations like selection, evaluation and storage are done. The usstop.C is to write out everything and close the ROOT files appropriately.

4.2.2 Selection criteria

Selection Criteria (Cuts) form the main crux of the data analysis. Cuts are generally classified under two categories based on *event quality* and *track quality* [42]. Event quality cuts on event parameters include:

- Existence of an event header. If no relevant event header exists, the event gets rejected.
- Existence of a run number for the event. If no run number is stored for the

event or it is ambiguous, the event gets rejected.

- Existence of information on how many tracks and vertices got reconstructed in the event. If an event that has tracks but no vertices or vice versa, it is considered to be a bad event and is rejected.

- Events with interaction (IA) trigger. As part of event selection, we have selected only the events with IA trigger.

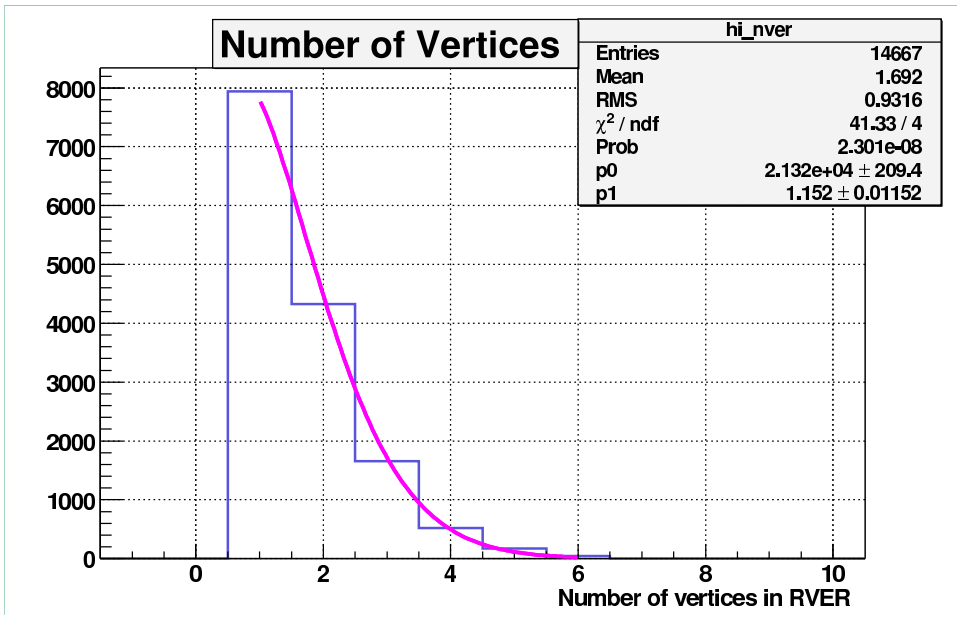

Figure 4.3 *Distribution of number of interactions per event.*

Some of the other event quality cuts that are applied in this analysis include, table of reconstructed vertices (RVER), table of reconstructed tracks (RTRA), and table of reconstructed target (GTAR), which must all exist. Also, in selecting vertices, only one primary vertex that has the maximum number of tracks in an event is chosen. Not all primary vertices of an event are being read out. The number of primary vertices per event ranges between 1 and 6, as shown in Figure 4.3.

Many track quality cuts are applied. They are listed in two parts below. The first part of the track quality cuts is based on the reconstruction parameters of the

tracks which are in turn mainly based on the number of hits on the track. They are:

- Vertex cut based on the number of hits on the SVD. The seed and triggers require that there be a certain number of hits on the various superlayers of the SVD. As can be seen from Figure 4.4a, the range of hits on the SVD has a spread between 3 and 20.

- Tracking cut based on the number of hits on the superlayers of the OTR. Figure 4.4b shows the range of number of hits on the OTR which spreads between 5 and 50.

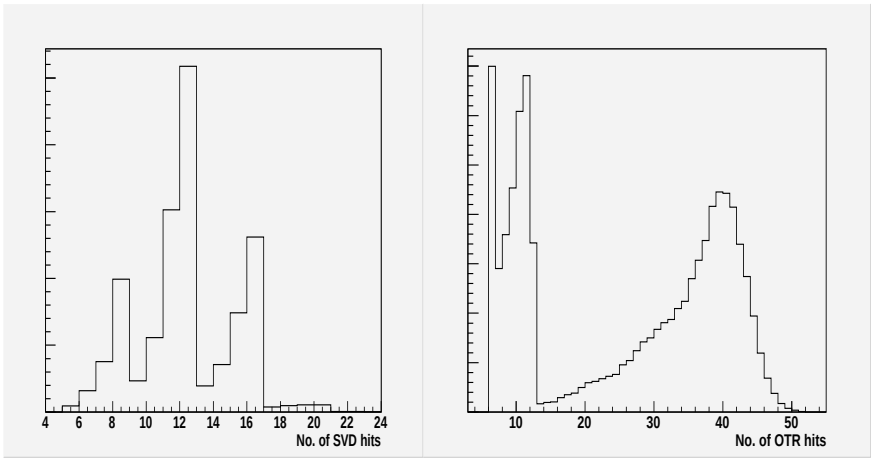

(a) **(b)**

Figure 4.4 *Hit distributions of (a) SVD (b) OTR.*

- RICH cut based on the occupancy rate in the RICH detector. The number of hits are chosen such that there are not too many hits, making the ring reconstruction difficult. The range of hits is between 40 and 3500, as can be seen in Figure 4.5.

The second part of the track quality cuts include those that identify kaons coming from a ϕ. They are:

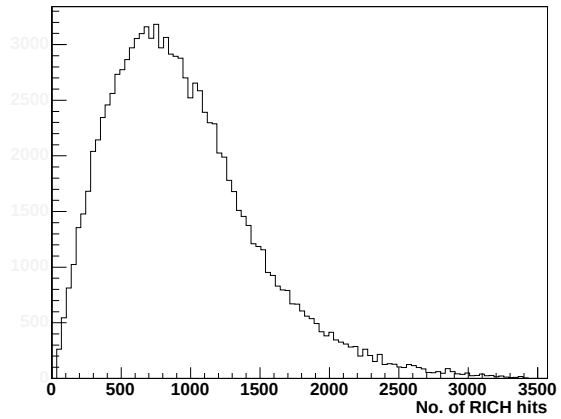

Figure 4.5 *Hit distributions of the RICH detector*.

- Particle ID cuts applied to identify kaons. Particle identification (PID) is done using the likelihood probability of a track being a particular particle type. The probability is computed from the momentum and the ring radius with the information obtained from the RICH detector.

  Figure 4.6 shows the RICH particle identification efficiency plots for various kaon likelihood cuts as a function of the momentum of the track. The kaon momentum threshold for the HERA-B RICH is 9.6 GeV/c. Just selecting all particles of momentum above the kaon threshold in ϕ selection is not enough to reduce background adequately. On the other hand, a tighter particle ID cut on both kaons helps in reducing background significantly. Figure 4.7 shows the effect of particle ID requirement on ϕ selection. The top-left plot shows the KK invariant mass spectrum with no requirement of PID on the tracks and we do not observe a ϕ signal. The bottom-left plot shows the ϕ signal after requiring a 60% kaon likelihood for one of the tracks. The bottom-right plot shows the reduction of background, if in addition to the 60% likelihood on one track we require both tracks have momentum above kaon threshold. The top-right plot shows the significant reduction of background after requiring both tracks have kaon likelihood above 60%.

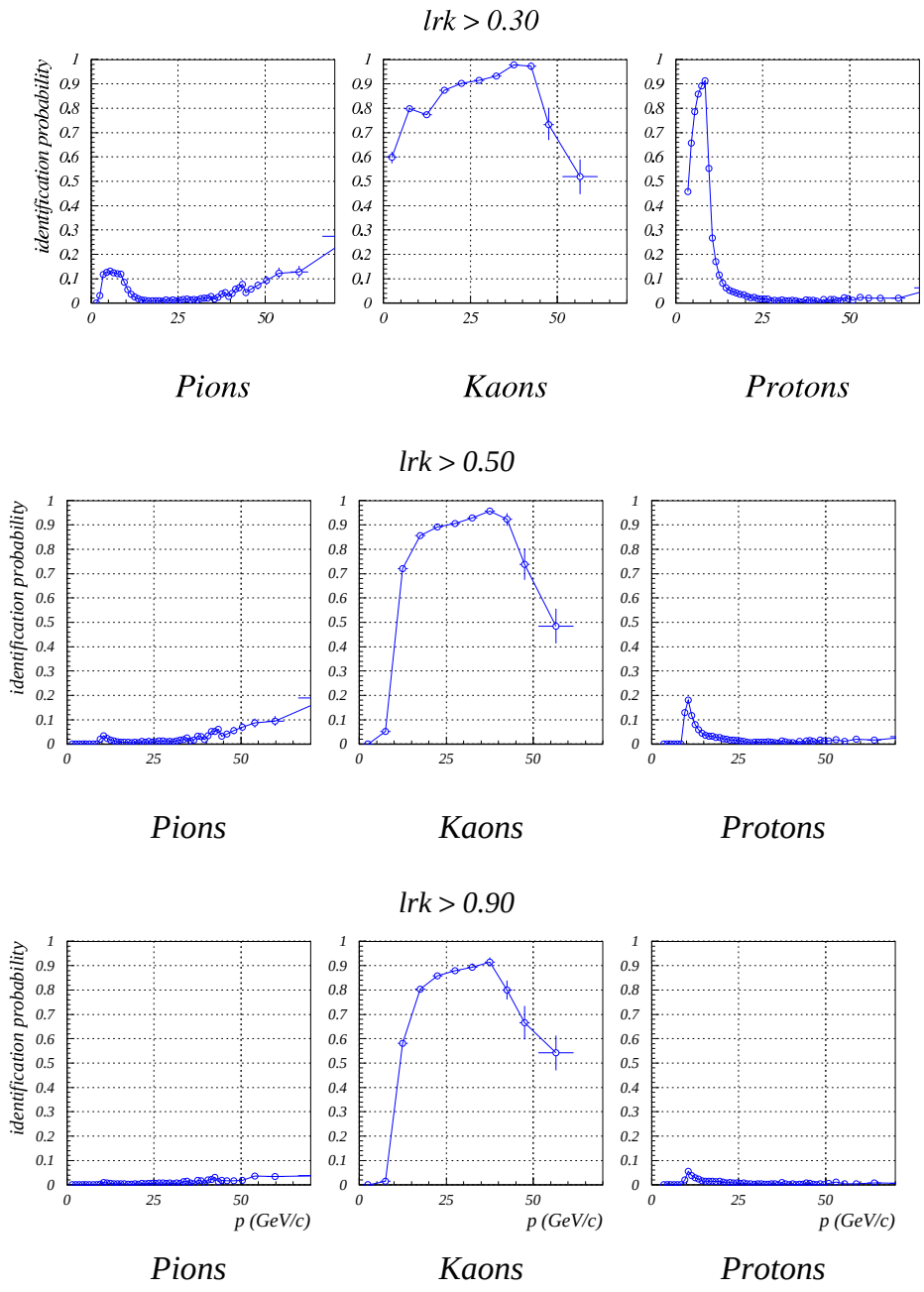

Figure 4.6 *Particle likelihood efficiency plots.*

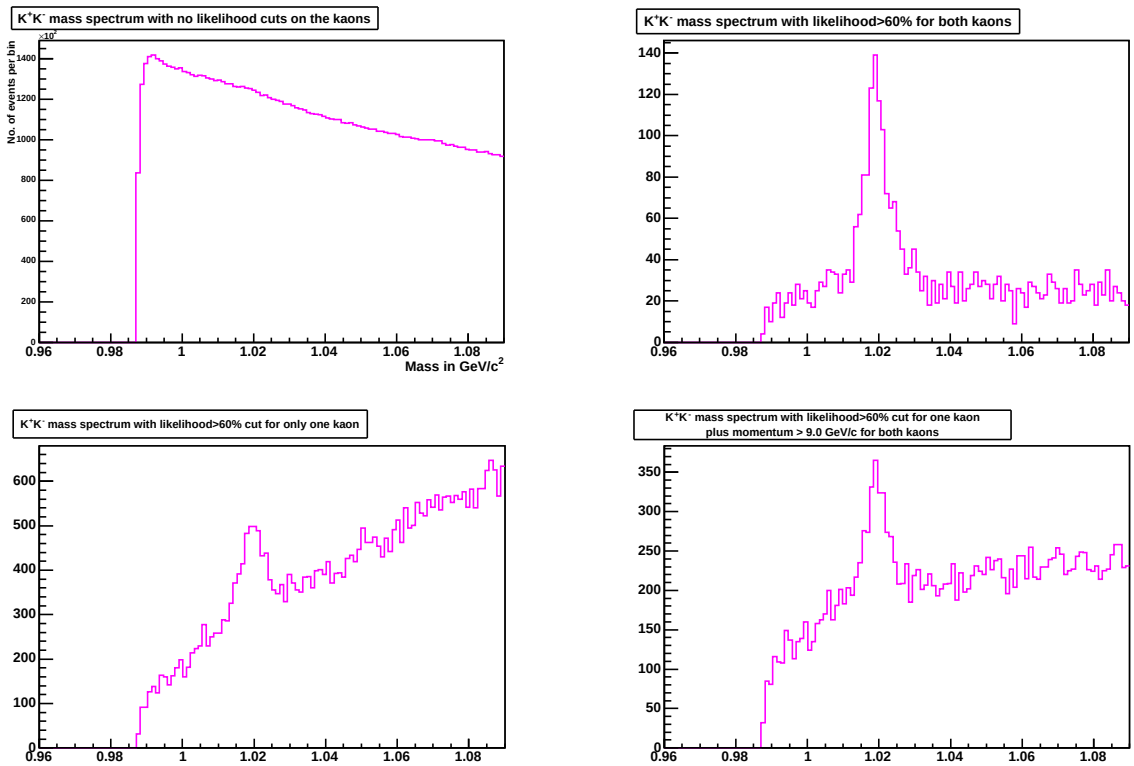

Figure 4.7 *Effect of kaon likelihood on ϕ selection.*

- Oppositely charged kaons.
- Opening angle cut. Figure 4.8 shows the opening angle distribution of all the kaon pairs, which ranges from 0 to 60 mrad. But the interesting fact to be observed here is that all the kaon pairs under the ϕ peak shown in the lower plot have opening angles between 10 and 30 mrad. An opening angle cut of more than 1 mrad was applied to remove clones (tracks sharing most of the hits) in track reconstruction.

The choice of the cuts is made in such a way that the loss of good events are kept to a minimum level. The effect of the cuts quantified as survival rates are listed in Tables 4.1 and 4.2.

Table 4.1 *Table for step-by-step reconstruction efficiency measurement* w.r.t *events*.

Selection Criteria for Event Quality

Selection criterion	**Estimated survival rate in %**
Existence of EVHD table	100%
Existence of RTRA table	95%
Existence of RVER table	95%
Existence of GTAR table	95%
Events with IA trigger alone	90%

Table 4.2 *Table for step-by-step reconstruction efficiency measurement* w.r.t *tracks*.

Selection Criteria for Track Quality

General Selection Criterion for Tracks

Selection Criteria	**Estimated survival rate in %**
Number of hits on SVD > 6	70%
Number of hits on OTR > 15	70%
Number of hits on RICH $> 40 < 3000$	90%

Selection Criterion for Tracks to reconstruct $\phi(1020)$

Selection Criteria	**Estimated survival rate in %**
Likelihood probability of $K_1 > 0.60$	30%
Likelihood probability of $K_2 > 0.60$	30%
No neutral tracks, RTRA $!= 6$	100%
Kaons of pairs be oppositely charged	30%
Opening angle of pair > 1 mrad	80%

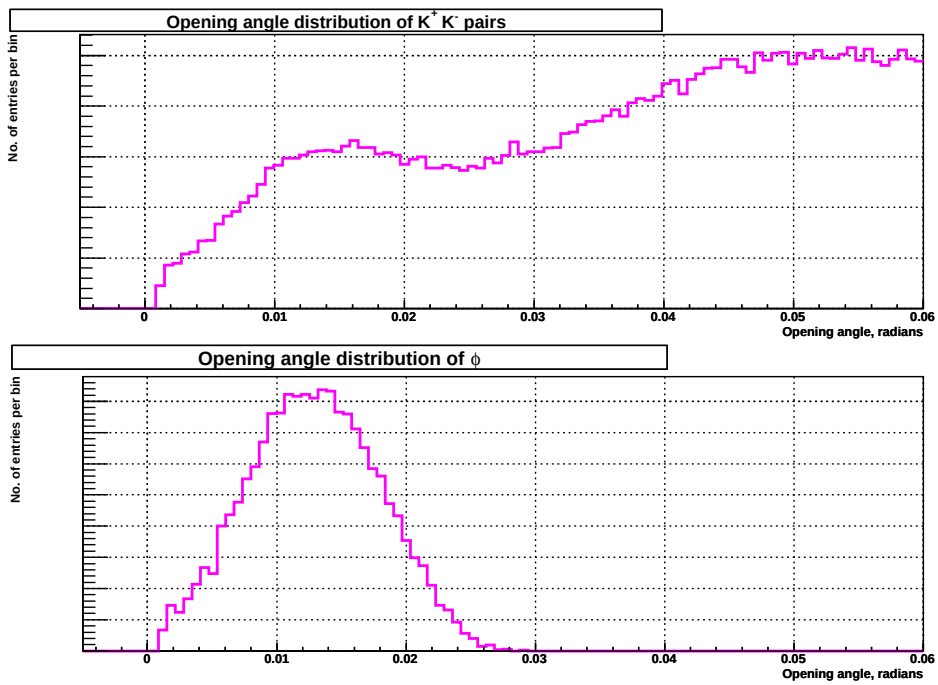

Figure 4.8 *Opening angle distribution of KK vs ϕ.*

4.2.3 ϕ Counting and Mass measurement

After running the entire data through the selection criteria, we are left with a sample of events enriched in ϕ. The next step is the reconstruction and counting of the ϕ's. The two kaon tracks are required to form a vertex (an intersection point). For each oppositely charged kaon-pair, we calculate the invariant mass of the pair using the following equation:

$$M = \sqrt{m_{K^+}^2 + m_{K^-}^2 + 2E_{K^+}E_{K^-} - 2\vec{p}_{K^+} \cdot \vec{p}_{K^-}} \tag{4.11}$$

where m_K represents the mass of the kaons, E_K represents the energy of the kaon tracks, and $\vec{p_K}$ represents the 3-momenta of the kaon tracks. The invariant mass distribution is shown in Figure 4.9. A clear ϕ meson signal is visible. The invariant mass spectrum of the K^+K^- pairs is fitted by a function consisting of a background term and a relativistic Breit-Wigner (BW) resonant term convoluted with a Gaussian

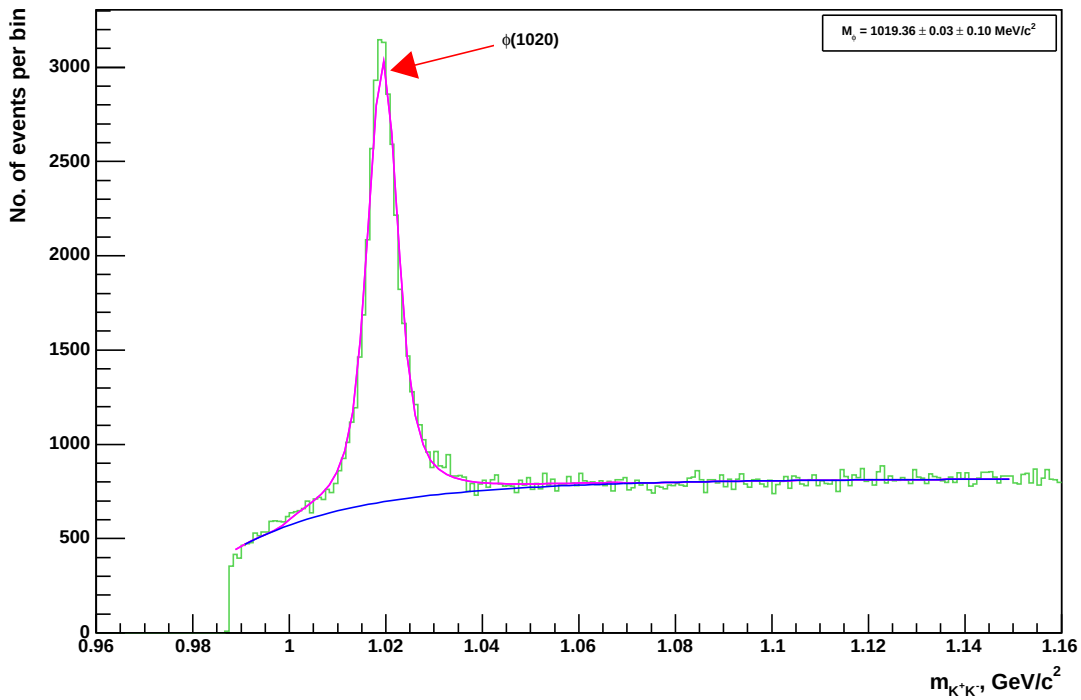

Figure 4.9 *Invariant mass spectrum of* K^+K^-.

"experimental" mass resolution function. The background function is given by

$$BG(x) = Bx^{\beta}(2-x)^{\delta} \tag{4.12}$$

where B, β and δ are constants determined by the fit. The signal is given by

$$BW_c(M, M_0, \Gamma_0) = \int BW(M', M_0, \Gamma_0) \exp\left[-\frac{1}{2}\left(\frac{M-M'}{\sigma}\right)^2\right] \frac{dM'}{\sigma\sqrt{2\pi}} \tag{4.13}$$

where

$$BW(M', M_0, \Gamma_0) = \frac{M_0\Gamma_0(M)}{\pi} \frac{2M}{(M^2-M_0^2)^2 + M_0^2\Gamma_0^2(M)}. \tag{4.14}$$

and M_0 is the central value of the ϕ mass, Γ_0 is the intrinsic width of the ϕ. σ is the standard deviation of the mass resolution assumed to be a gaussian. The fitting provides us with the mass measurement for the ϕ. The value obtained is $M_0 = 1019.41 \pm 0.038$ MeV/c^2 with a width of $\Gamma_0 = 4.5 \pm 0.10 MeV/c^2$. The values are

very close to the particle data book (PDB) values of $M_\phi = 1019.456 \pm 0.020$ MeV/c^2 with a width of $\Gamma = 4.26 \pm 0.05$ MeV/c^2. The value of σ from the fit is $\sigma = 1.7 \pm 0.3$ MeV/c^2. Using the fitting function, the number of background subtracted ϕ mesons is calculated by the integral of the curve. The limits of integration correspond to $M_\phi \ \pm 13$ MeV/c^2 which is $\approx \pm 3\Gamma$, where Γ is the full-width at half maximum (FWHM). The choice on the limits of integration was made to include a little tail of the resonance, but avoid too much background subtraction.

Table 4.3 *Table for ϕ counting.*

Target material	N_T	$N_{\phi(DATA_{RECO})}$	$N_{\phi(BG)}$	$\mathcal{L}$, **mb**$^{-1}$
Carbon	68 M	18136±137±150	16140±127±100	277732.2±55.54±3043.69
Titanium	21 M	7926±90±100	7536±87±100	33735.5±10.12±494.48
Tungsten	60 M	25091±158±200	24370±156±150	32155.4±8.04± 263.76

Table 4.3 lists the total number of events (N_T) used for the ϕ analysis, the total number of ϕ mesons ($N_{\phi(DATA_{RECO})}$) reconstructed, the number of ϕ background events ($N_{\phi(BG)}$), and the integrated luminosity $\mathcal{L}$ for each of the three targets.

4.2.4 ϕ Cross-Section

The formula for the experimental determination of the ϕ cross-section is given by

$$\sigma(\phi \to K^+K^-) = \frac{N_{\phi(\mathrm{DATA_{RECO}})}}{\mathcal{L}\ \mathcal{BR}(\phi \to K^+K^-)\epsilon_{\mathrm{TRIGGER}}\epsilon_{\phi(\mathrm{RECO})}} \tag{4.15}$$

where $\epsilon_{TRIGGER}$ is the trigger efficiency and is ≈ 1. The reconstruction efficiency for $\phi \to K^+K^-$, $\epsilon_{\phi(RECO)}$, is determined using Monte Carlo. The reconstruction efficiency is given by,

$$\epsilon_{\phi(RECO)} = \frac{N_{\phi(\mathrm{MC_{RECO}})}}{N_{\phi(\mathrm{MC_{GEN}})}} \tag{4.16}$$

The number of Monte Carlo generated ϕ's are counted conditionally by requiring the Lund particle code of 333 be present in an event. The Monte Carlo data file used for analysis was created in such a way that every event stored contains at least one ϕ decaying into K^+K^-. Events without a ϕ decaying into K^+K^- are not stored in this file. Hence the reconstruction efficiency need not be corrected for the branching

ratio of $\phi \rightarrow K^+K^-$. The Monte Carlo reconstruction is done in the same way as data.

The efficiency has to be calculated using the Monte Carlo, but the value of the efficiency can be related to the experiment when there is good agreement between data and Monte Carlo simulations. This can be verified by looking for differences between normalized distributions of data and Monte Carlo simulated events as a function of either the transverse momentum or the longitudinal momentum. The comparison of the p_T^2 distribution between data and Monte Carlo in Figure 4.10 shows a clear difference. The data show less production of ϕ mesons in comparison to Monte Carlo for $p_T < 1.0$ GeV/c, while for higher p_T region the situation is opposite. To account for this discrepancy, a reweighting of the Monte Carlo events is performed.

The reweighting procedure [43] applies a weighting factor to each p_T^2 bin where the weighting factors are determined by the ratio of number of events for data to Monte Carlo. The corrected x_F distribution and y $(= \frac{1}{2}\ln\left(\frac{E+p_z}{E-p_z}\right))$ distributions are shown in Figures 4.12 and 4.13 respectively. The agreement in the x_F and the y distributions become much closer after applying the correction procedure. The relation between the correction factors versus p_T^2 shown in Figure 4.11 suggests that the number of particles generated in the first p_T bin between 0 - 0.25 GeV/c should go down by a factor of two. A simple extrapolation procedure gives the corrected number of Monte Carlo events generated. The corrected efficiency is used to calculate the cross-section. The values of the corrected efficiency determined from Monte Carlo are shown in column 4 of Table 4.4 which is determined by dividing column 3 from column 2. The total cross-sections are listed in column 5 of Table 4.4.

Table 4.4 *Table for ϕ production cross-sections.*

Target material	$N_{\phi(MC_{GEN})}$	$N_{\phi(MC_{RECO})}$	ε_ϕ, **%**	σ_ϕ, **mb**
Carbon	611740 ± 1074	7625 ± 221	1.25 ± 0.02	10.62 ± 0.11 ± 0.75
Titanium	613123 ± 1030	7270 ± 220	1.19 ± 0.02	40.13 ± 0.39 ± 2.58
Tungsten	1427598 ± 1696	17205 ± 332	1.20 ± 0.01	132.97 ± 1.26 ± 7.67

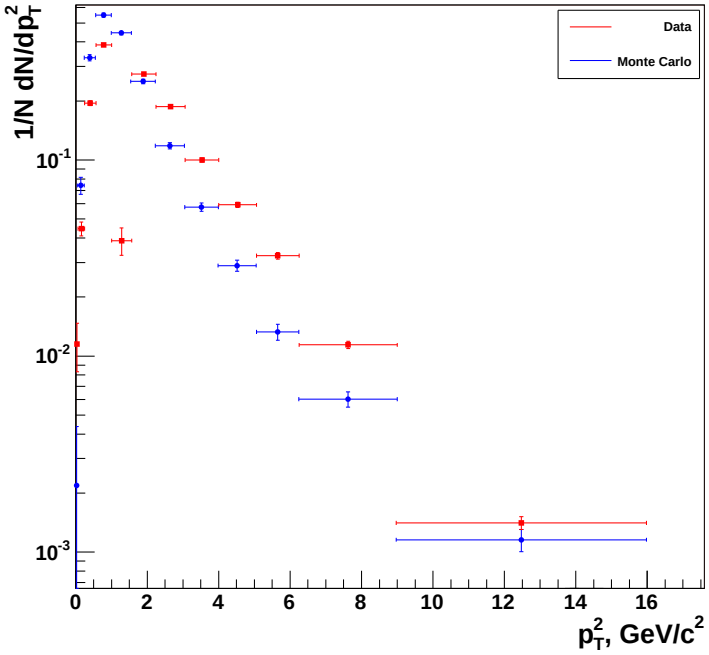

Figure 4.10 *A plot showing disagreement between data and Monte Carlo.*

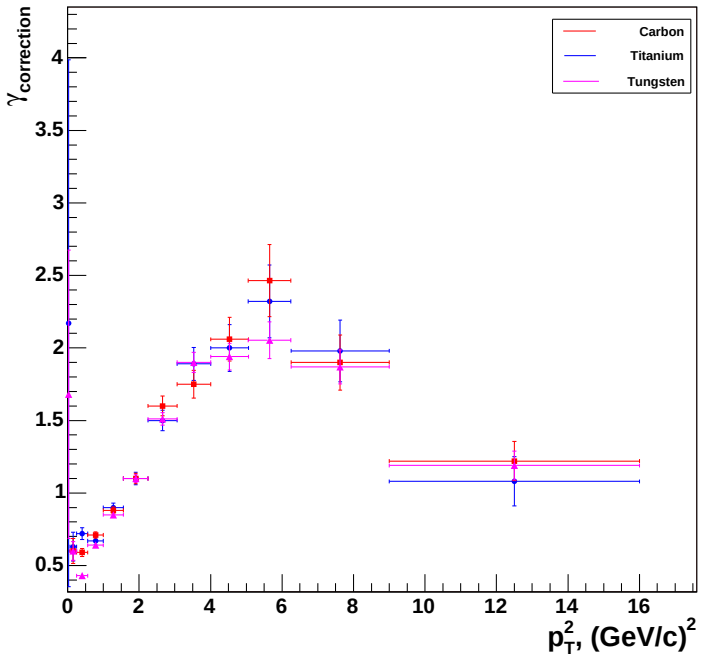

Figure 4.11 *The γ correction factor as a function of p_T^2.*

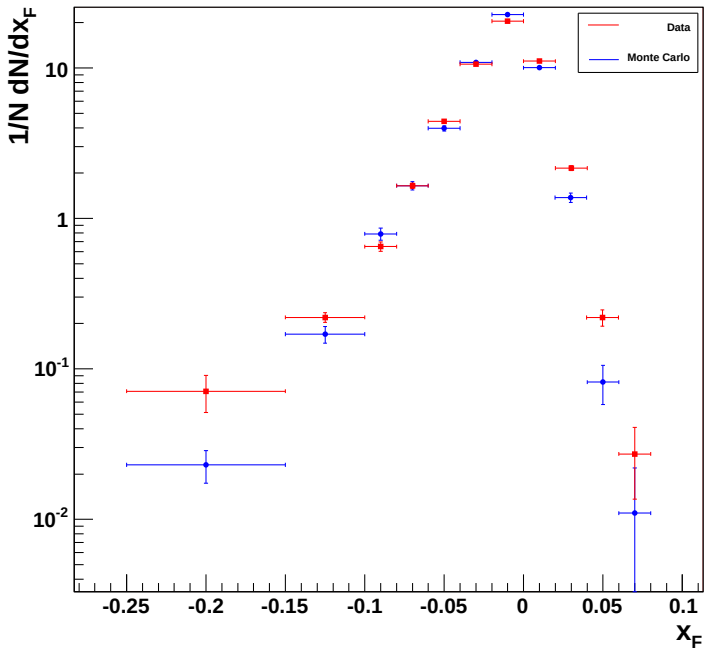

Figure 4.12 *The x_F distribution after the p_T^2 correction .*

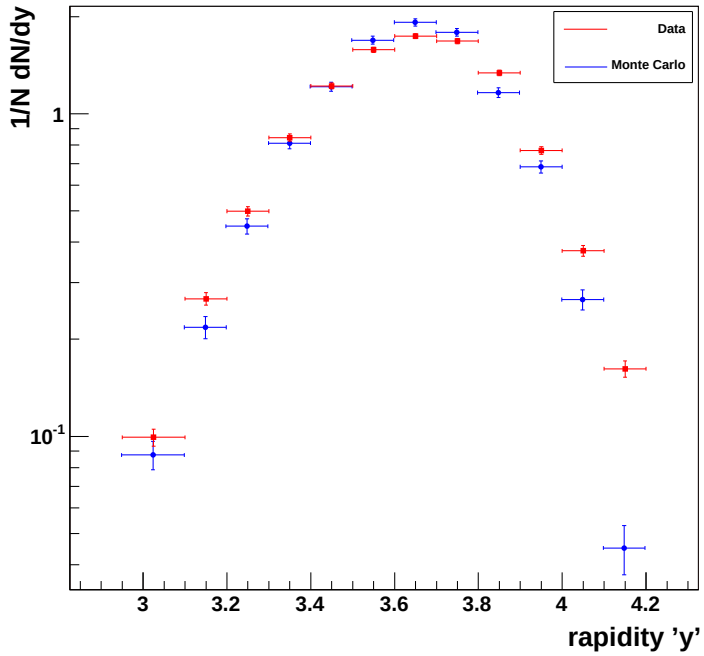

Figure 4.13 *The rapidity "y" distribution after the p_T^2 correction.*

4.2.5 $A-$dependence of ϕ production

Starting from equation 4.8, we can write:

$$\ln(\sigma) = \alpha \ln(A) + \ln(\sigma_0) \tag{4.17}$$

where σ_0 is the cross-section coefficient and α gives the $A-$dependence. Using the total cross-sections for the three different target materials as listed in column 5 of Table 4.4, we can determine σ_0 and α by using a linear fit to equation 4.17. The three data points with errors are shown in Figure 4.14, where $\ln(\sigma)$ is plotted against $\ln(A)$. The statistical and the systematic errors are added in quadrature. The straight line in Figure 4.14 is the least-square fit to the data. From the fit, the value of α was determined from the slope to be $\alpha = 0.92 \pm 0.03$, and the value of σ_0 was determined from the $y-$intercept to be $\sigma_0 = 1.08^{+0.14}_{-0.12}$ mb/N.

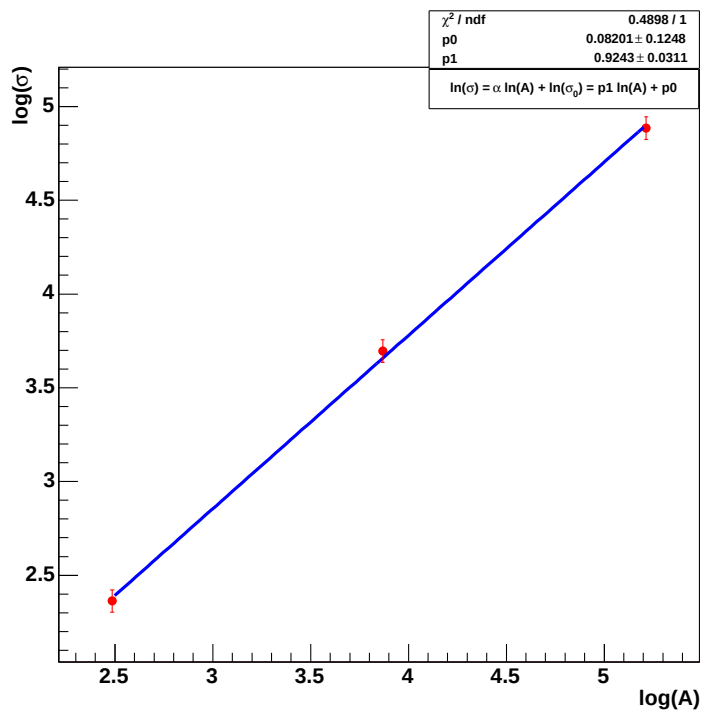

Figure 4.14 *Plot to measure α and σ_0.*

4.3 Open Charm Analysis

The ϕ cross-section has been measured. The next step is to determine the charm fraction in the ϕ sample and then calculate the inclusive open charm production cross-section.

4.3.1 Selection Criteria

Open charm analysis involves a separate selection criteria. The data sample is the same as the one used for the ϕ analysis. Loose cuts were applied for the ϕ analysis because the requirement was to have the maximum number of ϕ mesons reconstructed to measure ϕ production. For the open charm analysis, we need a purer sample of ϕ's with reduced background. The event quality cuts remain the same. Tighter cuts are applied to ensure track quality.

- Likelihood cuts are tightened to reduce misidentification of pions and protons as kaons. This gives a purer sample of ϕ's with an improved signal to background ratio.
- Decay products from heavier quarks have higher p_T. The accessible region begins at $p_T \approx 0.5$ GeV/c in HERA-B (The lower p_T region is not accessible because of the geometry of the HERA-B detector). A $p_T > 1$ GeV/c was applied. This cut is expected to improve detection efficiency of ϕ's from charm.
- Distance of closest approach (DCA) is the shortest distance between two tracks. The midpoint of this shortest distance line is defined as the reconstructed secondary vertex. The method used for the reconstruction of the secondary vertex from the two kaon tracks is described in Appendix A. Previously for ϕ selection, the DCA cut was not applied, but it is expected to help select purer ϕ's for charm analysis. It was noted in Figure 4.8 that the opening angle spread for the KK pairs that make up the ϕ's range between 1 and 30 mrad. The small opening angle leads to poor resolution along the z direction. In order to minimize background, a DCA cut of < 500 μm was applied.

- Mass window is maintained to be $\approx 3\Gamma \approx \pm 12$ MeV/c^2.

Method to determine a value for Δz from the distribution

The next important criterion concerns the method to determine Δz. First of all, a range must be fixed to measure Δz so that the long uneven tail of the distribution does not mislead us towards an incorrect value for Δz. The various methods that were considered for this analysis include: determining the mean by averaging all data for Δz, the median of the Δz distribution, and the value of the mean from fitting the Δz distribution. The median has a 25% greater error compared to the mean.

Figure 4.15 shows that the Δz distributions are symmetric about the peak. Note that the peak is slightly shifted from zero towards the downstream direction for the data sample. This shift is the motivation to pursue this analysis. The central value from fitting the Δz distribution to a gaussian is very close to the mean obtained by averaging the data. Hence, the mean obtained by averaging is used for the present analysis.

All the results for this analysis are measured using the mean of Δz calculated using the simple averaging technique. The range within which these values are evaluated is chosen by using the standard deviation of the distribution. The wider the range of Δz, the higher the standard deviation. An optimum choice for the Δz range ± 3 cm has been made, which is about $\pm 3\sigma$. The value of Δz averaged within this range will be used for the charm fraction calculation.

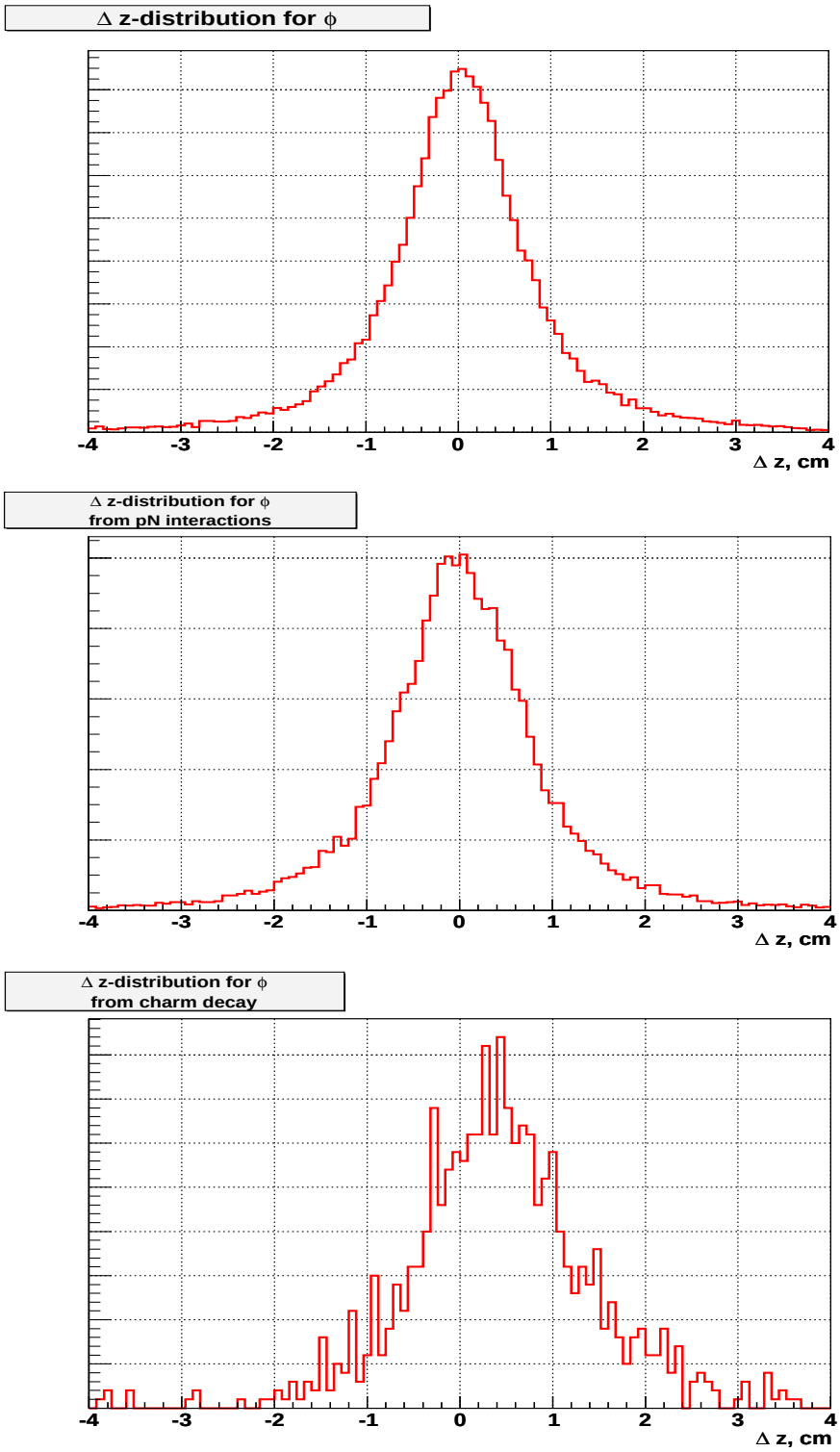

Figure 4.15 Δz *resolution plot for* ϕ*'s from data (top), primary interactions (middle), and charm decays (bottom).*

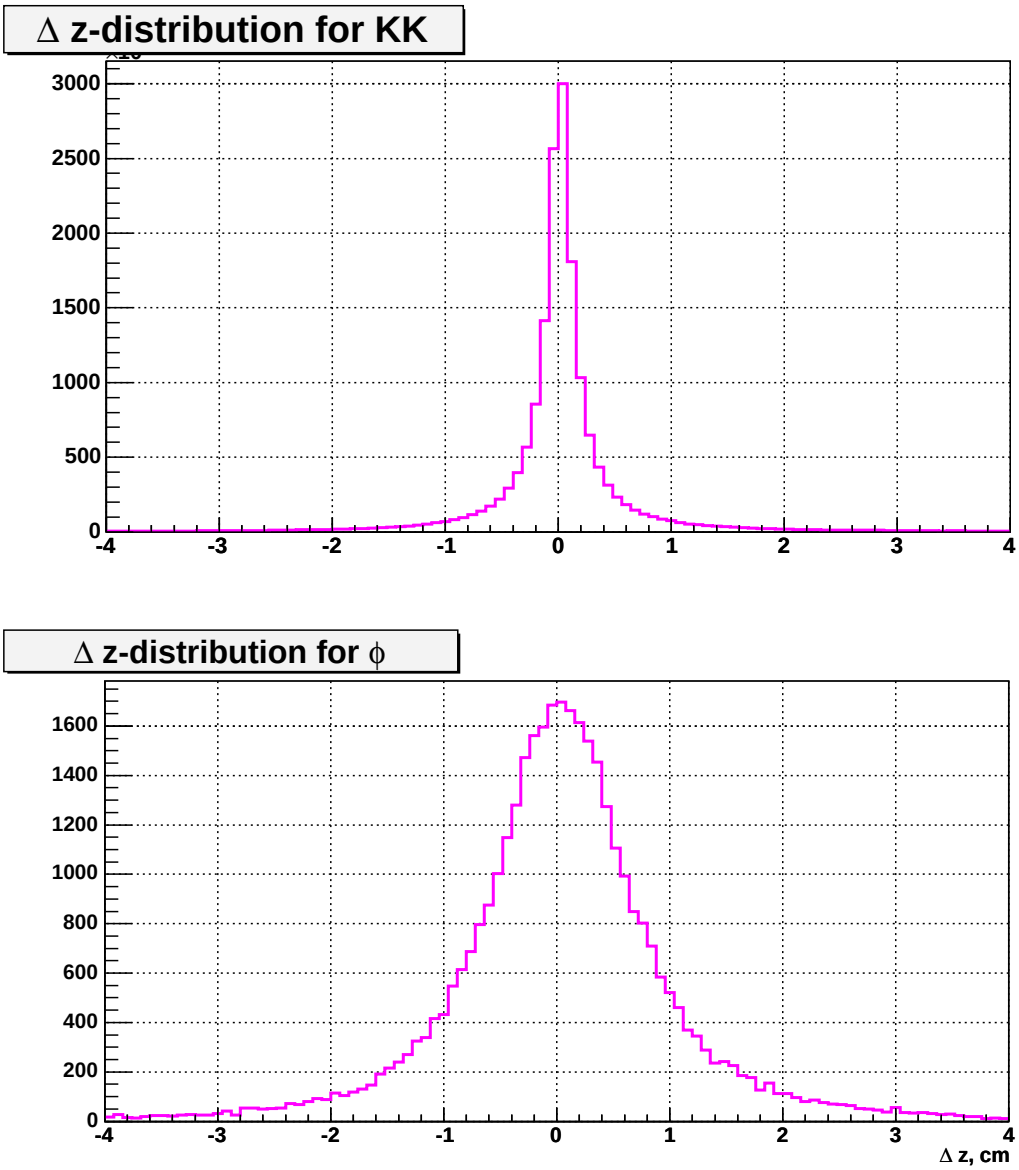

Figure 4.16 Δz *resolution plot for* K^+K^- *(top) and* ϕ *(bottom).*

4.3.2 Determination of the fraction of ϕ mesons from charm decay by the Δz method

The Δz method described above in section 4.1 allows extraction of the fraction of ϕ's coming from charm by using

$$f_{D\phi} = \frac{\Delta \mathrm{z}_{T\phi} - f_{P\phi}\Delta \mathrm{z}_{P\phi} - f_{BG\phi}\Delta \mathrm{z}_{BG\phi}}{\Delta \mathrm{z}_{D\phi}} \tag{4.18}$$

$\Delta z_{D\phi}$ is determined using the charm Monte Carlo. After the HERA-B event simulation, a file was created with the requirement that there be at least one charm particle per event stored in the file as was done in creating the ϕ file. The ϕ's from charm were chosen by requiring that a track with particle ID from the Lund code be 333 (ϕ) and its mother track be either 411 (D^0), 421 (D^+), 431 (D_s^+) or its negative counterparts to account for the anti-particles of the three charmed mesons. Similarly, $\Delta z_{P\phi}$ is determined from the ϕ Monte Carlo. The choice here was to have a track with particle ID 333 and its mother track must be either 92 or 91, which stands for internal sub-processes and represents primary interactions. The Δz distributions from the three samples (total sample, primary interaction sample and open-charm sample) are shown in Figure 4.15. From the distribution, it is clear that the Δz of the ϕ's from charm decay are displaced from the primary vertex, seen by the shift in the peak of the distribution. The value for Δz is the average of all the Δz entries in the distribution.

The Δz values for the direct ϕ Monte Carlo are determined by combining all the target materials. This is done in order to reduce the Monte Carlo statistical error on these Δz values, which in turn helps in reducing the systematic error of the fraction and hence the cross-section. The Δz values for the charm Monte Carlo are also added together.

It is important here to remark about an interesting observation on the primary vertex reconstruction. It is regarding the Δz values as a function of the K^+K^- invariant mass scale, as shown in Figure 4.17.

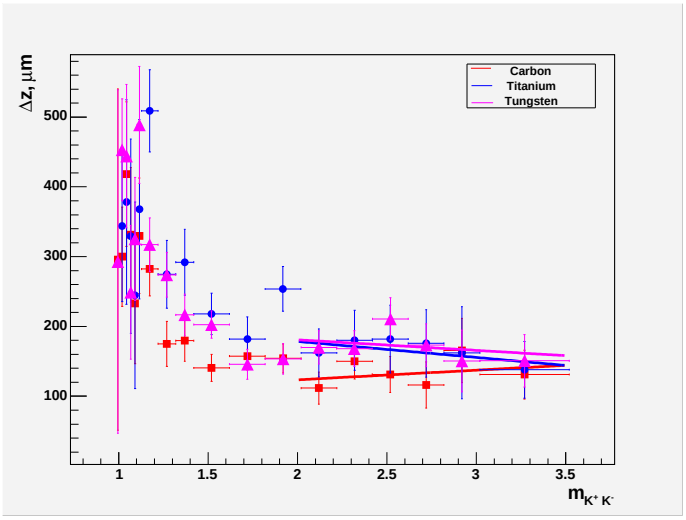

Figure 4.17 *The* Δz *as a function of* $m_{K^+K^-}$ *with primary vertices from ARTE tables.*

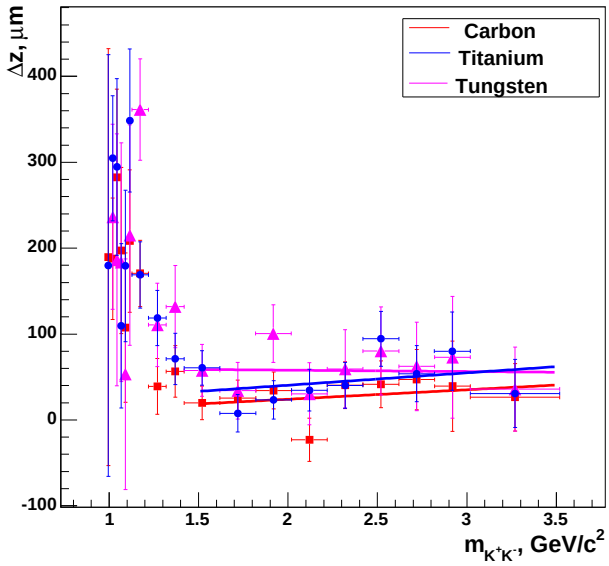

Figure 4.18 *The* Δz *as a function of* $m_{K^+K^-}$ *with primary vertices reconstructed by the averaging method.*

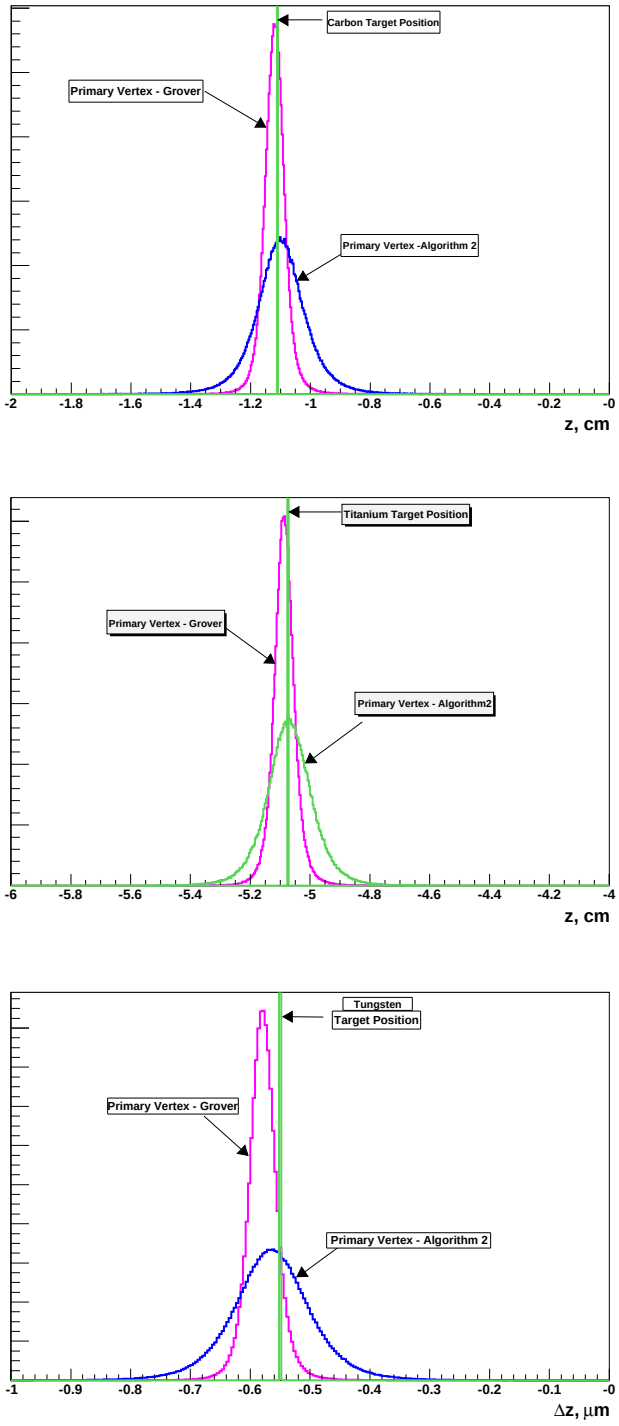

Figure 4.19 *The z−coordinate distribution of the primary vertices obtained from ARTE table, those obtained by "the averaging of all vertices of track pairs in an event" method and the target position.*

For $m_{KK} > 2$ GeV/c^2, the Δz values are expected to be zero. The reason is that the kaons that pair up to give high invariant mass values cannot be produced from multiple decays. This suggests that these kaon pairs are produced from primary interactions and hence their Δz must be zero. The plot in Figure 4.17 shows the Δz values, reconstructed using primary vertex positions from the ARTE table, in the high mass region is nonzero and constant. This leads to a speculation that there might be a systematic shift in the reconstructed primary vertices in the ARTE tables. In Figure 4.17 shows the Δz values for the ϕ is the second bin point from the left.

The primary vertex reconstruction was done by the standard software with many alignment inputs. Considering the observation above, a simple algorithm was used to reconstruct the primary vertices. The algorithm takes all the tracks in an event and makes pairwise reconstruction of vertices and finally fixes the average of these vertices to be the primary vertex of that event. There is a selection criterion applied for this reconstruction which requires that there be at least 4 tracks in the event and the z coordinate of a pair-vertex must not be too far away from the target z coordinate. The difference between z coordinates of the new primary vertices and the old ones are shown in Figure 4.19. The Δz values measured using the new primary vertices are closer to zero even though there is still an offset. But the offset is approximately the statistical error.

Table 4.5 *Table for Δz displacement of ϕ's.*

Tg	$\Delta z_{T\phi}$, μ**m**	$\Delta z_{BG\phi}$, μ**m**	$\Delta z_{P\phi}$, μ**m**	$\Delta z_{D\phi}$, μ**m**
C	$187.68 \pm 70.70 \pm 15$	$257.34 \pm 132.24 \pm 30$	$12.66 \pm 66.82 \pm 8$	$4210.67 \pm 290.47 \pm 110$
Ti	$236.46 \pm 107.80 \pm 20$	$393.91 \pm 192.12 \pm 30$	$12.66 \pm 66.82 \pm 8$	$4210.67 \pm 290.47 \pm 110$
W	$304.67 \pm 72.73 \pm 40$	$413.15 \pm 132.6 \pm 50$	$12.66 \pm 66.82 \pm 8$	$4210.67 \pm 290.47 \pm 110$

The Δz values are given in Table 4.5. From this the fraction of ϕ's from charm is determined. The measured values of the fractions are given in Table 4.6. The fraction $f_{D\phi}$ given in Table 4.6 is the fraction of charm ϕ's with respect to the total ϕ sample.

Table 4.6 *Table of fraction of ϕ's.*

Target	f_ϕ, %	$f_{BG\phi}$, %	$f_{D\phi}$, %
C	$66.69 \pm 0.54 \pm 0.25$	$33.31 \pm 0.47 \pm 0.15$	$2.23 \pm 1.98 \pm 1.16$
Ti	$66.96 \pm 0.82 \pm 0.25$	$33.04 \pm 0.69 \pm 0.15$	$2.33 \pm 2.98 \pm 1.20$
W	$66.66 \pm 0.46 \pm 0.25$	$33.34 \pm 0.40 \pm 0.15$	$3.77 \pm 2.02 \pm 1.09$

The fraction that we have obtained is the fraction of ϕ's coming from charm decay with respect to the total number of ϕ's under the signal without background subtraction. Hence, $N_{D\phi}/N_\phi$ is given by

$$\frac{N_{D\phi}}{N_\phi} = \frac{f_{D\phi}}{f_{D\phi} + f_{P\phi}} = \frac{f_{D\phi}}{f_\phi} \tag{4.19}$$

The main source of error in the fraction is the statistical error of the sample. The estimated Δz shift of a charm signal with respect to the amount of ϕ's reconstructed is about 100 μm. From Table 4.5, the statistical error on the Δz of the total sample is close to 75 μm giving a 75% fractional error. The error of the background is reduced by the background fraction and the error of the Monte Carlo events is also reduced by its respective fraction. The error in the fraction measurement directly affects the cross-section measurement.

4.3.3 Charm Cross-section

Table 4.4 gives the values for ϕ production cross-sections, and the fractions are listed in Table 4.6. The values of the efficiencies of ϕ reconstruction from charm decay

Table 4.7 *Table of efficiencies for ϕ and charm detection.*

Target	ϵ_ϕ **in %**	$\epsilon_{D\phi}$ **in %**	$\eta = \frac{\epsilon_{D\phi}}{\epsilon_\phi}$
C	0.512 ± 0.008	1.47 ± 0.08	2.85 ± 0.16
Ti	0.53 ± 0.008	1.36 ± 0.11	2.59 ± 0.15
W	0.51 ± 0.005	1.34 ± 0.07	2.66 ± 0.11

compared to ϕ's from primary interactions are listed in columns 1 and 2 of Table 4.7.

The ratio of these efficiencies are listed in column 3. The ratio of efficiencies increases with p_T. This confirms the fact that the ϕ's from charm have higher p_T. With the efficiency ratio, the fraction of ϕ's from charm, and the ϕ cross-section measured, the inclusive charm production cross-section is calculated using the following equation,

$$\sum_i \mathcal{B}R(D_i \to \phi) \cdot \sigma_{0D_i} = \frac{\mathrm{f} \cdot \sigma_{0\phi}}{\eta \cdot \mathrm{A}^{1.02-0.92}} \tag{4.20}$$

where the $A-$dependence of charm and ϕ production is taken into account. The errors on the cross-section values are separated into statistical and systematic. All the Monte Carlo errors and the systematic errors on the data sample are combined to give the systematic error. The statistical error is from the size of the data sample.

Table 4.8 *Table for charm cross-section.*

Target	$f = \frac{f_{D\phi}}{f_\phi}$, **%**	$\eta = \frac{\epsilon_{D\phi}}{\epsilon_\phi}$	$\sum_i \mathcal{B}R(D_i \to \phi) \cdot \sigma_{0D_i}$, μ**b/N**
Carbon	$3.34 \pm 2.97 \pm 1.74$	2.85 ± 0.16	$9.87 \pm 8.78 \pm 5.18$
Titanium	$3.48 \pm 4.41 \pm 1.79$	2.59 ± 0.15	$9.86 \pm 13.53 \pm 5.13$
Tungsten	$5.66 \pm 3.03 \pm 1.64$	2.66 ± 0.11	$13.64 \pm 7.31 \pm 4.02$

Table 4.8 lists the values of the inclusive charm cross-section coefficient weighted by the branching ratio for three different target materials and the average value is $11.12 \pm 5.90 \pm 4.80$ μb$/N$. The results can be interpreted as an upper limit. The statistical errors are larger than the systematic errors. When we make an estimate of $\sum_i \mathcal{BR}(D_i \to \phi \to K^+K^-)\sigma_{0D_i}$ with the known values of production cross-sections for the various D's and their branching ratios taken from the PDB, we obtain the estimate as 4.28 ± 3.28 μb$/N$. The dominant error of the estimate is the branching ratio of $D_s \to \phi$ which is $\approx 18^{+15}_{-10}\%$. Thus the measured result and the theoretical result agree within quoted errors.

CHAPTER 5

SUMMARY

In this dissertation, the charm and ϕ analyses were performed with data from the HERA-B experiment. In particular,

- The ϕ cross-section has been measured.
- The fraction of ϕ mesons from charm decay has been measured.
- The inclusive charm branching ratio times the cross-section has been determined using $D_i \rightarrow \phi \rightarrow K^+K^-$ channel.

The data used for this analysis were collected using the interaction trigger during the December 2002 run-period of HERA-B. The experiment involved interactions of 920 GeV/c protons on Carbon, Titanium and Tungsten targets. The ratio of data from each target is about 68:21:60 million events. The ϕ's were reconstructed using oppositely charged kaon pairs. The invariant mass distribution of the kaon pairs was fitted using a Gaussian mass resolution function convoluted with a relativistic Breit-Wigner function plus a background function. The intrinsic width of the ϕ signal was fixed to match the value from the PDB in the fit. The mass of the ϕ was determined as $1019.41 \pm 0.03 \pm 0.05$ MeV/c^2. The mass resolution obtained from the ϕ signal was 1.7 ± 0.3 MeV/c^2 which is less than the intrinsic width of the ϕ signal. The number of ϕ's is equal to the area under the ϕ signal with background subtracted, which is "the integral of the fit function minus the background function" within a mass range of 26 MeV/c^2 divided by the bin size of the mass distribution. The efficiency of ϕ reconstruction was determined using Monte Carlo event simulation. The efficiencies were obtained from Monte Carlo event simulations

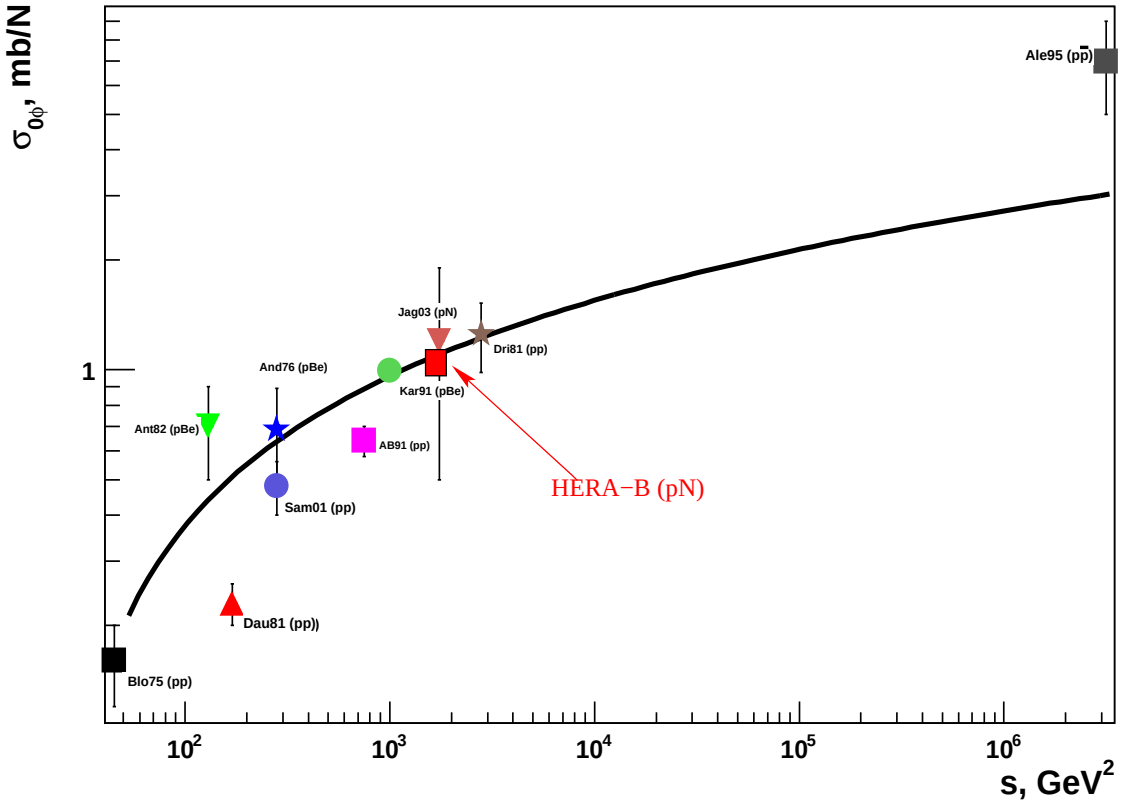

Figure 5.1 *The ϕ cross-section measured at HERA-B is compared to other experiments.*

which were run through the same geometry as the December 2002 period data used. The Monte Carlo model used for ϕ generation under-produced ϕ's in the high p_T region. A reweighting procedure was applied to determine the ratios of the number of events in data to the number of events generated in Monte Carlo for each p_T^2 bin. These ratios were multiplied to the number of Monte Carlo generated events of each p_T^2 bin to obtain the corrected total number of ϕ's generated. After applying the p_T^2 reweighting procedure, there was good agreement between data and Monte Carlo in the x_F and y distributions. With good agreement between data and Monte Carlo, the reconstruction efficiency was determined to be $\approx 1.25\%$. The cross-section of ϕ production was then measured to be $(1.08^{+0.14}_{-0.12}) \cdot A^{0.92}$ mb. The agreement with

theory and other experiments is good, as can be seen from Figure 5.1. The value $\alpha = 0.92 \pm 0.03$ which shows the atomic mass dependence was measured from the total cross-sections for ϕ production from three different target materials.

The fraction of ϕ mesons from charm decays was measured using the Δz method. The fraction was obtained by applying a $p_T > 1$ GeV/c cut, because it gives a higher efficiency of detecting ϕ mesons from charm decays to those produced in primary interactions. Also, a higher likelihood cut for both of the kaons was applied to reduce background. ϕ mesons within $M_\phi \pm 12$ MeV/c^2 were chosen in order to not include too much of the tail and hence reduce background effects. The background Δz was measured using Δz values from the immediate sidebands of the ϕ mass peak. It was observed that the Δz of the background is significantly higher than the Δz of the ϕ signal. The Δz value for the ϕ's produced from primary interactions and the Δz value for those produced from charm decay were obtained from Monte Carlo simulations. The p_T^2 correction that was applied to ϕ production was not applied to the Δz measurements but was applied on the efficiency measurements in the charm analysis. The fraction of ϕ mesons from charm decays was measured to be $\approx 3.5 \pm 2.7 \pm 1.7\%$.

Table 5.1 *Properties of* D *mesons.*

Particle	D_i **cross-section,** μ**b**/N	$\mathcal{BR}(D_i \to \phi)$**, %**
$D^0(D^0)$	$38 \pm 3 \pm 13$ @ 800 GeV/c (Kodama91)	1.7 ± 0.8
$D^+(D^-)$	$38 \pm 9 \pm 14$ @ 800 GeV/c (Kodama91)	< 1.8
$D_s^+(D_s^-)$	$\frac{\sigma(\mathrm{D_s})}{\sigma(\mathrm{D^0+D^+})} \approx 0.2$ (Adamovich96)	18^{+15}_{-10}

Finally, the inclusive charm production was measured in terms of branching ratio times cross-section. The average value of this measurement was $(11.12 \pm 5.90 \pm 4.81) \cdot A^{1.02}$ μb, where the A^α dependence of open-charm production cross-section was taken from another experiment [41]. Using the known values of cross-section and branching ratios from other experiments and theory as listed in Table 5.1, the inclusive production cross-section is calculated to be $\approx (4.28 \pm 3.28) \cdot A^{1.02}$ μb. Comparing the two results, we find that they agree within their quoted errors.

To summarize, the ϕ cross-section and its A^{α} dependence has been measured to be,

$$\sigma_{\phi} = (1.08^{+0.14}_{-0.12}) \cdot A^{0.92 \pm 0.03}\ mb \tag{5.1}$$

and the fraction of ϕ's from charm decay and hence the inclusive open charm production cross-section weighted by the branching ratio to decay into a ϕ has been measured to be,

$$\sum_i \mathcal{BR}(D_i \rightarrow \phi)\sigma_{D_i} = (11.12 \pm 5.90 \pm 4.81) \cdot A^{1.02}\ \mu b \tag{5.2}$$

APPENDIX A

Method to reconstruct a vertex from two given tracks

The reconstruction of a vertex from two given tracks is a simple geometrical problem. The method involves finding the shortest distance between two lines in 3D, in our case the lines are the tracks that has defined point on the line and a direction. So the tracks can be represented by two vectors such as:

$$\tilde{\mathrm{u}} = \tilde{\mathrm{r}_1} + \lambda \hat{\mathrm{e}_1} \tag{A.1}$$

$$\tilde{\mathrm{v}} = \tilde{\mathrm{r}_2} + \mu \hat{\mathrm{e}_2} \tag{A.2}$$

where $\tilde{\mathrm{r}_1}, \tilde{\mathrm{r}_2}$ are the position vectors of two points on the tracks and $\hat{\mathrm{e}_1}, \hat{\mathrm{e}_2}$ are the directional vectors. Now $\tilde{\mathrm{s}} = \tilde{\mathrm{v}} - \tilde{\mathrm{u}}$ is a vector between any two points on the two lines. Now if s should be the shortest distance, then the scalar quantity i.e the square of the distance 's' when differentiated with respect to the parameters λ and μ must be a minimum which also means $\tilde{\mathrm{s}}$ should be $\perp^r$ to both $\tilde{\mathrm{u}}$ and $\tilde{\mathrm{v}}$ as can be seen below.

From the definition of $\tilde{\mathrm{s}}$, we have

$$\tilde{\mathrm{s}} = \tilde{\mathrm{r}_2} - \tilde{\mathrm{r}_1} + \mu \hat{\mathrm{e}_2} - \lambda \hat{\mathrm{e}_1} = \tilde{\mathrm{r}_{12}} + \mu \hat{\mathrm{e}_2} - \lambda \hat{\mathrm{e}_1}, \tag{A.3}$$

and

$$\frac{\mathrm{ds}^2}{\mathrm{d}\mu} = 0 = 2(\tilde{\mathrm{r}_{12}} \cdot \hat{\mathrm{e}_2} + \mu \hat{\mathrm{e}_2} \cdot \hat{\mathrm{e}_2} - \lambda \hat{\mathrm{e}_1} \cdot \hat{\mathrm{e}_2}) \tag{A.4}$$

$$\frac{\mathrm{ds}^2}{\mathrm{d}\lambda} = 0 = 2(\tilde{\mathrm{r}_{12}} \cdot \hat{\mathrm{e}_1} + \mu \hat{\mathrm{e}_2} \cdot \hat{\mathrm{e}_1} - \lambda \hat{\mathrm{e}_1} \cdot \hat{\mathrm{e}_1}) \tag{A.5}$$

which is equivalent to,

$$\tilde{\mathrm{s}} \cdot \hat{\mathrm{e}_1} = \tilde{\mathrm{r}_{12}} \cdot \hat{\mathrm{e}_1} + \mu \hat{\mathrm{e}_2} \cdot \hat{\mathrm{e}_1} - \lambda \hat{\mathrm{e}_1} \cdot \hat{\mathrm{e}_1} = 0 \tag{A.6}$$

$$\tilde{\mathrm{s}} \cdot \hat{\mathrm{e}_2} = \tilde{\mathrm{r}_{12}} \cdot \hat{\mathrm{e}_2} + \mu \hat{\mathrm{e}_2} \cdot \hat{\mathrm{e}_2} - \lambda \hat{\mathrm{e}_1} \cdot \hat{\mathrm{e}_2} = 0 \tag{A.7}$$

Solving the two equations above, we obtain the value for λ and μ to be,

$$\lambda_0 = \frac{(\tilde{r_{12}} \cdot \hat{e_1}) - (\tilde{r_{12}} \cdot \hat{e_2})(\hat{e_1} \cdot \hat{e_2})}{1 - (\hat{e_1} \cdot \hat{e_2})^2} \tag{A.8}$$

$$\mu_0 = \frac{(\tilde{r_{12}} \cdot \hat{e_2}) - (\tilde{r_{12}} \cdot \hat{e_1})(\hat{e_1} \cdot \hat{e_2})}{1 - (\hat{e_1} \cdot \hat{e_2})^2} \tag{A.9}$$

Hence for values of λ_0 and μ_0, magnitude of $\tilde{s} = \tilde{r_{12}} + \mu_0 \hat{e_2} - \lambda_0 \hat{e_1}$ will be the shortest distance. Now the mid-point of this shortest distance line is considered to be the reconstructed vertex of the two tracks.

REFERENCES

[1] M Gell-Mann. "Quark Model". *Physics Letters*, **8**, 214, (1964).

[2] G. Zweig. *CERN Reports No*, CERN-TH **401**, 01, (1964).

[3] Donald H Perkins. *Introduction to High Energy Physics*, 4th *edition*, (2000).

[4] M K Gaillard, P D Grannis, F J Scuilli. "The Standard model of particle physics". *Review of Modern Physics*, **71, No. 2**, S96, (1999).

[5] David Griffiths. *Introduction to Elementary Particles*, (1987).

[6] R.P. Duperray, C.Y. Huang, K.V. Protasov, and M.Buenerd. "Parametrization of the antiproton inclusive production cross-section on nuclei". *Physical Review*, **D 68**, 094017, May (2003).

[7] Denis Dujimic. "Open Charm production at HERA-B". *http://www-hera-b.desy.de/general/thesis/diss/diss_denis_dujimic.pdf*, Doctoral dissertation, University of Texas at Austin, (2001).

[8] Kendall Reeves. "Charmonium production at HERA-B". *http://www-hera-b.desy.de/general/thesis/diss/diss_kendall_reeves.pdf*, Doctoral Dissertation, University of Texas at Austin, (2001).

[9] Patricia Conde. "Measurement of the ratio between the D+ and the D0 production cross section using an impact parameter method". *http://www-hera-b.desy.de/general/thesis/diss/diss_patricia_conde.ps.gz*, Doctoral dissertation, University of Santiago de Compostela, November (2002).

[10] M K Gaillard, P D Grannis, F J Scuilli. "Particle Data Book". *Physical Review D*, **66, No. 1**, 01, July (2002).

[11] R. Vogt. "Phenomenology of Charm and Bottom production". *Z. Physik*, **C 71**, 475, October (1996).

[12] Matteo Cacciari. "Heavy Quark Production: Theory vs Experiment". *http://www.arXiv.org/pdf/hep-ph/0312194*, December (2003).

[13] R. Ammar, *et al*. "D-Meson Production in 800-GeV/c pp Interactions". *Physical Review Letters*, **61, No. 19**, 2185, November (1988).

[14] Duncan A. Morris. "Heavy quark fragmentation functions in a simple string model". *Nuclear Physics*, **B 313**, 634, (1989).

[15] Marianne Bargiotti. "Studies on χ_c states at the HERA-B experiment". *http://www-hera-b.desy.de/general/thesis/diss/diss_marianne_bargiotti.pdf*, **DESY thesis**, May (2004).

[16] K H Lau, *et al*. "Fragmentation of Heavy Quarks Produced in e^+e^- Annihilation". *Physical Review Letters*, **50, No. 26**, 2054, June (1983).

[17] H. Dijkstra, *et al*. "Inclusive ϕ meson production, the parton fusion model and strange quark structure functions". *Z. Physik*, **C 31**, 391, (1986).

[18] S. Yazaki, M.Fukugita, T. Inami, N. Sakai. "Violation of the OZI rule in central production of the ϕ meson". *Physics Letters*, **B 68**, 251, (1977).

[19] J. Ivarsson. "Potential for B-Physics measurements with a fixed target proton collision experiment". *http://www-hera-b.desy.de/general/thesis/diss/diss_jenny_ivarsson.ps.gz*, Doctoral dissertation, Lund University, **ISBN 91-628-3661-7**, LUNFD6/(NFFL–7173), (1999).

[20] The HERA-B Collaboration. "HERA-B: An experiment to study CP violation in the B system using an internal target at the HERA-B proton ring − Proposal". *http://www-hera-b.desy.de/general/publications/proposal/proposal/prop.ps.gz*, **DESY-PRC 94/02**, (1994).

[21] The HERA-B Collaboration. "HERA-B: An experiment to study CP violation in the B system using an internal target at the HERA-B proton ring − Technical Design Report".
http://www-hera-b.desy.de/general/publications/proposal/tdr/tdr.ps.gz,
DESY-PRC 94/02, (1998).

[22] Brian Aagard Peterson. "Beauty production at HERA-B".
http://www-hera-b.desy.de/general/thesis/diss/diss_brian_aagard_petersen.ps.gz,
Doctoral dissertation, University of Copenhagen, (2002).

[23] P. Krizan and M. Staric. "An Iterative method for the analysis of Čerenkov rings". *http://www-hera-b.desy.de/subgroup/detector/rich/rich/id-algorithms/iterat.ps.gz*, **DESY-PRC**, (1999).

[24] I. Arinyo *et al*. "The HERA-B Ring Imaging Čerenkov Counter".
Nuclear Instruments and Methods, **A 516**, 445, (2004).

[25] E K Gerndt. "The HERA-B Trigger".
http://www-hera-b.desy.de/subgroup/trigger, (1999).

[26] The HERA-B Software group. "ARTE Manual and ARTE Tables".
http://www-hera-b.desy.de/subgroup/software/arte, (1996).

[27] R Mankel. "ARTE conventions".
http://www-hera-b.desy.de/subgroup/software/arte/arteconvent.html,
HERA-B Note, January (1998).

[28] A Gellrich. "Libraries in ARTE".
http://www-hera-b.desy.de/subgroup/software/arte/ARTE.html,
January (2001).

[29] A Gellrich. "Kumac Settings in ARTE".
http://www-hera-b.desy.de/subgroup/software/arte/KUMAC.html,
January (2001).

[30] A Gellrich. "Event Classification in ARTE". *http://www-hera-b.desy.de/subgroup/software/arte/ECLASS.html*, January (2001).

[31] T Lohse. "MCGEN: A general tool for MC production for physics at HERA-B". *http://www-hera-b.desy.de/subgroup/software/mc/welcome.html*, **HERA-B Note 99-098**, (1999).

[32] J Ivarrson, P Kreuzer, T Lohse. "PYTHIA and FRITIOF: Event generators for HERA-B". *http://www-hera-b.desy.de/subgroup/software/mc/welcome.html*, **HERA-B Note 99-067**, (1999).

[33] U Husemann. "The Monte Carlo simulation chain from a user's point of view". *http://www-hera-b.desy.de/subgroup/software/mc/welcome.html*, **HERA-B Note 03-020**, March (2003).

[34] Schuler *et al.* "The PYTHIA event generator manual". *http://www.thep.lu.se/ torbjorn/Pythia.html*, **PYTHIA 6.0**, (2003).

[35] H. Dijkstra *et al*, The ACCMOR Collaboration. "Hadronic ϕ production and the Lund model for low p_T interactions". *Z. Physik*, **C 32**, 349, (1986).

[36] P Aushev *et al*. "Luminosity determination". *http://www-hera-b.desy.de/subgroup/target*, (2003).

[37] E Fernandez *et al*, The MAC Collaboration. "Lifetime of Particles Containing b Quarks". *Physical Review Letters*, **51, No. 12**, 1022, September (1983).

[38] Lockyer *et al*, The MARK II Collaboration. "Measurement of the Lifetime of $B-$hadrons". *Physical Review Letters*, **51, No. 12**, 1316, September (1983).

[39] Mikayel Ispiryan. "A-dependence of ϕ production". *http://www-hera-b.desy.de/general/thesis/diss/diss_michael_ispiryan.pdf*, Doctoral dissertation, University of Houston, May (2004).

[40] R. Bailey *et al*. "A-Dependence study of inclusive ϕ production". Z. *Physik*, **C 22**, 125, (1984).

[41] M. J. Leitch. "Nuclear Dependence of Neutral-D-Meson Production by 800 GeV/c Protons". *Physical Review Letters*, **72, No. 16**, 2542, April (1994).

[42] Mikayel Ispiryan. "Private Communication". (2003).

[43] Mikayel Symalla. "Produktion von ϕ mesonen in inelastischen proton-kern-wechselwirkungen". *http://www-hera-b.desy.de/general/thesis/diss/diss_michael_symalla.pdf*, Doctoral dissertation, Universität Dortmund, May (2004).